DEVELOPMENT OF A NEW TECHNIQUE TO IDENTIFY AND QUANTIFY COMPLEX AUSTENITE DECOMPOSITION PRODUCTS

by

Jinghui Wu

B.S. in Metal Processing, Northeastern University, China, 1996

M.S. in Materials Science and Metallurgy, Northeastern University, China, 1999

Submitted to the Graduate Faculty of

School of Engineering in partial fulfillment

of the requirements for the degree of

Doctor of Philosophy

University of Pittsburgh

2005

UNIVERSITY OF PITTSBURGH

SCHOOL OF ENGINEERING

This dissertation was presented

by

Jinghui Wu

It was defended on

November 17th, 2004

and approved by

Joseph D. Defilippi, US Steel Corporation

Claxito Issac Gracia, Research Professor, Materials Science and Engineering

Ian Nettleship, Associate Professor, Materials Science and Engineering

Qing-Ming Wang, Assistant Professor, Mechanical Engineering

Jörg M. K. Wiezorek, Associate Professor, Materials Science and Engineering

Dissertation Director: Anthony J. DeArdo, Professor, Materials Science and Engineering

ABSTRACT

DEVELOPMENT OF A NEW TECHNIQUE TO IDENTIFY AND QUANTIFY COMPLEX AUSTENITE DECOMPOSITION PRODUCTS

Jinghui Wu, PhD

University of Pittsburgh, 2005

Polycrystalline aggregates are comprised of three microstructural features: grain centers, grain boundaries, and regions affected by grain boundaries. It is these features that determine the mechanical properties, and any advanced understanding of microstructure-property relations requires their quantitative description. Traditionally, descriptions of microstructures have been based on visualization, i.e., how grains appear in the optical or scanning electron microscope (SEM). While this may lead to classification systems that permit differentiation, it does not allow for quantification, especially in complex microstructures, and does not lend itself to either developing or applying structure-property relationships. The goal of this study is to present a new approach to the characterization of complex microstructures, especially those found in advanced modern high strength steels. For such steels, the new approach employs the fact that different austenite decomposition products formed at different transformation temperatures have different dislocation or sub-grain boundary densities. Hence, measuring the degree of lattice imperfection of the grain centers of the ferrite is one way of first identifying, then grouping, and finally quantifying, the different types or forms of ferrite. The index chosen in this study to distinguish the degree of lattice imperfection is the image quality (IQ). As part of the new approach a procedure has been developed to improve the accuracy of applying IQ measurements. This procedure includes three major features: IQ normalization, Grain Boundary Region (GBR) identification and the Multi-Peak model. These three features make this new approach a unique technique, which quantitatively describes the complex microstructures with much more details. The potential application of this technique and further development has also been discussed at the end of this study.

TABLE OF CONTENTS

LIST OF TABLES

LIST OF FIGURES

ACKNOWLEDGEMENTS

The completion of this thesis would have never been possible without those helps, supports and assistances from so many kind persons. Here, I would like to give my most sincere thanks to them.

First and foremost, I would like to thank my advisors namely, Dr. A. J. DeArdo, Dr. C. I. Garcia and Dr. P. Wray for their unstinting support and guidance in this research. Their invaluable suggestions make the whole research so well organized and directed. I would also like to extend my gratitude to other members of my committee, Dr. Joseph D. Defilippi, Dr. Ian Nettleship, Dr. Qing-Ming Wang and Dr. Jörg M. K. Wiezorek. Their invaluable comments, corrections and criticism are gratefully acknowledged.

I would like to give my special thank to Dr. Ken Goldman. He is such a kind man, an excellent mentor and a great teacher. He is an advisor not only in your research, but also in your life. His generous help makes so many things possible.

I would like to thank all my BAMPRI colleagues for their encouragement throughout my stay at the University of Pittsburgh. Thanks are also due to the staff and faculty members of the Department of Materials Science and Engineering for their constant support.

The financial support provided by the AISI and the BAMPRI is gratefully acknowledged.

I would like to thank my parents and all my family members for believing in my capabilities and constantly supporting me in this challenging endeavor. Finally, I would like to thank my wife, Xuetian Han, for her love and patience and being with me through the most critical stages of this work.

Thank you all.

This thesis is especially dedicated to my parents, my wife and my son.

1.0 INTRODUCTION

1.1 SIGNIFICANCE OF THIS STUDY

The microstructure has a direct relationship to the final mechanical properties. Controlling the microstructure is believed to be the essential approach to the ideal mechanical properties and fully understanding the microstructures is the key to make the approach possible.

Considering the correlation of microstructure and mechanical properties, the Hall-Petch equation is a traditional and classical description, which has been widely used. Based on the Hall-Petch equation, the lower yield strength (σ_y) of the metal can be expressed as an expanded Hall-Petch equation assuming linear additivity [2, 3]:

$$\sigma_y = \sigma_{PN} + \sigma_s + \sigma_b + \sigma_{pp} + \sigma_d + \sigma_{texture} \qquad \textbf{1.1}$$

where σ_{PN} is the Peierls-Nabarro stress, which is the stress needed to move a dislocation into a perfect periodic lattice[4]; σ_s is the strengthening from solid solution [5]; σ_b is the strengthening from grain or phase boundaries [6]; σ_{pp} is the precipitation strengthening [7]; σ_d is the dislocation strengthening [2, 8] and $\sigma_{texture}$ is the texture strengthening [9].

The Hall-Petch equation could explain the yield strength form the view of the contribution from every strengthening mechanism. While most of these evaluations have been accomplished based on a large amount of experiments, the Hall-Petch theory is not convenient to be used in

modeling. Additionally, the interaction and trade off among those mechanisms are complicated, and all of them are very sensitive to the chemical composition and the processing conditions. These factors indicate that the Hall-Petch equation might not be the ideal theory for modeling.

Simplified approaches have been used in today's metallurgical models. One of the most typical simplifications is by using volume fraction of different decomposition products instead of those contributions from different mechanisms. From this point of view, the clear definition and accurate description of different decomposition products is very necessary for successful modeling. Although much research has been done on the classification, morphology and formation mechanism of all kinds austenite decomposition products, there are still many uncertainties and disagreements related to the description of austenite decomposition products, particularly when complex microstructures are formed.

The sensitivity of the microstructure evolution to the processing conditions leads to the complexity of the microstructures, which makes it so difficult for the quantitative description of microstructures to be accomplished. In these days, most commercial microstructure-mechanical property models are still based on the quantitative description of microstructures, which is accomplished mainly by expertise assumptions rather than measurement. Therefore, understanding the microstructure and providing accurate identification and quantification of microconstituents have become the key of correlating the microstructure and mechanical properties. It has been such a challenge that people have been struggling with for years.

1.2 CONTENT OF THE THESIS

The major goal of this thesis is to develop new techniques for better describing and quantifying the complex microstructures, such as HSLA hot band microstructures found in some preliminary research.

Several attempts to identify and quantify the austenite decomposition products will be discussed. The traditional methods, including optical microscopy, Scanning Electron Microscopy (SEM), for example, will certainly be used. Atomic Force Microscopy (AFM) will be discussed as a relatively new technique in the field of steel microstructure characterization. Fractal analysis will also be introduced to understand the grain boundary characteristics. For all of those techniques and ideas, their advantages and shortcomings will be summarized and compared.

Most of the efforts will be expended on the application of Electron Backscatter Diffraction (EBSD). Various types of information collected from EBSD will be evaluated, compared, and analyzed for a better understanding of the microstructure and grain boundary characteristics. As a newly proposed method, image quality (IQ) analysis will be studied in detail for its extended application in microstructure quantification. A series of materials and microstructures will be developed and studied. These microstructures vary from simple polygonal ferrite to complex HSLA hot band, indicating a wide range of application of this new methodology.

2.0 BACKGROUND

2.1 TRADITIONAL THEORIES OF AUSTENITE DECOMPOSITION

2.1.1 Austenite Decomposition Products

At different temperature ranges, pure iron has three (solid) allotropic forms: the δ-Fe, which is stable between 1538^{o}C and 1394^{o}C, the fcc phase, named austenite, which is stable between 1394^{o}C and 912 ^{o}C and the bcc phase, termed ferrite, which is stable below 912 ^{o}C. For Fe-C alloys, the metastable orthorhombic carbide with composition Fe_3C is called cementite. In order to facilitate the discussion of the austenite decomposition, the Fe-Fe_3C metastable equilibrium phase diagram is shown in Figure 2.1[10, 11] with the definitions of the A_1, A_3 and A_{cm} temperatures.

There are two typical methods used in studying the austenite decomposition behavior: isothermal transformation experiments and continuous cooling experiments. Time-temperature-transformation (TTT) diagrams can be constructed based on the results from isothermal transformation experiments, which show the extent of transformation with the passage of time at constant temperature. Continuous cooling transformation (CCT) diagrams illustrate the degree the transformation that has progressed with the passage of time and change in temperature for a given cooling rate. Both of these methods have been widely used in the research of austenite decomposition.

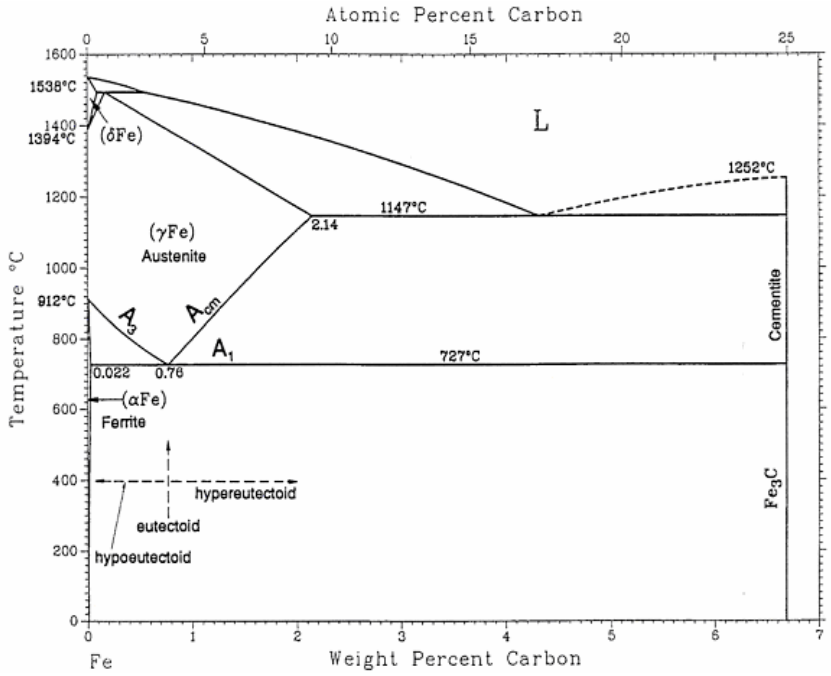

Figure 2.1 The Fe-Fe_3C metastable equilibrium phase diagram [11].

The products of the austenite decomposition vary with different time-temperature schedules, the final austenite microstructure and the base chemistry of the steel. Under equilibrium conditions, pro-eutectoid ferrite will form in iron-carbon alloys containing up to 0.8% carbon and the reaction occurs between 910°C and 723°C. With higher cooling rates, ferrite can be formed down to temperatures as low as 600°C. Dubé classified four well-defined morphologies of ferrite as grain boundary allotriomorphs, Widmanstätten side plates or laths, intragranular idiomorphs and intragranular plates [12]. Some additions were made later to this classification by Aaronson in his research on the ferrite reaction [13]. After decades of research, more than ten different kinds of microstructures have been identified from the decomposition products of austenite [14, 15]. It is of great importance to identify the morphologies of these microstructures, especially in complex mixtures, for further understanding the details of the transformation

kinetics and microstructures. A brief definition and description of each microstructure will be given in the following subsections. For all of those austenite decomposition products to be summarized, their identifications are only based on their appearance or morphology and, for most of them, accurate measurement of their volume fraction cannot be accomplished with any of the traditional techniques.

2.1.1.1 Grain Boundary Allotriomorphs Grain boundary allotriomorphs are crystals, which nucleate at grain boundaries in the parent phases and grow preferentially along these boundaries [16]. In hypoeutectoid steels, grain boundary ferrite is the first austenite decomposition product, which forms at the highest temperature and relatively low cooling rate. These ferrite grains are usually equi-axed or lenticular in form at the beginning. Facets will be developed on at least one side of these crystals if the transformation is performed at lower temperatures and the lenticular crystals will grow into equiaxed grains. Therefore, grain boundary ferrite is also called polygonal ferrite or equiaxed ferrite. This morphology has a very low dislocation density and very little substructure. Growth of grain boundary ferrite is controlled by rapid substitutional atom transfer across partially coherent boundaries and long-range diffusion of carbon atoms rejected from the growing ferrite grains.

Grain boundary ferrite exhibits a rational orientation relationship with respect to at least one austenite grain. The most accepted relationship is the Kurdjumov-Sachs (K-S), which allows low energy, immobile interfaces to develop between fcc and bcc phases [16]. The K-S relation is

$$\{111\}\gamma // \{110\}\alpha \text{ and } <1\bar{1}0>\gamma // <\bar{1}\bar{1}1>\alpha$$

2.1.1.2 Widmanstätten Side Plates Widmanstätten side plates are plate or needle shaped crystals that nucleate on the pre-existing ferrite allotriomorphs and grow into the interior of the matrix along well-defined planes as defined by the Kurdjumov-Sachs relationship [16, 17].

For hypoeutectoid steels, Widmanstätten ferrite is considered as a striking feature of those with lower carbon content. The morphology of Widmanstätten ferrite is very similar to that of bainitic ferrite and both structures have the surface relief effects typical of invariant plane strains, while Widmanstätten ferrite is formed at a higher temperature range and is preceded by the nucleation of grain boundary allotriomorphs [18]. Aaronson gave his explanation that the plate morphology of Widmanstätten ferrite is a result of the difference in the mobility of incoherent phase boundaries and coherent ones [19].

2.1.1.3 Acicular Ferrite Acicular ferrite is shaped and pointed like a needle. It nucleates heterogeneously on small non-metallic inclusions and radiates in many directions from these "point" nucleation sites; therefore, it has in three-dimensions the morphology of thin, lenticular plates [17]. Acicular ferrite cannot be formed at temperatures above the bainite start temperature.

2.1.1.4 Non-polygonal Ferrite Different from polygonal ferrite, non-polygonal ferrite has curved irregular boundaries and non equi-axed shape. Non-polygonal ferrite has various nucleation sites. When the cooling rate is satisfied, which is slow enough to avoid bainite and fast enough to avoid polygonal ferrite, it is formed at temperatures lower than polygonal ferrite and higher than acicular ferrite.

2.1.1.5 Massive Ferrite Massive ferrite is an austenite decomposition product usually found in very-low-carbon steels with rapid cooling where single-phase austenite is possibly transformed to single-phase ferrite without a composition change [20]. Massive ferrite usually has coarse ferrite grains and irregular boundaries. Since there is no composition difference, the transformation can be accomplished by short-range diffusion across interfaces [21]. Except for its irregular grain boundaries, massive ferrite differs from polygonal ferrite also in its high dislocation density, dislocation substructure and even containment of M/A constituents.

2.1.1.6 Pearlite Pearlite is a lamellar mixture of ferrite and cementite, which has been observed for over 100 years. The ideal morphology of pearlite is a hemispherical nodule nucleated on austenite grain boundaries and also on inclusions, and growing gradually into one austenite grain. The interface between pearlite and austenite is found to be incoherent. The spacing of the lamellae in pearlite is sensitive to the transformation temperature and decreases as the degree of undercooling below the eutectoid temperature increases. Well-defined crystallographic orientation relationships were found between cementite and ferrite lamellae within the pearlite nodule, but neither of them has an orientation relationship with the austenite grain in which they are growing [17].

2.1.1.7 Bainite Bainite is one of the most complex products of austenite decomposition, which was named after Bain, who with Davenport, first found these structures during their pioneering studies of the isothermal decomposition of austenite. After years of study, the definition of bainite still exists in three different forms [22, 23].

The general microstructural definition describes bainite as the product of the diffusional, noncooperative, competitive ledgewise growth of two precipitate phases formed during eutectoid decomposition, with the minority phases appearing in nonlamellar form. This alternative mode of eutectoid decomposition is thus fundamentally different from the diffusional, cooperative, shared growth ledges mechanism for the formation of pearlite.

On the surface relief definition, bainite is the plate-shaped product of a shear mode of phase transformation, usually taking place above the M_S temperature, as evidenced by an invariant plane strain (IPS) relief effect when the plate forms at a free surface.

In the view of the overall reaction kinetics definition, bainite has its own C-curve and time-temperature-transformation (TTT) diagram. There is an upper limiting temperature, termed the "kinetics B_S", which is well below the eutectoid temperature. When the kinetics B_S is approached, transformation of bainite starts and the amount of bainite increases as the transformation temperature is reduced until some critical condition is satisfied, which is called incomplete transformation and will be reviewed in following sections.

Based on the transformation temperature and the base chemistry of the concerned steel, the bainite microstructure has several classifications, Figure 2.2[23]. Different microstructures may have different contributions to the final mechanical properties.

2.1.1.7.1 Nodular Bainite

As shown in Figure 2.2 (a), nodular bainite is a kind of bainite structure whose external morphology is not predetermined by the morphology of either of the proeutectoid phases [23]. For nodular bainite to be formed, three conditions have to be met[22]:

Large contiguous volumes of untransformed matrix are available;

Eutectoid ferrite must have a higher growth rate than that of proeutectoid ferrite;

The nucleation rate of cementite on eutectoid α/γ boundaries must be higher than that on proeutectoid α/γ boundaries.

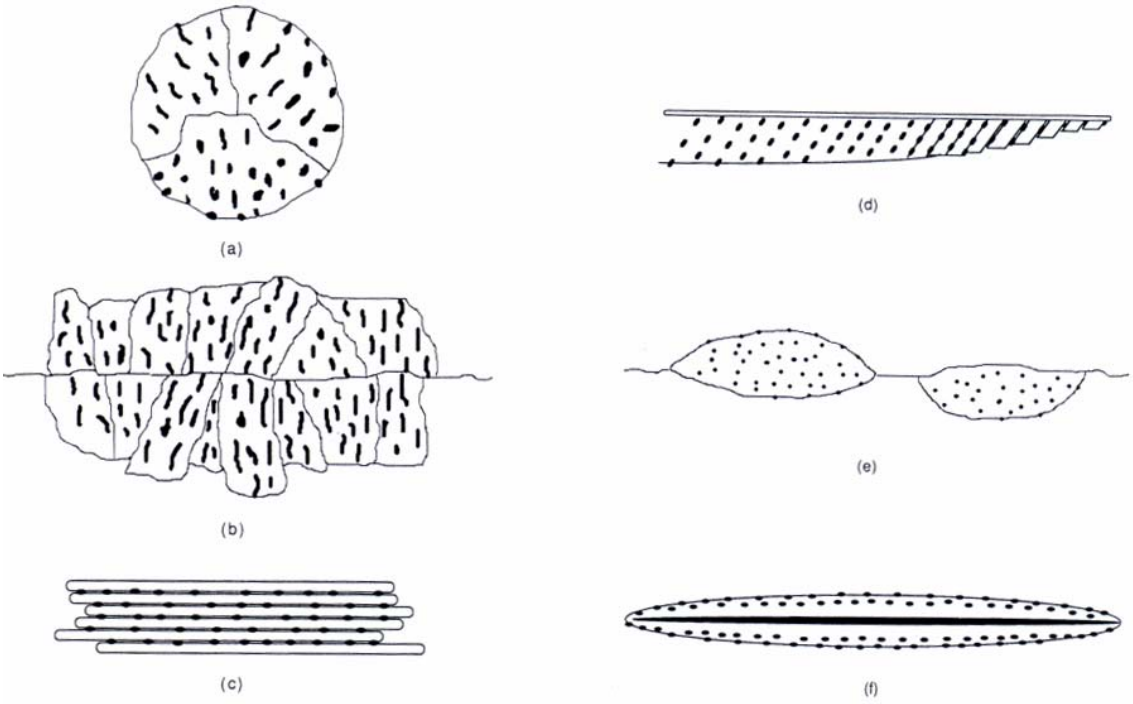

Figure 2.2 Schematic illustrations of the various bainite morphologies. (a) Nodular bainite; (b) Columnar bainite along a prior matrix grain boundary; (c) A sheaf of upper bainite laths; (d) Lower bainite; (e) Grain boundary allotriomorphic bainite, and (f) Inverse bainite. [23]

2.1.1.7.2 Columnar Bainite

Columnar bainite is a modification of nodular bainite with its external morphology affected by some microstructural features. The illustration of typical columnar bainite microstructure is shown in Figure 2.2 (b).

2.1.1.7.3 Upper Bainite

Upper bainite is usually formed in the temperature range of 550°C~400°C. The microstructure of upper bainite consists of fine plates of ferrite separated by low-misorientation boundaries or cementite particles. The plates of ferrite grow in clusters, which are called sheaves. In each sheaf, the plates have the same crystallographic orientation. The formation of upper bainite has two stages. The first stage is the formation of bainitic ferrite. Since ferrite has a very low solubility of carbon, the growth of bainitic ferrite will enrich the remaining austenite with carbon. In the second stage, cementite will precipitate from the residual austenite layers. The cementite particles have a Pitsch relationship with the austenite matrix:

$$[001]_{Fe3C} // [\bar{2}25]_{\gamma}, [100]_{Fe3C} // [5\bar{5}4]_{\gamma}, [010]_{Fe3C} // [\bar{1}\bar{1}0]_{\gamma}$$

2.1.1.7.4 Lower Bainite

Compared to upper bainite, lower bainite has a lower transformation temperature range, 400°C~250°C. In lower bainite, cementite precipitates in two ways: from the carbon-enriched residual austenite and from supersaturated ferrite. In the second case, the cementite has the Bagaryatski orientation relationship with ferrite matrix:

$$[001]_{Fe3C} // [\bar{1}01]_{\alpha}, [100]_{Fe3C} // [111]_{\alpha}, [010]_{Fe3C} // [\bar{1}2\bar{1}]_{\alpha}$$

In lower bainite, cementite nucleates at the austenite/ferrite interface, so a unique variant of the orientation relationship should be taken, which will give an optimum match for both austenite and ferrite involved. Because of this, the cementite in lower bainite forms in parallel arrays about 60^{o} to the axis of bainite plate, which is different from that in tempered martensite.

2.1.1.7.5 Grain Boundary Allotriomorphic Bainite

When carbide precipitates in the grain boundary ferrite allortriomorphs in a process different from cooperative growth, which is what happens for pearlite, this bainite type microstructure is called grain boundary allotriomorphic bainite. Decreasing the initial austenite grain size will promote the formation of grain boundary allotriomorphic bainite by taking the place of upper bainite at a given transformation temperature.

2.1.1.7.6 Inverse Bainite

Inverse bainite is found only in hypereutectoid steels. Proeutectoid cementite forms first as an isolated plate or parallel plates. Ferrite will nucleate at the austenite-cementite interface and grow by consuming the austenite structure whose carbon concentration has been diminished by the formation of cementite. From the interface of austenite and ferrite a non-lamellar eutectoid mixture of carbide and ferrite will be formed. This is the morphology of inverse bainite as show in the Figure 2.2(f).

2.1.1.7.7 Granular bainite

Granular bainite is a term frequently used to describe the bainite that occurs during continuous cooling transformation. This terminology is used widely in industry, where most steels undergo nonisothermal heat treatments.

Granular bainite has the same mechanism of formation as the ordinary bainite. However, because the microstructure forms gradually during cooling, the sheaves of bainite can be rather coarse. The optical microstructure then gives the appearance of blocks of bainite and austenite, so that it is appropriate to use the adjective "granular".

A characteristic (though not unique) feature of granular bainite is the lack of carbides in the microstructure. Instead, the carbon that is partitioned from the bainitic ferrite stabilises the residual austenite, so that the final microstructure contains both retained austenite and some high carbon martensite in addition to the bainitic ferrite.

2.1.1.8 Martensite Martensite is an austenite transformation product, which is obtained when a very fast cooling rate (for example, rapid quench) is applied. The martensite reaction is usually an athermal process. For a certain steel, there is a martensitic start temperature, M_S, which is not affected by the cooling rate if only the critical cooling rate is satisfied. Once the M_S is reached, the martensite reaction starts and will go further with cooling until a transformation finish temperature, M_f, is reached. Martensite in steels is a supersaturated solid solution of carbon in ferritic iron. It has a body-centered tetragonal structure. The lattice parameters of martensite are strongly affected by the carbon content of the parent austenite:

$$\frac{c}{a} = 1 + 0.045 \cdot wt\%C \qquad \textbf{2.1}$$

Based on the carbon content of the steel, three types of martensite are defined [17]. They are low carbon, medium carbon and high carbon martensite. Martensite has very high dislocation density.

2.1.1.8.1 Low Carbon Martensite

Low carbon martensite is usually referred to as lath martensite. This type of martensite is found in plain carbon and low alloy steels with carbon content up to 0.5wt%. The laths in low carbon martensite are grouped into packets and separated from each other by low angle boundaries. The habit plane of low carbon martensite is close to $\{111\}_\gamma$ and Kurdjumov-Sachs relations exist between austenite and low carbon martensite matrix: $\{111\}_\gamma // \{110\}_{\alpha'}$ and $\{1\bar{1}0\}_\gamma // \{1\bar{1}1\}_{\alpha'}$

2.1.1.8.2 Medium Carbon Martensite

Medium carbon martensite is also referred to as acicular martensite, even though its morphology is that of lenticular plates. Medium carbon martensite forms in isolation and can be concurrent with lath martensite in the range of 0.5%~1% carbon. Medium carbon martensite's habit plane is close to $\{225\}_\gamma$ and also has a Kurdjumov-Sachs relations with austenite matrix.

2.1.1.8.3 High Carbon Martensite

High carbon martensite has its habit plane close to $\{259\}_\gamma$ and its orientation relation to austenite changes from Kurdjumov-Sachs to Nishiyama-Wasserman relations: $\{111\}_\gamma // \{110\}_{\alpha'}$

and $<1\bar{1}2>_{\gamma}$ // $<1\bar{1}0>_{\alpha'}$. The morphology of high carbon martensite is heavily twinned lenticular plates, which are formed individually.

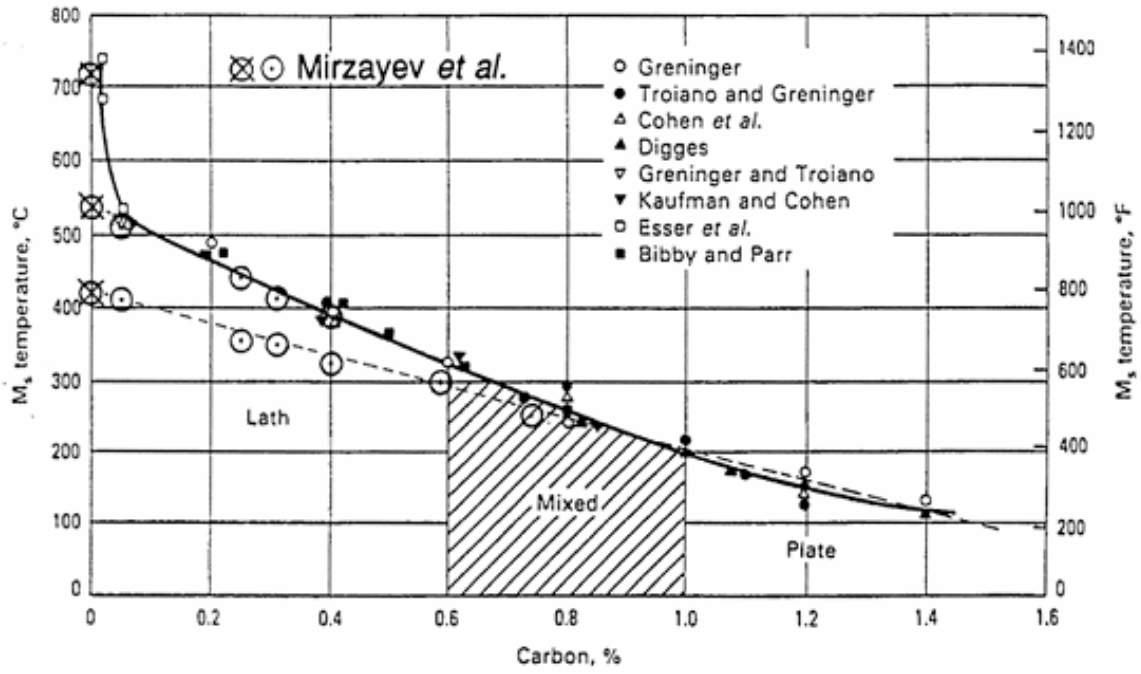

Figure 2.3 *Ms* vs. carbon concentration plot for plain carbon steels. [14]

The effect of carbon content on M_S is shown in the Figure 2.3 [14]. It was also found in some steels that the lath martensite transformation could be suppressed and replaced by twinned martensite at a higher cooling rate. Twinned martensite is the final transformation product before supercooled austenite is fully retained. If lath martensite is observed, twinned martensite can be finally formed by increasing the cooling rate; while lath martensite may or may not be found in steels containing twinned martensite by decreasing the cooling rate, because lath martensite can only be formed in low carbon and/or low alloy steels [24].

2.1.2 Kinetics and Mechanisms of Ferrite Formation

As mentioned in the previous section, various austenite decomposition products can be formed depending on the basic chemistry of steel and the temperature-time schedule employed. In this section, kinetics and mechanisms of austenite decomposition will be reviewed.

2.1.2.1 Basic Solid-Solid Phase Transformation Theory A phase is a portion of a system with homogeneous properties and composition, which is physically distinct from other parts of the system. The composition of a phase can be described by giving the relative amount of each component that makes up the whole system. When a phase transformation occurs, it means the initial state of the alloy is unstable compared to the final state. The stability of each phase is determined by its *Gibbs free energy* value, G, which is given by the following equation:

$$G = H - TS \qquad 2.2$$

where, H is the enthalpy; T is the absolute temperature and S is the entropy of the system. The value of enthalpy is actually the heat content of a system.

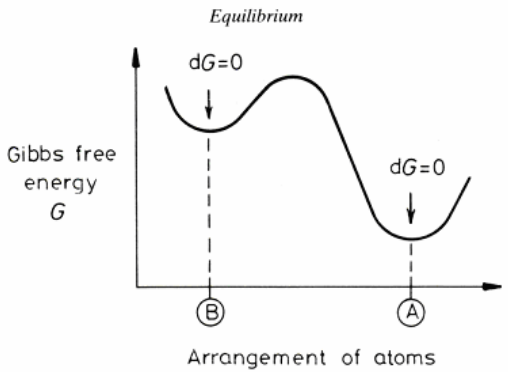

Figure 2.4 Schematic variation of Gibbs free energy with the arrangement of atoms [25].

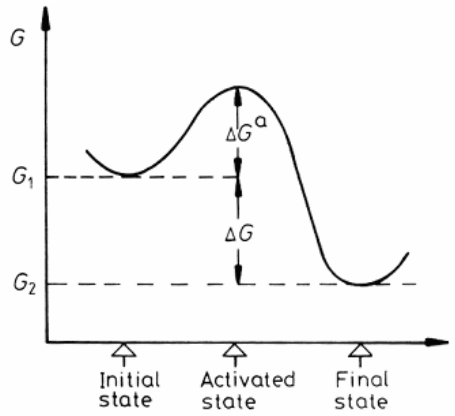

Figure 2.5 Transformation from initial to final state through an activated state of higher free energy [25].

At constant temperature and pressure, a closed system will be in stable equilibrium if it has the lowest possible value of the Gibbs free energy, or dG = 0. This definition is illustrated in the Figure 2.4 [25], in which A is the stable equilibrium state and B is called the metastable equilibrium state. Any transformation is possible only if it decreases the Gibbs free energy. That is: $\Delta G = G_2 - G_1 < 0$.

As shown in the Figure 2.5 [25], from G_1 to G_2 there is an intermediate state, called an activated state, which has its free energy designated by ΔG^a higher than G_1. ΔG^a is called the activation free energy barrier. The phase transformation rate is basically determined by the free energy hump between the metastable and stable states. The relation can be expressed as

$$\textbf{rate} \propto \exp\left(\frac{-\Delta G^a}{kT}\right) \qquad \textbf{2.3}$$

Solid-Solid phase transformation can be classified in a number of ways based on whether the transformation requires athermal growth or thermally activated growth [26, 27]. For a

diffusional phase transformation, nucleation is the step to start. Nucleation in solids is always heterogeneous. During heterogeneous nucleation, when a nucleus is created at a non-equilibrium defect, an interface is formed between the two phases and some free energy will be released (ΔG_d). Because of this new interface, a local variation in the interfacial energy (σ) is introduced. In addition, the difference in the molar volume of the parent and the decomposed phases will also lead to a change in elastic misfit strain energy per unit volume (ΔG_S). All of these energy changes make the transformation move from a less stable to a more stable state. The total free energy change of heterogeneous nucleation can be expressed as:

$$\Delta G = -V(\Delta G_V - \Delta G_S) + A\sigma - \Delta G_d \qquad \textbf{2.4}$$

where, ΔG_V is the volume free energy reduction of forming per unit volume of new phase; ΔG_S is the elastic misfit strain energy per unit volume; ΔG_d is the released free energy from the formation of an interface; σ is the local variation in the interfacial energy; V is the volume of the new phase and A is area of the new interface.

2.1.2.2 Austenite to Ferrite Transformation ($\gamma \rightarrow \alpha$) The austenite/ferrite transformation in Fe-C alloys and carbon steels involves a lattice structure change from fcc (γ) to bcc (α). As mentioned before, this phase transformation is a heterogeneous process, which starts from high free energy defects, like austenite grain boundaries and interfaces. Because of the limited solubility of carbon in ferrite, for most steels, this transformation is combined with a rearrangement of carbon through carbon diffusion. From this point of view, the growth kinetics of ferrite is widely accepted as a diffusion controlled issue. Interface velocity is also considered

in the ferrite growth rate. By assuming an infinitely fast diffusion of carbon in austenite, interface controlled ferrite growth kinetics is another extreme in the modeling of the $\gamma \rightarrow \alpha$ phase transformation. The real transformation reaction is under the combined effects of interface velocity and diffusive flux. Krielaart has done some work on this topic and proposed a mixed-mode model [28].

During continuous cooling with a relatively slow cooling rate, at the Ar_3 temperature, polygonal ferrite generally nucleates in the diffusional mode into an allotriomorphic shape from the austenite grain boundaries. The growth of nuclei is achieved by atomic transfer across the γ-α interface. At the coherent interface, growth is processed by the movement of steps along the interface. For polygonal ferrite, the growth rate is controlled by the long range diffusion of solutes in local equilibrium with the parent austenite phase [29]. At lower transformation temperature, quasi-polygonal ferrite may be formed through a composition-invariant mode [29].

Widmanstätten ferrite is generally formed with anisotropic growth from allotriomorphic ferrite pre-nucleated on the austenite grain boundaries. The growth of Widmanstätten ferrite is also considered to be in the diffusional mode [29].

2.1.2.3 Austenite to Bainite Transformation ($\gamma \rightarrow B$) All bainite reaction models can be grouped into two solid state transformation modes: displacive mode and diffusional mode (reconstructive mode) [22, 23, 30].

By the displacive mechanism, the bainitic ferrite is considered to grow by the propagation of discrete martensitic sub-units. These sub-units are clustered to form a sheaf-like microstructure. Bainitic ferrite is formed with carbon super-saturation. Immediately after the formation of bainitic ferrite, carbon will diffuse to the residual austenite. This may cause carbon concentration

around the austenite/ferrite interface to rise and could possibly lead to an incomplete transformation phenomenon or stabilized retained austenite, which will be reviewed in later sections.

A diffusional mechanism is used to describe transformations whose unit atomic process is the biased, diffusional jumps of individual atoms. This mechanism in the bainite reaction is strongly supported by Aaronson and his co-workers [23]. In some of their papers, their opinion has been strongly and carefully defended [22, 31].

The growth of bainite has several distinct steps [17, 30]. During continuous cooling, when the B_s temperature is reached, individual platelet ferrite nucleates and grows at the austenite grain boundaries. The displacements that occur during growth represent an invariant plane strain (IPS) with a large shear component. The growth of the platelet is stopped by the dislocation debris created by the deformation within the austenite. Subsequent individual platelets will nucleate at the tips of pre-formed ones. As this process continues, the sheaf structure will be developed. This procedure is illustrated in the Figure 2.6 [17, 30], which has morphology like that of upper bainite. It was found that the time required to grow a subunit (platelet) is small relative to that needed to nucleate successive subunits and the growth rate of individual platelets is much faster than the lengthening rate of sheaves [32].

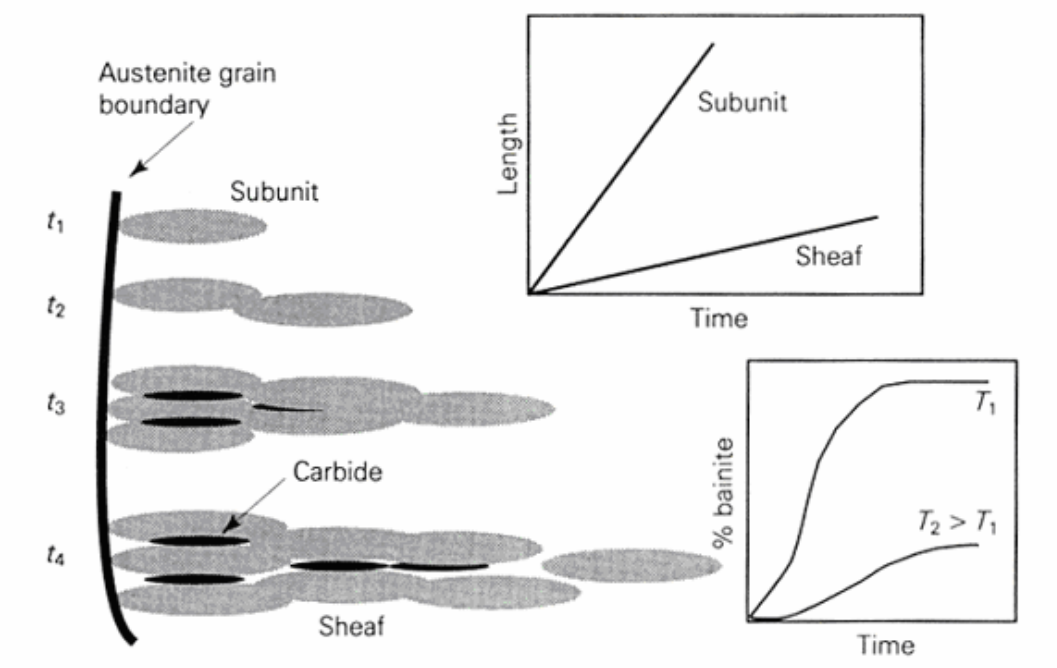

Figure 2.6 Schematic illustration of the microstructural features relevant in the kinetic description of a bainite microstructure [17].

2.1.2.4 Austenite to Martensite Transformation (γ→M) Martensite can be divided into two main categories: athermal martensite and isothermal martensite [33]. For athermal martensite, it can only grow athermally, i.e. the reaction proceeds as the result of changing temperature, and the amount of martensite formed is only a function of the temperature to which the steel is cooled and is independent of the time of holding at that temperature. Isothermal martensite transformation proceeds with time held at the transformation temperature. Since isothermal martensite is only produced in a few steel systems, especially in high alloy steels, our review here will be focused on athermal martensite.

The driving force for the start of martensite transformation can be expressed as $T_0 - M_S$, where T_0 is defined as the temperature at which strain-free austenite and martensite have the

same free energy. Supercooling is required for the martensite transformation to be started. A larger driving force ($T_0 - M_S$) will introduce larger temperature range, M_S -M_F, and larger shape change.

Martensitic transformation has a lattice correspondence. This means each atom in the parent phase can be related to a corresponding atom in the product phase. In a particular transformation, the correspondence applied is usually the one that introduces the smallest atomic displacements and consequently the lowest strain energy.

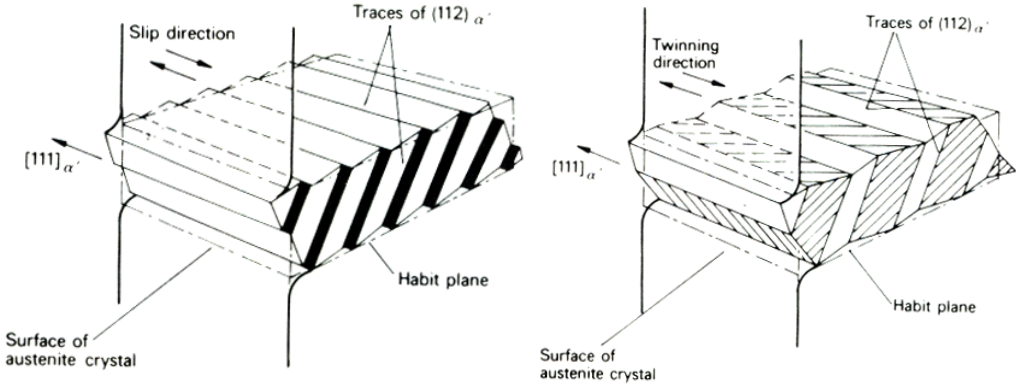

Figure 2.7 Formation of martensite plate, illustrating two types of lattice deformation: slip and twinning [17, 34].

There are two types of lattice invariant deformation happening during martensitic transformation: slip and twinning, which are shown in the Figure 2.7 [34].

2.1.2.5 Incomplete Austenite Decomposition The incomplete transformation phenomenon may be described as the formation of a significantly smaller proportion of ferrite than allowed by the Lever Rule at a given isothermal reaction temperature [31, 35]. As mentioned before, three quite different definitions of bainite are being used in the literature: the overall

reaction kinetics definition, the generalized microstructural definition and the surface relief definition. Based on these definitions, many theories on the phenomenon of incomplete transformation have been developed and discussed [36-40]. In this section, these theories will be reviewed.

2.1.2.5.1 Wever and Mathieu Theory

The earliest theory on incomplete transformation was proposed by Wever and Mathieu [41]. In this theory, the incomplete transformation phenomenon is explained as the result of elastic strain energy accumulation associated with the precipitation of bainite from austenite. The strain energy increases with the volume fraction of the transformation product until the free energy change accompanying the transformation is no longer large enough to support the reaction. This theory was not well developed. The main critique came from the idea that the elastic strain associated with bainite precipitation should be relieved by plastic deformation at the temperature when incomplete transformation occurs [37].

2.1.2.5.2 Zener Theory and Bhadeshia-Edmonds Theory

The Zener theory is also one of the earliest theories on incomplete transformation, which is based on the overall reaction kinetics definition of bainite. Zener [40] derived an approximate relationship for the carbon concentration at which austenite and ferrite of the same composition have the same free energy in the absence of strain energy at a given temperature, which is termed T_0. Incomplete transformation is explained by the Zener theory as a result of rejecting carbon from supersaturated ferrite. Rejected carbon causes the carbon concentration in the

untransformed austenite to rise smoothly with time until the composition corresponding to T_0 is attained, when further formation of bainite is prohibited.

Critique on the Zener theory is based on two main points [22]. First, by this mechanism, ferrite growth rate is at a massive or martensitic transformation level, which is too fast and no valid evidence has been found to support this swift growth kinetics. Secondly, a film of cementite is suggested to form around the bainite by the Zener theory [40], which could inhibit further bainite growth and result in incomplete transformation. However, this film of cementite has never been observed.

Bhadeshia and Edmonds have made some contribution to the carbon enrichment explanation on incomplete transformation recently [38]. As they said [38], "The bulk of the partitioning of carbon into the residual austenite must occur after the initial formation event. If this represents the true nature of events, the bainite reaction can be expected to stop as soon as the austenite carbon content reaches a critical value, the magnitude of which would be near the T_0 curve, depending on the exact degree of partitioning occurring simultaneously with transformation. Such an interpretation would also explain the incomplete reaction phenomenon since, with decreasing temperature, the austenite can tolerate successively greater amounts of carbon before the formation of supersaturated ferrite becomes thermodynamically impossible." This explanation implies a sharp discontinuity in partial molar free energy at the γ/α interface during carbon diffusion, with which some other researchers disagree [23, 31].

2.1.2.5.3 Solute Drag-like Effect (SDLE) Theory

Aaronson gave an explanation of incomplete transformation as a special effect of certain alloying elements upon the proeutectoid ferrite reaction [19]. Some modifications have been made [36, 42] and "Solute drag-like effect" was termed by Bradley in1981 [42].

During the proeutectoid ferrite reaction in Fe-C-X alloys, substitutional alloying elements, which tend to segregate to γ/α boundaries, are swept up by the boundary during growth. The activity of carbon in austenite in contact with the boundary is markedly decreased by the presence of adsorbed X element, which also reduces the driving force for growth [37]. When this activity reduction is sufficient to produce a constant carbon activity in austenite, i.e. the carbon activity in bulk austenite in contact with the boundary is the same as that of carbon far away from boundary, growth stasis occurs [37].

As mentioned by Reynolds [36], an important distinction between SDLE and solute-drag models applied to grain growth is that the information on boundary composition is not required to determine the drag force in SDLE theory.

SDLE theory is also questioned by some researchers [43, 44]. Detailed defenses have been given by Aaronson and his co-workers [22].

2.2 NOVEL MICROSTRUCTURAL CHARACTERIZATION TECHNIQUES

2.2.1 Fractal Analysis

Grain size hardening functions basically through the obstacle effects of grain boundaries on the motion of dislocations. In other words, the grain boundary characteristics play a more important role in strengthening than just the average grain diameter, which is currently used in the Hall-

Petch equation. Additionally, because of the transformation temperature and formation mechanism, different kind of ferrite might have different grain boundaries; and the characterization of the ferrite grain boundaries might indicate the various kinds of ferrite. Fractal analysis is a tool providing more information on grain boundaries, which is needed for further understanding of strengthening mechanisms.

Fractal analysis is a technique pioneered by Mandelbrot to describe the shape of irregular objects occurring in nature [45]. In the past few years, this technique has been proven to be very useful to describe complex and geometrically irregular microstructures of metals and alloys [46-48] and especially grain boundary characteristics [49, 50].

The fractal dimension of an object is a function of its roughness. If a rough line is measured by tracing with certain step length, ε, the measured length of line will change with different step length used. The larger ε is, the smaller the line length. For a two-dimensional condition, a genuine method to determine the fractal dimension, D_S, is based on the fractal equation [45]:

$$P(\varepsilon) = a \cdot \varepsilon^{1-D_S} \qquad \textbf{2.5}$$

where P is the perimeter of the object; a is a constant and ε is the yardstick length (or step length). If P versus ε is plotted on a log-log plot, the fractal dimension D_S is given as:

$$D_S = 1 - k \qquad \textbf{2.6}$$

where k is the slope. This is so called yardstick method or structure walk technique [51, 52].

Another important concept in fractal analysis is the shape factor. Mandelbrot noted that natural objects, which are formed by the same process, would have a self-similarity, which is

independent of object size [45]. For objects of the same shape, the ratio of the perimeter, *P*, to the square root of the area, *A*, will have a constant value, which is called the shape factor.

$$F = \frac{P}{A^{1/2}} \qquad \textbf{2.7}$$

For self-similar irregular shapes, the above equation can be written with fractal geometry as:

$$F_D = \frac{P^{\frac{1}{D_R}}}{A^{1/2}} \Rightarrow \ln(A) = \frac{2}{D_R} \cdot \ln(P) - 2 \cdot \ln(F) \qquad \textbf{2.8}$$

where, D_R and F can be determined by measuring the slope and intercept of the plot.

D_R is called the fractal dimension calculated from the perimeter-area relation. The evaluation of the fractal dimension of the grain boundaries by means of the perimeter-area relation must be accompanied by methods allowing for the verification of the self-similarity of the structure [49].

Fractal analysis is a useful tool to describe the grain boundary characteristics, especially the grian boundary curvature, roughness and the grain shape. It provides information on some particular features of the microstructures; however it does not work as tool to quantify any of these particular features. Therefore, fractal analysis cannot be used to quantitatively describe microstructures. Additionally, fractal analysis also requires a huge amount of experimental work including several micrographic techniques with different magnifications, which makes it impossible for this technique to effectively describe microstructures.

2.2.2 Electron Backscatter Diffraction (EBSD)

Electron backscatter diffraction (EBSD) is based on the acquisition of diffraction patterns from bulk samples in the scanning electron microscope. Since in 1924 when Kikuchi first observed the Kikuchi lines in TEM and later in 1954 when the back reflected Kikuchi lines were obtained by Alam [53], it took people several decades to make the fully automated indexing of EBSD pattern possible, which is the most important effect of the emergence of EBSD as a metallographic technique. The rapid automated pattern analysis together with the control of the microscope beam or stage has made it possible for line or area scans of a sample surface to be accomplished rapidly and automatically. This brought out the term "orientation image microscopy", which has been widely used in extended fields for various purposes.

2.2.2.1 Description of the Technique As shown in Figure 2.8 [54], basic EBSD equipment includes a scanning electron microscope and an EBSD system. The EBSD acquisition hardware generally comprises a sensitive CCD camera, and an image processing system for pattern averaging and background subtraction. The EBSD acquisition software will control the data acquisition, solve the diffraction patterns and store the data. Additional software is required to analyze, manipulate and display the data.

EBSD is carried out on a specimen which is tilted between 60^{o} to 70^{o} from the horizontal. If a backscattered image is required from the tilted sample, additional backscattered electron detectors must be used and these are typically positioned close to the transmission phosphor screen.

The data required for quantitative microstructure analysis using EBSD are usually obtained in the form of an orientation map, as shown in Figure 2.9. There are several critical parameters

that must be controlled during the data acquisition: the speed of the data acquisition and the spatial and angular resolutions, which depend on a number of factors including the specimen, the equipment and the method of operation.

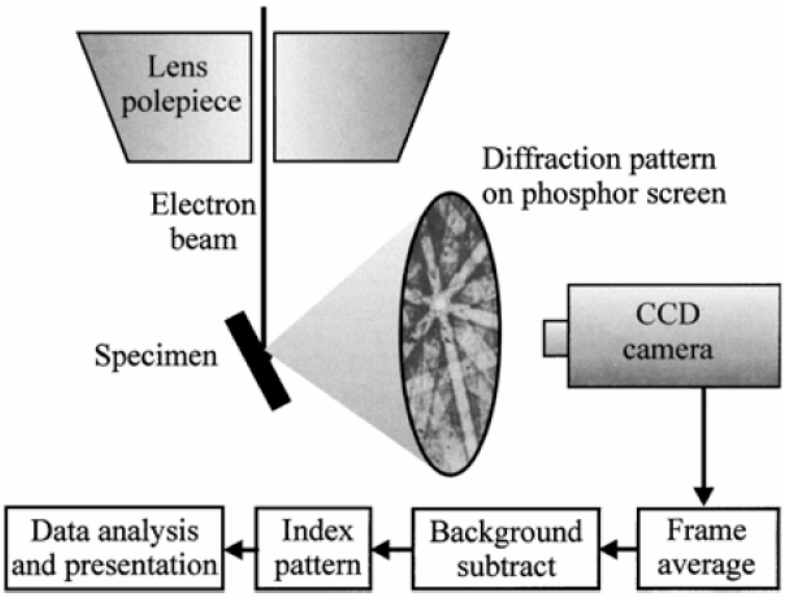

Figure 2.8 Illustration of EBSD system [54].

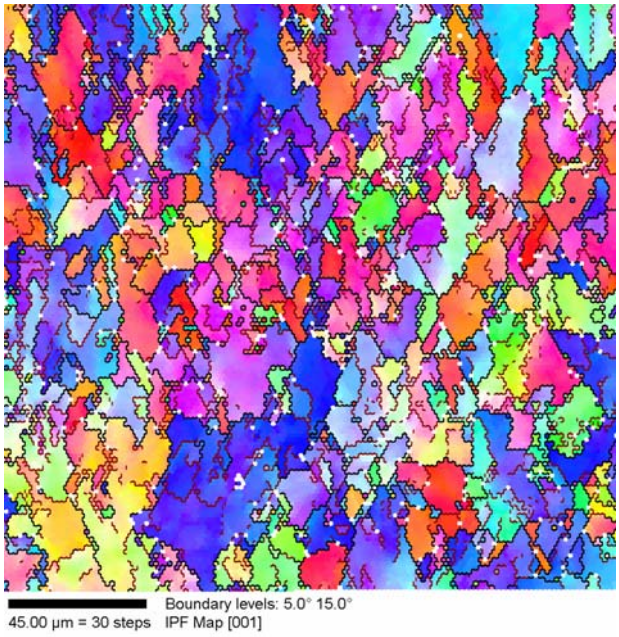

Figure 2.9 Orientation Map

Currently, EBSD acquisition systems are all standard commercially available equipment with no significant modifications. The application of EBSD to quantitative description of microstructure is strongly affected by the type, quantity and quality of the data which can be obtained.

For all EBSD systems, there are two types of scanning modes: beam scanning and stage scanning. In the beam scanning mode the normal microscope scan is disabled and the beam is controlled by the EBSD acquisition software. This mode is simple and requires no modification to the microscope. The beam scanning mode is also rapid because the time needed to remove the beam is negligible. The disadvantages of this mode are that during the scan, the beam moves off the optic axis and this can result in inaccuracy in the determination of absolute orientations and in beam defocus. However, under most conditions, these errors can be corrected or minimized by applying specially designed software and functions.

In the stage scanning mode a stationary electron beam is used and the specimen is moved relative to the beam with stage stepping motors controlled by the EBSD software. The obvious advantage of stage scanning is the elimination of beam defocus. However, because the stage movement is slower than beam scanning and, for normal SEM, the position accuracy with this mode is limited, the stage scanning mode is more time consuming and is most suitable for scan steps larger than 1 μm.

To accomplish a successful EBSD investigation, several factors have to be taken into account:

2.2.2.1.1 The specimen preparation

The backscattered electron signal varies with the atomic number (z) of the material. By increasing the z value, the signal, the quality of the pattern and the spatial resolution would be improved.

Since the diffraction pattern comes from the surface of the material, a properly prepared surface is always required. Usually, electropolishing is required. For some hard materials, however a fine mechanical polishing might also be sufficient.

2.2.2.1.2 The speed of data acquisition

The speed of data acquisition is initially determined by three consecutive operations.

The time required to obtain an analyzable diffraction pattern. This primarily depends on the material and microscope operating conditions.

The time required to analyze the pattern. This depends on the processing speed of the computer, the speed of the pattern-solving algorithm and number of lines in the pattern required for a resolution.

The time to reposition the beam or stage, which might be a significantly long time for stage scanning mode.

2.2.2.1.3 Spatial resolution

If the area of the sample contributing to a diffraction pattern contains more than one crystallographic orientation, e.g. a grain boundary region, a single crystal diffraction pattern is not obtained and the pattern might not be successfully indexed (or have a significantly low image quality and index confidence).

The area from which an EBSD pattern is acquired with an electron beam focused on a 70^{o} tilted sample is approximately elliptical, which is perpendicular to the tilt axis, being some 3 times that of the mirror axis, as illustrated in Figure 2.10. The spatial resolution is a function of material, beam accelerating voltage, specimen tilt and probe size.

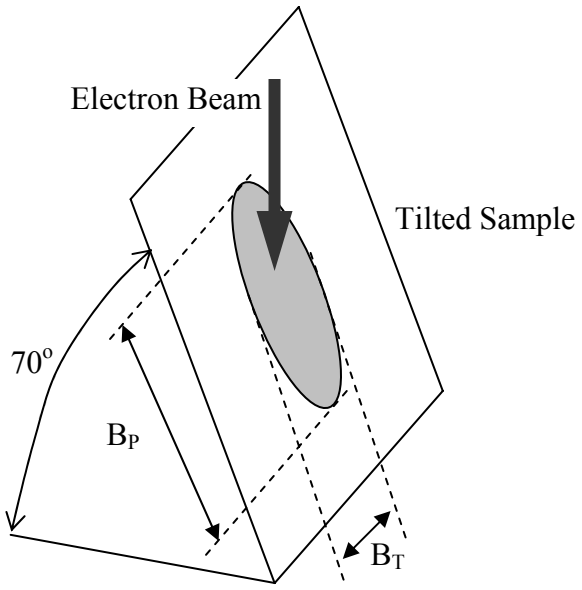

Figure 2.10 The geometry of the electron beam and the sample

While in practice, the achievable spatial resolution is rather smaller than those shown above, because most of the time there is still a significant difference in intensity of the patterns even if they are from two neighboring grains. Therefore, the pattern may still be analyzed successfully, while a reduced image quality would be introduced. In this case, the effective resolution could be determined by measuring the fraction of solved (or less affected) patterns (F_{Solved}) for grains of mean size D_P and D_T perpendicular and parallel to the tile axis. F_{Solved} can be approximately calculated by

$$F_{Solved} = \frac{(D_T - B_T)\cdot(D_P - B_P)}{D_T \cdot D_P} \qquad \textbf{2.9}$$

where B_P is the effective spatial resolution perpendicular to the tilt axis and B_T is the resolution parallel to the tilt axis and F_{Solved} is actually the area fraction of the grain whose diffraction patterns are ideally not affected by the grain boundaries, which is illustrated in Figure 2.11.

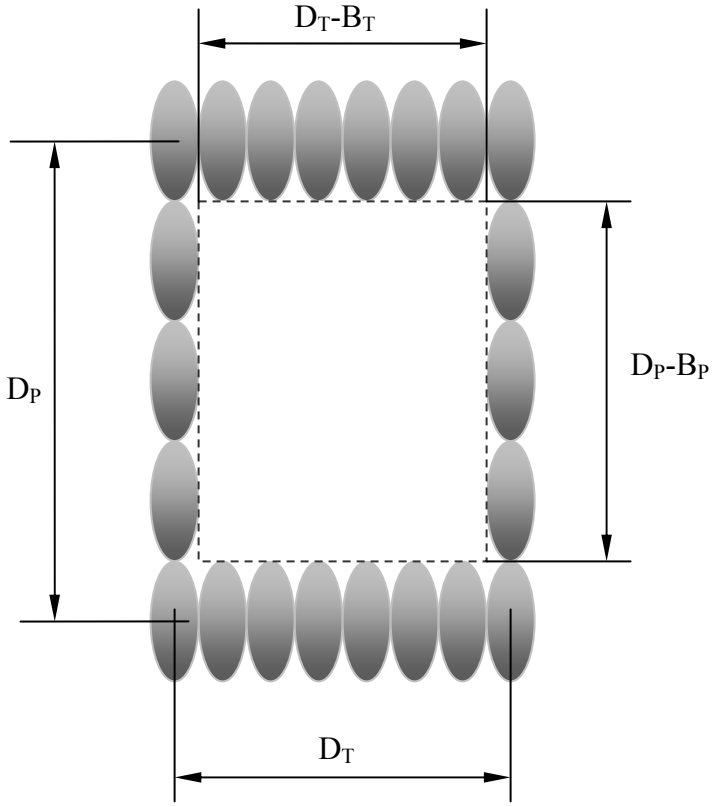

Figure 2.11 Illustration of F_{Solved}

The spatial resolution might be affected by numbers of factors. As Humphreys pointed out, the beam current and the frame length are two important factors [54] [55]. The influence of those two factors has been shown in Figure 2.12. An optimized probe current is expected for the best resolution. And, a minimum frame length of 8 or larger is also required for a satisfying resolution under the accelerating voltage of 15 keV.

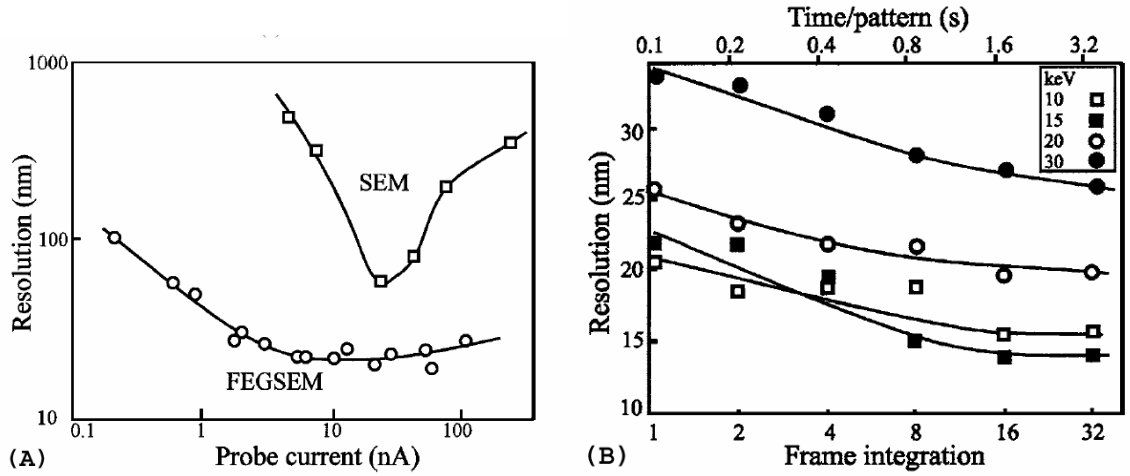

Figure 2.12 Probe current and frame integration vs. spatial resolution [54].

2.2.2.1.4 Angular precision

The absolute orientation of a crystallite is typically obtained with an accuracy of ~2°, depending on the sample alignment and EBSD operation conditions. The accuracy with which the relative orientation between adjacent data points can be determined is of great importance when analyzing microstructures containing significant amounts of low angle grain boundaries. The measured distribution of misorientation is the sum of the orientation noise and the real misorientation and therefore, very small misorientation (<2°) are difficult to be determined.

The angular precision is also affected by the microscope operation systems. Increasing probe current will decrease the angular resolution to a constant value, which is determined by the data acquisition system. When the accelerating voltage is increased, because the positions of the narrower Kikuchi bands are determined more accurately, the angular resolution will also be improved. For poor quality patterns, the angular precision may also be improved if the number of

lines measured from the diffraction pattern is increased, which will slow down the data processing rate. When the misorientation is expressed as an angle-axis pair, those inaccuracies mentioned above could introduce a large error in determining the misorientation axis.

The smallest misorientations between grains and subgrains, which can be determined by automated EBSD, are typically between 0.5° and 1.5°. The lower limit is achievable only from very high quality patterns using a well calibrated system. This limit could even be lowered when higher resolution cameras are employed and when more accurate algorithms for pattern measurement are developed.

The angular resolution could also be improved at the expense of spatial resolution by data processing. When there are a considerable number of data points in each grain, the orientation of the grain could be much more precisely determined by averaging all data points inside this grain. However, orientation averaging is only valid if the true orientation is constant within each grain or subgrain, and this should be considered before such procedures are used. Generally, as an example, annealed samples match that assumption very well, while for materials containing many free dislocations and poorly developed sub-boundaries, orientation averaging might not be a wise choice.

2.2.2.1.5 Non-indexed and incorrect data points

For many reasons, the diffraction patterns of some scan points may have very poor quality. Sample surface defects, grain boundaries and phase boundaries all could introduce a poor pattern quality and therefore non-indexed data points. The amount of these non-indexed data points is critical in obtaining quantitative microstructural data. Even non-indexed data points could be "repaired" by assigning the orientation of a neighboring point or an averaging orientation from

their neighbors, too much caution is needed in using this procedure. On the other hand, those non-indexed data points could possibly be analyzed as a source of information about those defects and interfaces.

Diffraction patterns could also be wrongly indexed when the pattern quality is low as well as when the pattern is symmetrical. In cubic metals, wrong indexing is rare for a well calibrated system and mis-indexed points generally appear as isolated pixels on an orientation map and as they typically have high misorientation to the adjacent pixels they can often be recognized. Wrongly indexed data points can be reduced by increasing the pattern quality, improving calibration and using a large number of bands for pattern solution.

2.2.2.2 Application of EBSD The EBSD technique had been applied to the metallurgical research field for over a decade. For many materials with a relatively simple crystallographic structure (e.g. aluminum and steels), EBSD data can be collected very quickly and with a high degree of reliability. The technique can be used for a wide range of applications [56-61], ranging from routine grain size and texture characterization, to detailed phase identification of boundary precipitates. In this section a selection of the typical applications of EBSD in metallurgy will be reviewed.

2.2.2.2.1 Measuring grain or subgrain size

Grain size is an important microstructural feature, which has been used in quantitative metallography for mechanical property rationalization and prediction. Grain size and subgrain size can be measured by using EBSD through either the linear intercept method or the grain reconstruction method.

In the linear intercept method, the grain boundaries are usually defined as those interfaces with high angle misorientation (>15°). Compared to SEM imaging, which reveals both high and low angle misorientation interfaces, the results of grain size measurement from EBSD is usually larger.

In the grain reconstruction method, beyond the definition of grain boundary as high angle misorientation, a grain is also defined as a region containing materials which is within a (small) specified orientation range. Usually both of those two definitions give similar grain size measurement. For microstructures with a significantly high fraction of low angle grain boundaries, the latter definition will provide a smaller grain size.

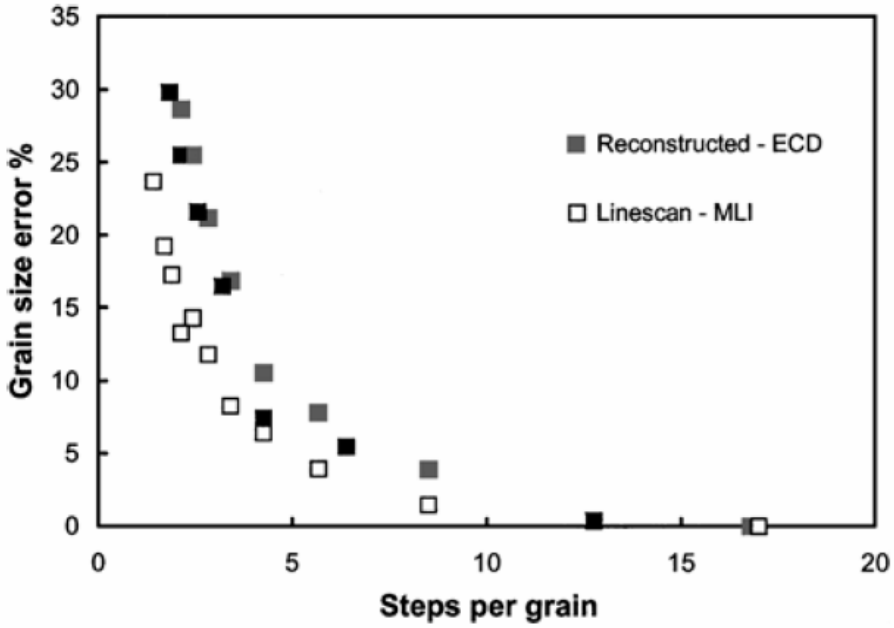

Figure 2.13 Grain size error Vs. Steps per grain [54].

The accuracy of grain size measurement is affected by several factors. Beyond the spatial resolution and the angular precision mentioned in previous sections, the scanning step size is another important factor. As shown in Figure 2.13, to obtain an accuracy of 10% for grain size measurement, at least 5 scan points should be included in a grain; an increase of the accuracy to 5% requires an average minimum scan point of about 8 to be included in each grain.

2.2.2.2.2 Texture analysis

If grain size measurement is just a job all traditional techniques can do and EBSD is just doing better, texture analysis is a specific and powerful function particular to EBSD. Textures are conventionally determined by the analysis of pole figures which are obtained from a sample by x-ray diffraction and quantitative orientation distribution (ODFs) are obtained from analysis of 3 or 4 pole figures. Such procedures are fully automated and as the time to obtain a single pole figure is typically ~1.5 hours, the data acquisition time for a specimen is approximately 4~6 hours. There are certain errors in the experimental x-ray procedure such as line broadening and in the data analysis, which lead to inaccuracies in calculating orientation distribution functions. Fully automated EBSD analysis has eliminated such errors by obtaining the crystallographic texture of a specimen directly from individual diffraction patterns. And, texture analysis by EBSD is a significant time saving technique compared to the conventional x-ray analysis.

Another benefit of using EBSD in texture analysis is that a whole information package can be gained about the microstructure. That is all the information about the grain size, grain boundaries, as well as the texture (orientations), collected simultaneously and their correlation and interaction can also be analyzed.

2.2.2.2.3 Boundary characteristics

Some of the most important parameters which can be determined from EBSD are related to the nature of the grain boundaries. A boundary is characterized by five degrees of freedom, three of which relate the orientation of the material on either side of the boundary and two degrees of freedom which define the inclination of the plane of the boundary.

Misorientation, also termed disorientation, is one parameter which is most often used to describe the angular relationship between the crystals. When the angle-axis pair is used to describe grain boundaries, the misorientation is defined as the smallest angle, by which one crystal could rotate about a particular axis so as to bring it into register with the other crystal. By calculating the misorientation of all grain boundaries, EBSD can easily provide the information about the distribution of boundary angles. The profile of the distribution as well as the fraction of high (or low) angle grain boundaries might be relevant to the properties of the material and be useful in microstructural analysis.

Since the information on orientation is fully collected, EBSD analysis can also detect and measure grain boundaries with special orientation relationships. As an example, the properties of coincident site lattice (CSL) boundaries have been successfully studied by using EBSD [56, 60].

2.2.2.2.4 Microconstituent identification

In this application, the microconstituent could be different phases with various crystal structures or the same phases with different stored energies and/or defect densities. For different phases, EBSD could identify them by their crystal structure, which can be determined through the diffraction pattern. For the same phases, the identification might require information on the boundary characteristics. Today, the widest usage of EBSD in microconstituent identification is

about measuring the recrystallization fraction. A more detailed description of this application will be reviewed in the next section.

2.2.2.3 Theory about Image Quality and its Application Image Quality (IQ) value is an important parameter derived from the EBSD technique, which assesses the sharpness of EBSD patterns. A better pattern gives a more reliable determination of the sample orientation. A map of image quality, therefore, can reveal areas in which the orientation data are suspect. The image quality (IQ) parameter provided by commercial EBSD suppliers is based on the intensity of the peaks in Hough space, representing the strength of the detected Kikuchi bands [62]. As illustrated in Figure 2.14, for the ideally perfect lattice, row I, there is a high Kikuchi band intensity and therefore, diffraction pattern with high sharpness and high IQ value is expected; while there are defects exist, low Kikuchi band intensity and low IQ value are observed as shown in row II. Image Quality is a direct measure of Kikuchi band intensities that determines the quality of an electron backscatter diffraction pattern. Since the defects and distortions of the crystal lattice within the diffraction volume could significantly affect the intensity of the Kikuchi band, IQ values are also related to the lattice structure features. This is the initial idea of using IQ analysis as a tool to characterizing microstructures.

IQ is dependent on the material and condition. It is a function of the technique and parameters used to index the pattern as well as other factors such as the video processing. Therefore, changing conditions in the microscope or video processing, such as simply changing the contrast and brightness, will affect the IQ value.

The EBSD spatial resolution is also believed to be an important factor affecting the IQ value. Humphreys gave a detailed review on the effects of spatial resolution as well as step size used during scanning on grain boundary analysis and IQ values [54]. It could be simply concluded that

higher spatial resolution gives higher IQ values and a minimum of eight scan spots per grain is required for an accurate measurement with the error lower than 5 percent.

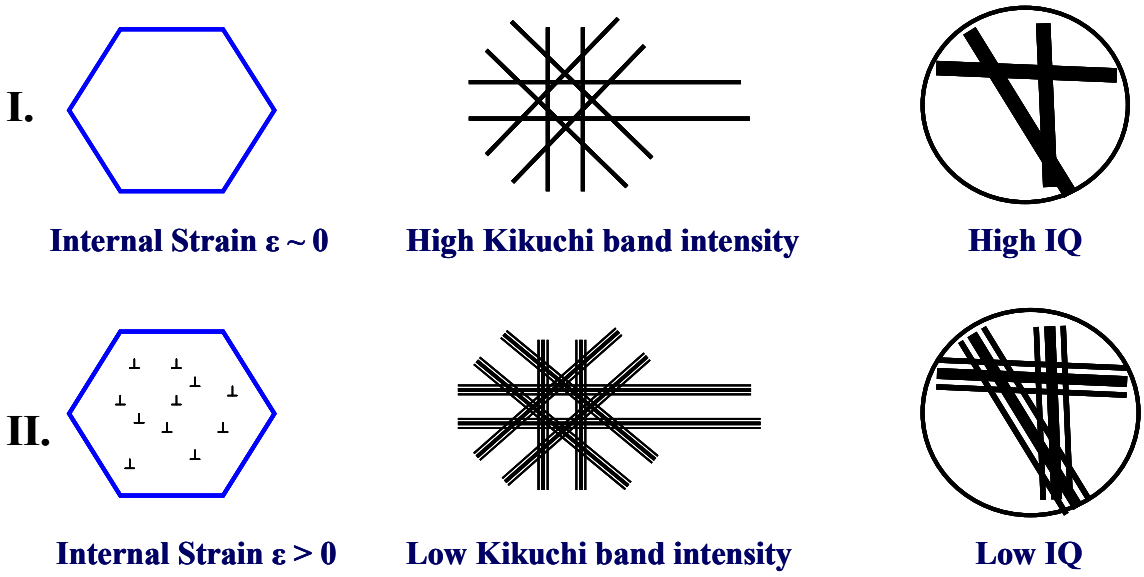

Figure 2.14 Illustration of the correlation of the lattice imperfection, Kikuchi bands and the Image Quality.

As Humphreys and Okuda both pointed out [54, 61], because different bands of varying intensity will appear depending on the orientation, orientation dependence of the IQ value is reasonably expected. However, in the example given by Humphreys, this variation in IQ caused by orientation can hardly be detected. Compared to other affecting factors, orientation might not give any significant contribution to the IQ values.

The greatest effect on IQ, which makes EBSD and IQ analysis useful tools in phase/microconstituent identification and quantification, is the perfection of the crystal lattice in the diffracting volume. Distortions of the crystal lattice within the diffracting volume lower the quality of diffraction patterns (more diffuse), so a lower IQ value is expected. Currently, based

on this, there are two major applications of EBSD/IQ analysis. One application is to quantify the recrystallization fraction and the other one is to quantify the ferrite fraction in some martensite + ferrite, $\alpha' + \alpha$, microstructures.

Generally, there are three methods to estimating the recrystallization fraction from EBSD data. The first one is similar to the optical microscopy, which is based on the grain shape and appearance. The second one is based on the misorientation, which is the original idea about recrystallization analysis using EBSD and has been used in some commercial software. The third method is the IQ analysis. In the unrecrystallized and/or partially recrystallized area, because of the higher defect density compared to the recrystallized region, a detectable reduction of image quality is expected, and therefore, given a suitable choice of threshold, the fraction of recrystallization can be determined as the area fraction of high IQ regions.

Mitsche and Rollett [58, 63] have given two examples of using IQ mapping analyzing recrystallization fraction. In Rollett's work [63], the confidence index (CI) was introduced for evaluating recrystallization fraction together with IQ values. Unrecrystallized pixels were linked to low CI and IQ. Errors in indexing were minimized by incorporating isolated unrecrystallizated pixels into surrounding recrystallized regions. That is, that a point can be considered as recrystallized if it has at least four recrystallized nearest neighbors, or three of its nearest neighbors are within 3º of the same orientation. This work increased the accuracy of the estimation of recrystallization fraction by involving the CI value. However, the grain boundary effects, which may cause errors as mentioned by Mitsche [58], were not even considered in Rollett's work.

Wilson and Spanos [64, 65] started using IQ analysis to quantify the ferrite fraction in some $\alpha' + \alpha$ microstructures in steels. The basic idea is similar to that of recrystallization fraction

evaluation. A significant low IQ area is expected to be associated with the martensite region, because of its extremely high dislocation density and the retained strains introduced during its formation. In Wilson's work, a certain threshold IQ value was simply selected from the IQ distribution profile and was used to divide the whole measurement points into two regions, representing the martensite and the ferrite fractions, respectively. They found this technique is feasible only for certain microstructures, for which two peaks appear in the IQ distribution profile, as expected, while it fails if there is only one peak found. As a suggestion to enforce this technique, they predicted that using IQ analysis combined with the orientation information might lead to a much improved result. However, there is no proven work supporting it and no detailed introduction on how to do it. The important points missed by Wilson [64, 65], which were also overlooked in the work on estimating recrystallization fraction, are the GB effects and the histogram of IQ. Ignoring the grain boundary effect might introduce error to the estimated results, while ignoring the histogram of IQ might provide totally wrong results. The typical IQ histogram should be a symmetric bell-shape distribution [66]. The overall histogram of IQ is a sum of all bell-shaped distributions from different phases and/or microconstituents. From this point of view, IQ analysis may still be feasible even for the condition with only a single peak detected, under which Wilson's technique has failed.

2.2.3 Atomic Force Microscopy (AFM)

The atomic force microscope (AFM), or scanning force microscope (SFM), was invented in 1986 by Binnig, Quate and Gerber [67]. Like all other scanning probe microscopes, the AFM works by measuring a local property - such as height, optical absorption, or magnetism - with a probe or "tip" placed very close to the sample. The small probe-sample separation (on the order

of the instrument's resolution) makes it possible to take measurements over a small area. To acquire an image, the microscope raster scans the probe over the sample while measuring the local property in question. The resulting image resembles an image on a television screen in that both consist of many rows or lines of information placed one above the other.

Unlike traditional microscopes, scanned-probe systems do not use lenses, so the size of the probe rather than diffraction effects generally limits their resolution.

2.2.3.1 Theory relating AFM and its Classification Figure 2.15 illustrates how this works: as the cantilever flexes, the light from the laser is reflected onto the split photo-diode [67]. By measuring the difference signal (A-B), changes in the bending of the cantilever can be measured.

Since the cantilever obeys Hooke's Law for small displacements, the interaction force between the tip and the sample can be found. The movement of the tip or sample is performed by an extremely precise positioning device made from piezo-electric ceramics, most often in the form of a tube scanner. The scanner is capable of sub-angstrom resolution in x-, y- and z-directions. The z-axis is conventionally perpendicular to the sample.

The AFM can be operated in two principal modes: with or without feedback control [68].

In the case with feedback, the positioning piezo, which is moving the sample (or tip) up and down, can respond to any changes in force which are detected, and alter the tip-sample separation to restore the force to a pre-determined value. This mode of operation is known as *constant force*, and usually enables a fairly faithful topographical image to be obtained (hence the alternative name, *height mode*).

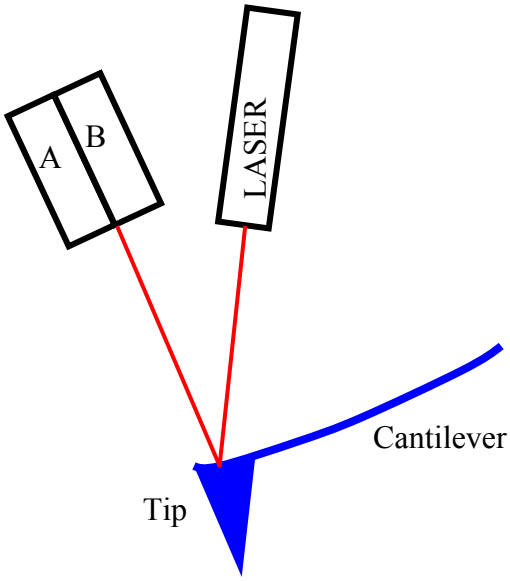

Figure 2.15 Illustration showing how AFM works [67].

When the feedback electronics are off, the microscope is said to be operating in *constant height* or *deflection* mode. This is particularly useful for imaging very flat samples at high resolution. Often it is best to have a small amount of feedback-loop gain, to avoid problems with thermal drift or the possibility of a rough sample damaging the tip and/or cantilever.

The three major modes of tip-sample interaction, which give the image contrast, are *contact mode*, *tapping mode* and *non-contact mode* [68, 69].

Contact mode is the most common method of operation of the AFM. As the name suggests, the tip and sample remain in close contact as the scanning proceeds.

One of the drawbacks of remaining in contact with the sample is that there exist large lateral forces on the sample as the tip is "dragged" over the specimen.

Tapping mode is the secondly most common mode used in AFM. When operated in air or other gases, the cantilever is oscillated at its resonant frequency (often hundreds of kilohertz) and

positioned above the surface so that it only taps the surface for a very small fraction of its oscillation period. While in contact with the sample, the time over which this contact occurs is very short, which means that lateral forces are dramatically reduced as the tip scans over the surface. When imaging poorly immobilized or soft samples, tapping mode may be a far better choice than contact mode for imaging.

There are more methods of obtaining image contrast with the tapping mode. For example, in constant force mode, the feedback loop adjusts so that the amplitude of the cantilever oscillation remains (nearly) constant. An image can be formed from this amplitude signal, as there will be small variations in this oscillation amplitude due to the control electronics not responding instantaneously to changes on the specimen surface.

More recently, there has been much interest in phase imaging. This works by measuring the phase difference between the oscillations of the cantilever driving piezo and the detected oscillations. It is thought that image contrast is derived from image properties such as stiffness and viscoelasticiy.

Non-contact mode [70]. In this mode the cantilever must be oscillated above the surface of the sample at such a distance that we are no longer in the repulsive regime of the inter-molecular force curve. This is a very difficult mode to operate in ambient conditions because the thin layer of water contamination on the surface of the sample will invariably form a small capillary bridge between the tip and the sample and cause the tip to "jump-to-contact".

2.2.3.2 Application of AFM to Study the Microstructure of Steels

The main application of AFM is imaging of structures on a sub-micrometer to nanometer scale, where optical microscopy is no longer usable. AFM has been widely used in many fields such as

surface analysis, thin film processing, microelectronic analysis and so on. Recently, the AFM technique started being used in microstructural analysis of multiphase steels [71].

In Yanez's work [71], AFM has been used to characterize the microstructure of a series of TRIP steels. Topography information has been collected from all samples. In the case of dual-phase samples, the higher areas in the sample correspond to the martensite and the lower areas correspond to ferrite. The inhomogeneity among martensite areas is explained as the result of the inhomogeneous chemical distribution in the prior austenite grain. For the multiphase samples, three types of regions have been successfully detected by using topographical analysis. The martensite/retained austenite occupied the highest area and the ferrite stayed in the lowest areas. Bainite is located in the intermediate areas.

2.3 COMPLEXITY OF HSLA STEEL MICROSTRUCTURES

Various austenite decomposition products have been summarized in the previous sections. As an example [72, 73], the complexity of the HSLA steel hot band microstructures will be discussed in this part of the study. The initial objective of this work was to correlate the processing conditions with the mechanical properties. However, the complexity of the hot band microstructures has turned out to be more important issue to be understood before any further progress.

2.3.1 Material Studied

A 70 ksi (480 MPa) grade HSLA steel was used. The raw material, which is a commercial, 250mm, as-cast slab material, was provided by Rouge Steel Company. The composition is shown in the Table 2.1.

2.3.2 Hot Rolling Experimental Design

In the hot rolling experiment, the to-be-deformed block has an orthorhombic shape with 51x76x102mm^3 dimension, as shown in Figure 2.16. A hole is made from the side surface to the center on each block, into which a thermocouple can be inserted, so that temperature change during processing can be traced.

The experimental plan of hot rolling is shown in the Figure 2.17. For each path, there are three passes of deformation. The first two passes are considered as rough rolling and the last pass as simulating the finish rolling. The roughing temperature is defined as the temperature exactly before the first pass starts. The reduction and true strain of each pass are shown in the Table 2.2.

Table 2.1 Key Chemical Analysis of the HSLA Steel under Study.

Bulk Content, ppm.						
C	Mn	S	N	Nb	Ti	V
780	13,000	32	43	380	-	500

Table 2.2 Deformation schedule of hot rolling experiment

Pass	Thickness, inch	Reduction, pct	True Strain
	2.00	-	-
R1	1.00	50	0.69
R2	0.50	50	0.69
F1	0.25	50	0.69

The initial hot rolling experiment completed at the USX Technical Center has provided hot-band samples for totally twenty-four combinations of the processing conditions, as indicated in Figure 2.17. For the combinations, "1" represents the lowest condition level and larger number means higher temperature. For example, condition 1231 means low reheating temperature, high roughing temperature, high finishing temperature and low coiling temperature. The objective processing conditions for 1231 can be easily found to be that the reheating temperature is 1200^{o}C; the roughing temperature is 1150^{o}C; the finishing temperature is 1000^{o}C and the coiling temperature is 550^{o}C. The real processing conditions are given in Table 2.3. In addition to single samples for the twenty-four conditions, replicates were conducted for the conditions 1122, 1212, 1222, and 1232.

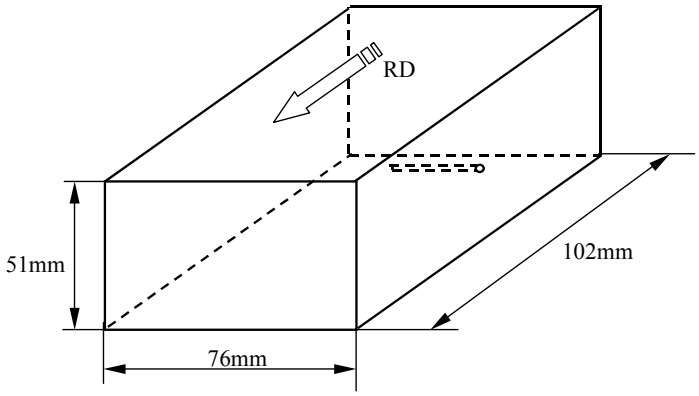

Figure 2.16 Dimensions of the specimen for hot rolling experiments

The Grain Coarsening Temperature (GCT) and the Recrystallization Stop Temperature (RST) [72] were determined in the laboratory using the Mechanical Testing System (MTS) before the rolling experiment to ensure the selected temperatures are suitable for the purpose of examining the effect of processing variability.

To determine the (GCT), encapsulated specimens were heated and held for one hour at temperatures from 950°C to 1300°C (1742 to 2372°F) with an interval of 50°C over that range and then water quenched. To help reveal the initial austenite grain boundaries, tempering of the quenched samples at 500°C for 24 hours was employed. The measured grain sizes are shown in Figure 2.18 and the typical microstructures are shown in Figure 2.19. From measurement of the prior-austenite grain sizes, it is found that the austenite grain coarsening occurs around 1075°C. As Palmiere concluded [74], the dissolution temperature is approximately 125°C higher than the austenite coarsening temperature. Thus, it is concluded that the grain boundary inhibiting precipitates will be completely dissolved or coarsened at even the lowest reheat temperature of 1200°C for the hot rolling experiment. The austenite grain size difference is expected to be the main source of variation in the reheating stage.

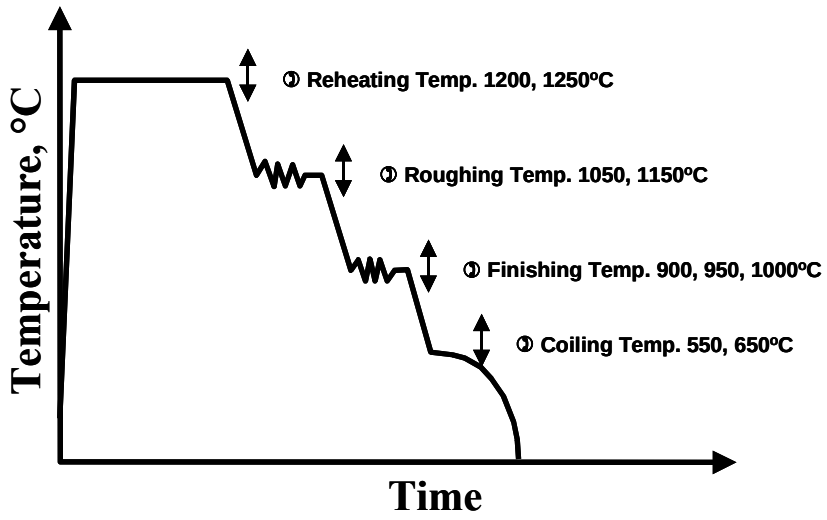

Figure 2.17 Hot rolling experimental plan for the commerical HSLA steel

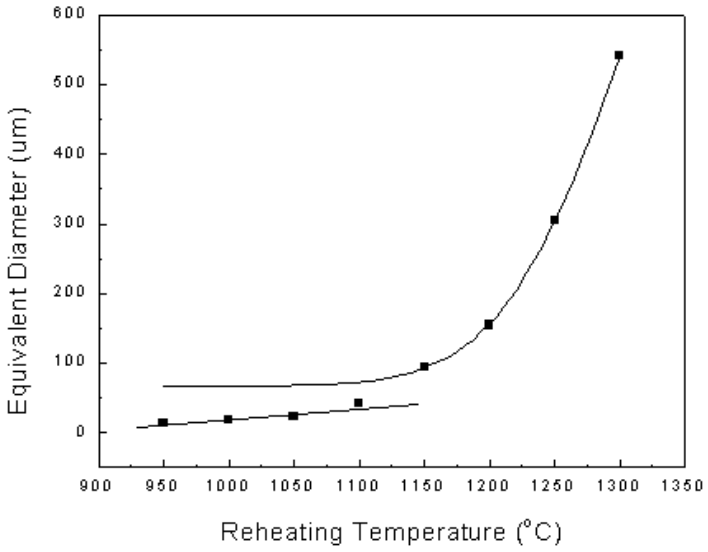

Figure 2.18 Austenite grain sizes of the under-study HSLA steel after being held at different reheating temperatures for 60 minutes.

To determine the RST of this steel, the samples of the as-cast slab material were heated and held for one hour at 1250°C, cooled to "finishing" temperatures at 50°C intervals in the range of 900 to 1100°C, deformed 30 pct and held for one second before quenching. According to the microstructures of the quenched samples, it was found that the start of the recrystallization of the deformed austenite occurred at about 925°C. At 1000°C with 30 percent deformation, deformed austenite was found to be fully recrystallized.

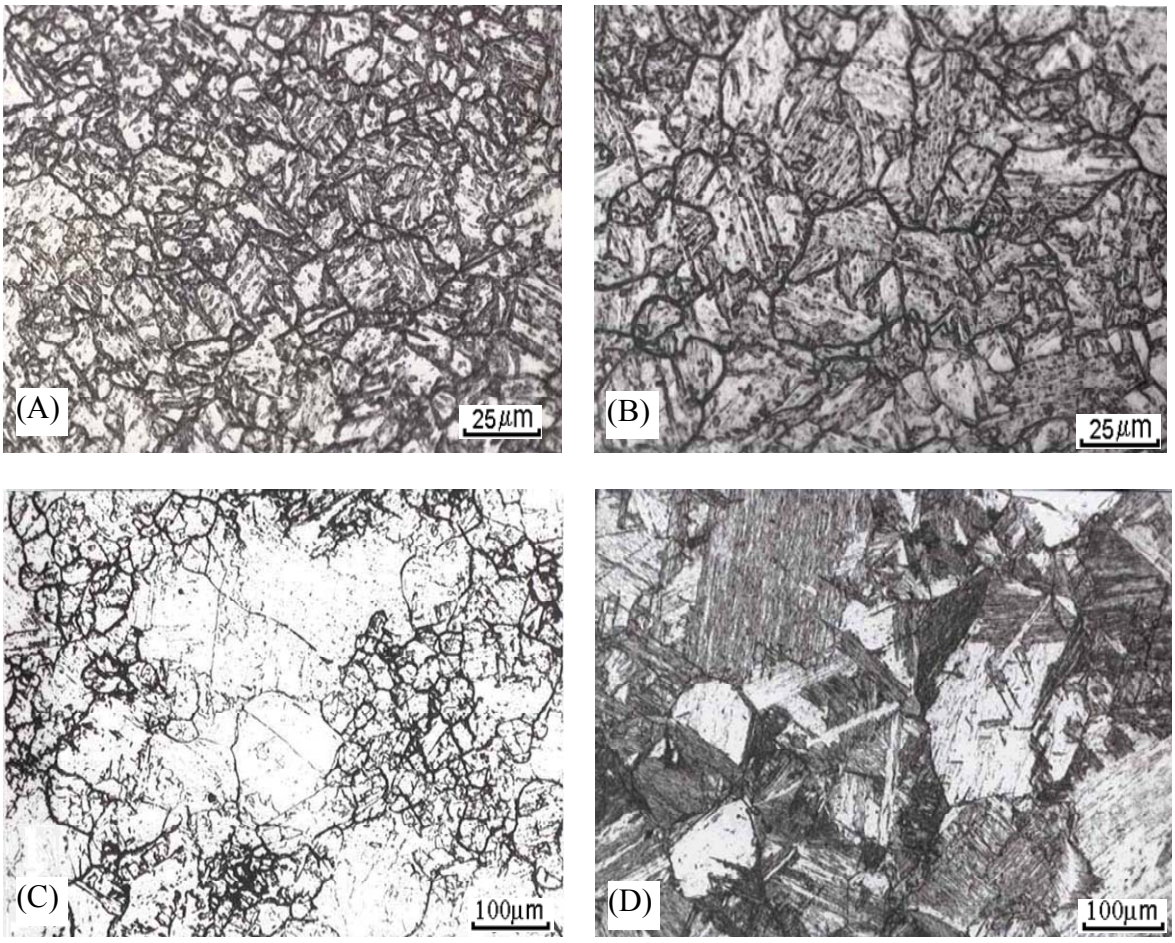

Figure 2.19 Microstructure of specimens reheated and held 60 minutes at temperatures: (A) 950°C, (B) 1050°C, (C) 1100°C, (D) 1150°C followed by water quenching to room temperature.

With the experimentally determined values of GCT and RST, it was agreed that the temperature levels of the experimental plan would be satisfactory.

2.3.3 Microstructural Analysis

2.3.3.1 Optical Microscopy Optical microscopy was used for examination and identification of the different phases and microconstituents. In the hot rolling experiment, the samples were cut perpendicular to the rolling plane and mounted in Bakelite. The specimens

were ground using 180, 240, 320, 400 and 600 grit abrasive papers in this order, and polished with 1.0 μm and 0.05 μm alumina paste. The polished sample was etched using 2% nital for 10-15 seconds. To reveal the initial austenite grain boundaries in the quenched samples, saturated picric acid solution is used. The solution is heated to 70~80°C and stirred. Samples are immersed in the solution for approximately 2 minutes to obtain the best appearance. LePera etchant was also used to identify some special microstructures [75].

Measurements of grain size and volume fractions of microconstituents were performed using a computer controlled Bioquant IV system attached to an optical microscope. More than 200 grains were measured by manually tracing the grain boundaries to obtain a statistically reliable grain size.

2.3.3.2 Scanning Electron Microscopy (SEM) and EBSD SEM was also used to provide more comprehensive and detailed identification of phases, especially microconstituents, with higher magnification. Samples used in optical microscopy analysis are coated before being used in SEM.

Electron Back Scattering Diffraction (EBSD) analysis was used to provide the information on crystallographic texture and grain boundary misorientation. The samples used for EBSD analysis were cut at a distance of one half from the sample surface, ground and polished as described in the previous section. Further electrolytic polishing is employed using an electrolytic solution of 85% acetic acid and 15% perchloric acid.

2.3.4 Main Results

2.3.4.1 Microstructure and Microconstituent Evolution There are five typical microconstituents found in the hot band microstructure. They are polygonal ferrite (F_P), non-polygonal ferrite (F_N), bainitic ferrite (F_B), pearlite (P) and carbon-rich microconstituents (C), as shown in Figure 2.20.

The final microstructure of each hot band is a combination of these five microconstituents and is dependent on the processing parameters. Even though there is no significant variation in the final grain size (as will be mentioned in the next section), the evolution of the microstructure is more sensitive to variation in finishing (T_F) and coiling (T_C) temperatures than to reheating (T_{RH}) and roughing (T_R) temperatures. As shown in the Figure 2.21, a microstructure evolution map has been constructed as a function of T_F and T_C. Polygonal ferrite and pearlite are the dominant phases at the upper left corner, which has a low T_F around 900°C and a high T_C around 700°C. When T_F is increased and/or T_C is decreased, non-polygonal ferrite (F_N) will be formed and its volume fraction keeps increasing with less polygonal ferrite (F_P) being detected. Further changing T_F and T_C in this way will lead to the formation of bainitic ferrite (F_B) along with a decrease in the volume fraction of pearlite. At the lower right corner of Figure 2.21, which has a high T_F around 1000°C and a low T_C around 550°C, no significant amount of pearlite is detected and other carbon-rich microconstituents are found.

Table 2.3 Real temperature used in hot rolling experiment

Combination of Conditions	Temperature, °C				Cooling Rate, °C /sec
	Reheat	Rough	Finish	End Cool	
1111	1200	1059	905	621	10.92
1112	1200	1051	908	693	9.32
1121	1200	1059	952	552	11.13
1122	1200	1116	958	677	10.12
1122	1200	1077	954	671	
1131	1200	1042	997	482	16.61
1132	1200	1061	1003	654	15.14
1211	1200	1148	913	607	10.54
1212	1200	1102	1048	-	9.19
1212	1200	1136	918	704	
1221	1200	1128	965	566	11.75
1222	1200	1106	954	677	9.58
1222	1200	1128	954	677	
1231	1200	1118	1009	510	13.48
1232	1200	1116	1006	654	13.51
1232	1200	1155	999	621	
2111	1280	1064	910	510	13.33
2112	1280	1064	906	677	8.19
2121	1280	-	-	-	
2122	1280	1055	952	677	9.84
2131	1280	1066	1004	399	13.16
2132	1280	1063	999	649	12.07
2211	1280	-	-	-	
2212	1280	1162	908	693	10.24
2221	1280	1162	956	552	11.88
2222	1280	1151	957	677	10.66
2231	1280	1159	1007	552	13.4
2232	1280	1164	1019	638	13.61

2.3.4.2 Grain Size Variation For those cases where the grain structure was sufficiently distinct, the grain size was measured and the results are given in Table 2.4.

The effect of processing on the grain size is shown in Figure 2.22. No significant pattern of dependence of the grain size on processing conditions can be gleaned from this figure; neither

the roughing temperature nor the finishing temperature appears to have a discernible effect. For a closer look at the effect of the finishing temperature, the mean grain diameter is plotted as a function of the measured finishing temperature shown in Figure 2.23. The effect of finishing temperature is negligible, being only an increase of 0.92 μm in mean grain diameter for an increase of 100°C in finishing temperature. In similar fashion, an increase of 100°C in the coiling temperature produced only a 0.69 μm increase in the mean grain diameter.

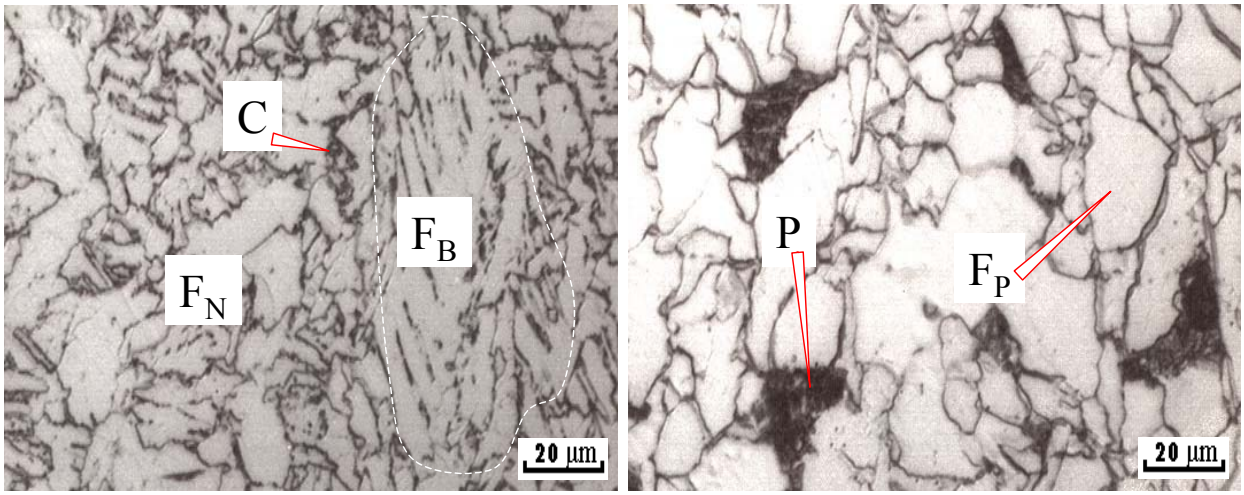

Figure 2.20 Typical microconstituents in the under-study HSLA steel hot band. P is the pearlite; F_P is the polygonal ferrite; F_N is the non-polygonal ferrite; F_B is the bainitic ferrite and C is the carbon-rich microconstituents.

Table 2.4 Grain Size Parameters for Polygonal Ferrite in the HSLA steel hot band
[C.V. = Coefficient of Variation, and < > denotes "mean".]

Process. Condition	Sample Size	Mean Diameter <D>, μm	Std. Dev of D, μm	C.V of D, pct
1111	288	4.52	1.77	39
1112	168	7.23	2.44	34
1122	191	7.95	3.24	41
1131	274	6.07	2.22	37
1132	308	9.11	3.69	41
11yz	5	6.98	1.76	
1211	214	4.24	1.33	31
1212	241	8.44	3.29	39
1221	302	5.90	2.19	37
1231	305	5.68	1.51	27
1232	243	5.90	1.83	31
12yz	5	6.39	1.66	
2111	345	5.47	1.77	32
2112	264	7.11	2.76	39
2122	290	6.54	2.93	45
2131	311	5.26	1.60	30
2132	256	8.43	3.06	36
21yz	5	6.58	1.16	
2212	274	6.54	2.90	44
2221	224	5.24	1.71	33
2222	287	6.99	3.12	45
2231	275	7.31	2.75	38
2232	283	6.77	2.21	33
22yz	5	6.59	0.64	

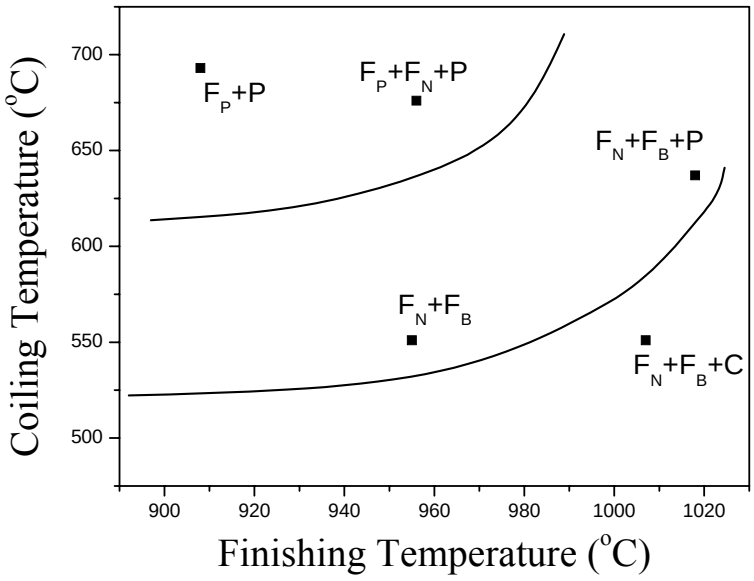

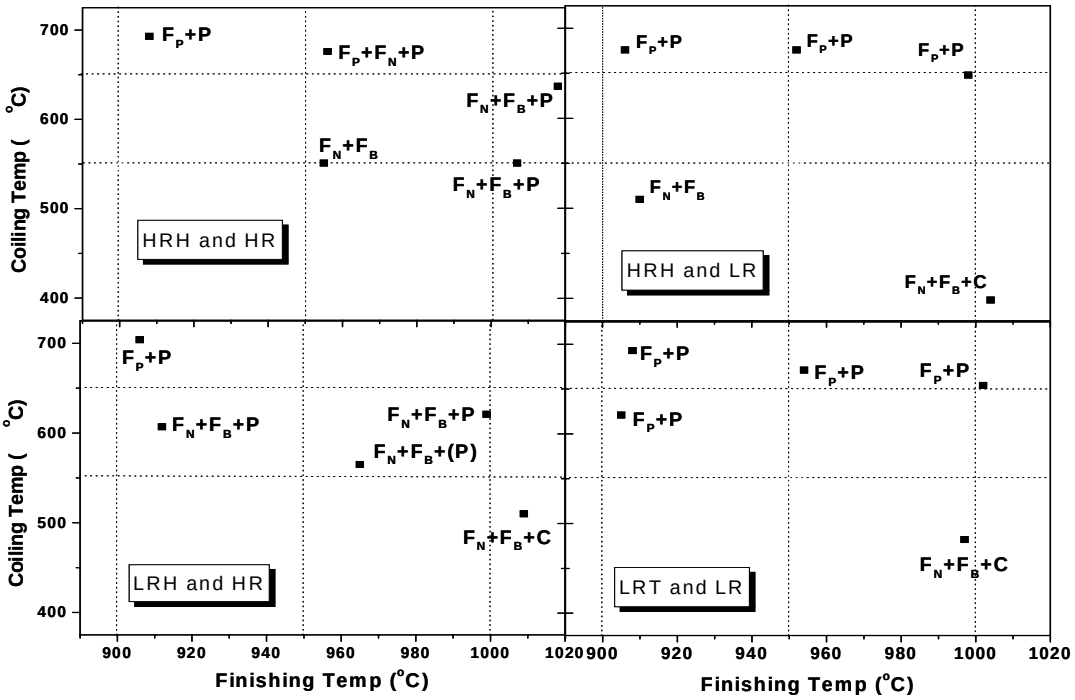

Figure 2.21 Microstructure evolution based on finishing and coiling temperatures, where HRH stands by High Reheating temperature, HR stands by High Roughing temperature, LRH is Low Reheating temperature and so on.

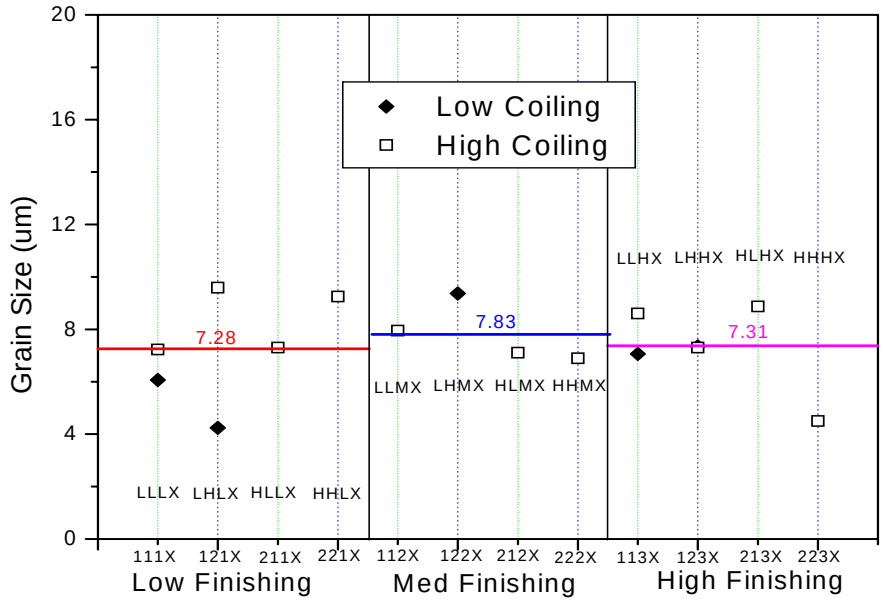

Figure 2.22 Variation of ferrite grain size with different processing factors

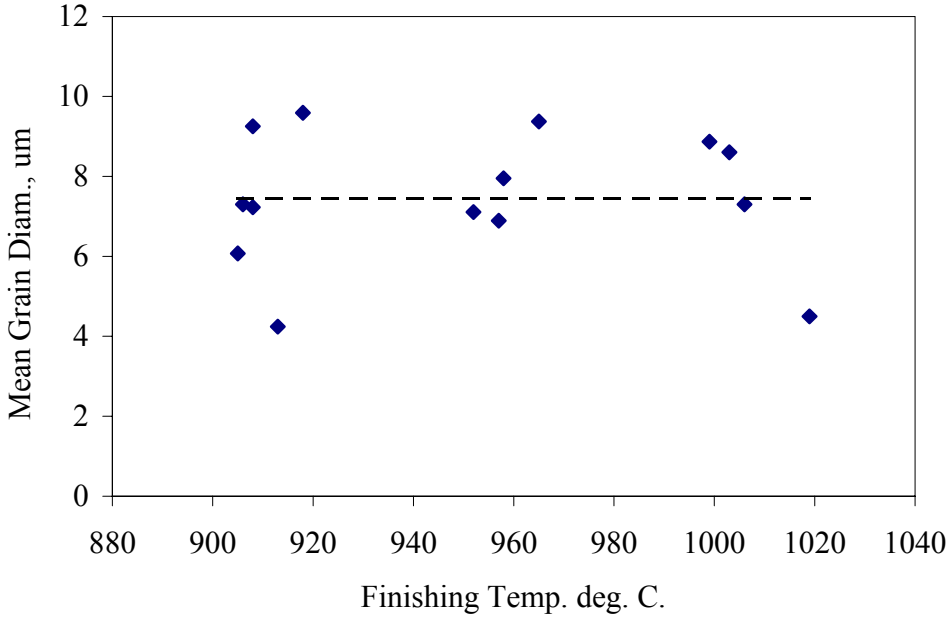

Figure 2.23 Illustration of the weak correlation of grain size with actual finishing temperature for the three aim levels of 900, 950, and 1000 ^{o} C.

2.3.4.3 Grain Boundary Character Distribution (GBCD)

2.3.4.3.1 Grain boundary misorientation

The grain boundary misorientation and the degree of preferred texture both have strong effects on the mechanical properties. The EBSD technique has been used to measure the grain boundary misorientation. Two examples of the measured distributions of grain boundary misorientations are given in Figure 2.24. Included in this figure is the theoretical distribution of grain boundary misorientations in a randomly oriented polycrystal.

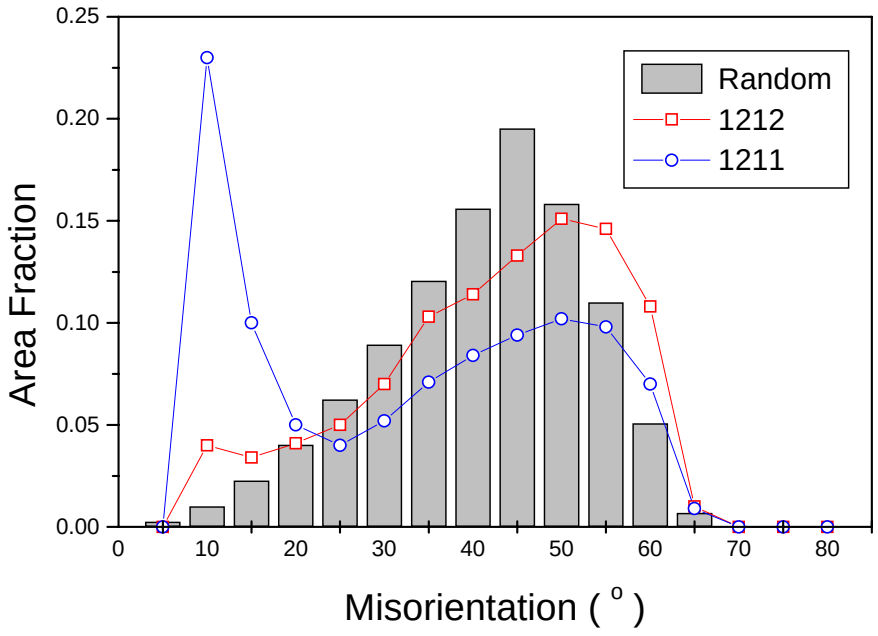

Figure 2.24 Representative frequency distributions of grain boundary misorientation as obtained by EBSD.

From comparison of the two distribution curves in Figure 2.24**,** it was found that for some processing conditions the measured distribution of the boundary misorientation may shift from

that resembling the random distribution. The fraction of the boundaries represented by "low-angle" character was estimated by finding the area under the “low-angle” peak. It was found that the lower coiling temperature leads to a much higher area fraction of the low angle grain boundary than does higher coiling temperature. Considering the microstructure evolution map of Figure 2.21, more low angle grain boundaries (LAGB) are found with increasing amounts of non-polygonal and bainitic ferrite. Both the variation in LAGB and the evolution of microstructure will cause the variation in the final mechanical properties.

2.3.4.3.2 Fractal Analysis

The yardstick method and the area-perimeter method are used to study the fractal characteristics of the grain boundaries.

The fractal dimension can be calculated using Equation 2.5 or Equation 5.1

$$N(\varepsilon) = a \cdot \varepsilon^{-D_S} \qquad \textbf{2.10}$$

where N is the number of steps used to tracing a certain length of grain boundary; a is a constant and ε is the yardstick length (or step length). If N versus ε is plotted on a log-log plot, the fractal dimension is given as

$$\ln(N) = \ln(a) - D_S \cdot \ln(\varepsilon) \qquad \textbf{2.11}$$

A combination of three measurements at three different step sizes and four magnifications was used to produce the plots presented in Figure 2.25.

When the area-perimeter method is used, Equation 2.7 and 2.8, the fractal analysis results on the 12xx microstructures are shown in Figure 2.26.

The effects of finishing and coiling temperatures on the nature of the grain structure of the hot rolled HSLA steel sheet are summarized in Table 2.5.

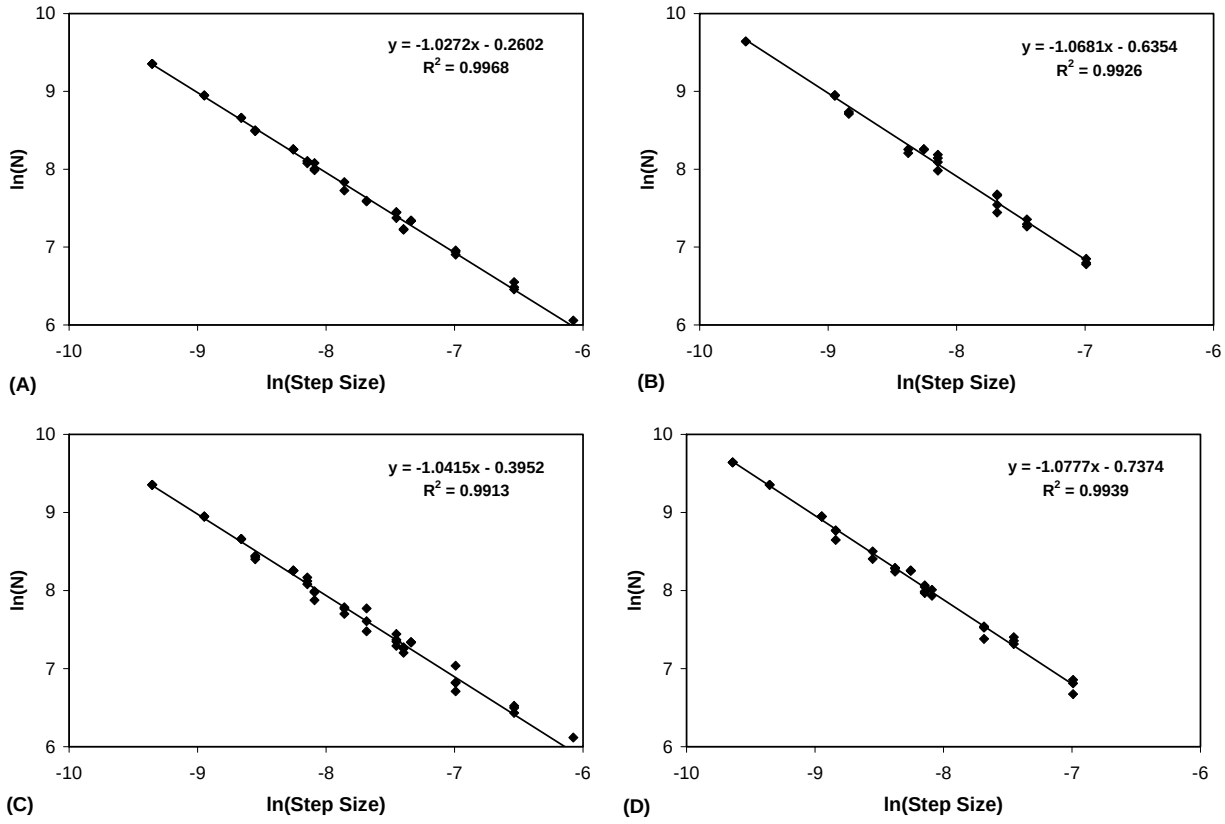

Figure 2.25 Fractal analysis of 12xx microstructures using the yardstick method. (A) 1212; (B) 1232; (C) 1211 and (D) 1231.

An interesting correlation between the fractal dimension variation and the microstructure evolution can be observed if the information in Table 2.5 and Figure 2.21 is combined as shown in Figure 2.27. With increasing the finishing temperature and decreasing the coiling temperature, more bainitic ferrite and acicular ferrite have been developed and the fractal dimension values

also are increased. Fractal analysis has successfully described the microstructure evolution with the processing condition changes. However, using this technique, no quantitative description of the fraction of each microconstituent can be gained.

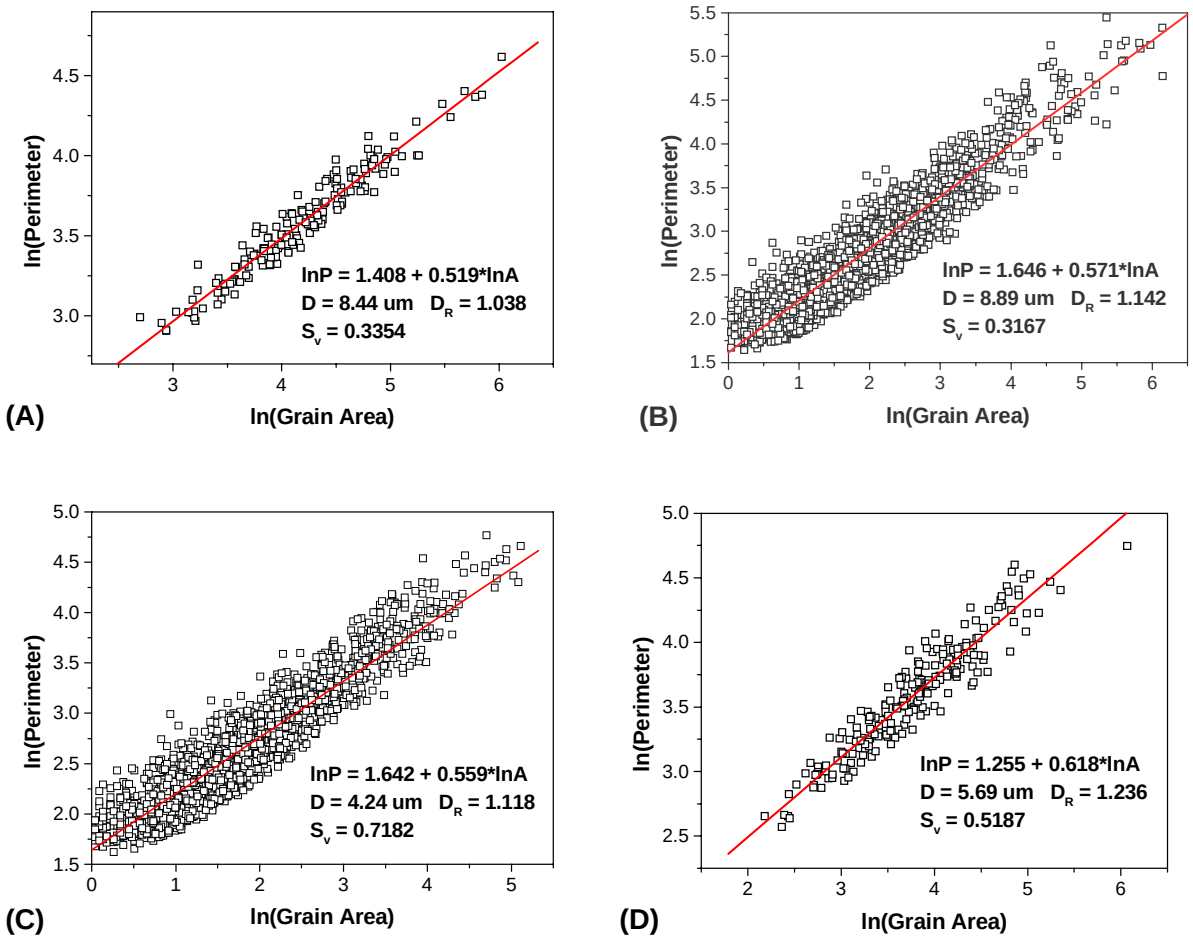

Figure 2.26 Fractal analysis of 12xx microstructures using the area-perimeter method. (A) 1212; (B) 1232; (C) 1211 and (D) 1231.

Table 2.5 Effects of the finishing and the coiling temperatures on the nature of the grain structure in hot rolled HSLA steel sheet.

	Low Finishing-Low Coiling (1211)	Low Finishing-High Coiling (1212)	High Finishing-Low Coiling (1231)	High Finishing-High Coiling (1232)
<D>, μm	4.24	8.44	5.69	8.89
S_v, /μm	0.7182	0.3354	0.5187	0.3167
G	4.27	3.88	2.76	4.23
D_R	1.118	1.038	1.236	1.142
D_S	1.041	1.027	1.078	1.068

In Table 2.5, <D> is the equivalent diameter of mean grain area; S_V is the amount of grain boundary surface per unit volume; G is the grain shape factor; D_S is the fractal dimension calculated by the yardstick method and D_R is the fractal dimension calculated from the area-perimeter relation.

The complexity of the HSLA hot band microstructures are significantly affected by the processing conditions. Even the grain size variation is in a very limited range, the measurement of the grain size is actually based on the ability of the operators to detect the grain boundaries. Therefore, the measurement of grain size is very much affected by the clearness and sharpness of grain boundaries shown in the optical micrographs. Only the grain boundaries of certain types of ferrite can be clearly observed and traced with a standard etchant. Because of this, the information gained from grain size measurement is certainly insufficient. The microstructure evolution is more closely related to the microconstituent population and grain boundary characteristics, both of which are very sensitive to the processing conditions.

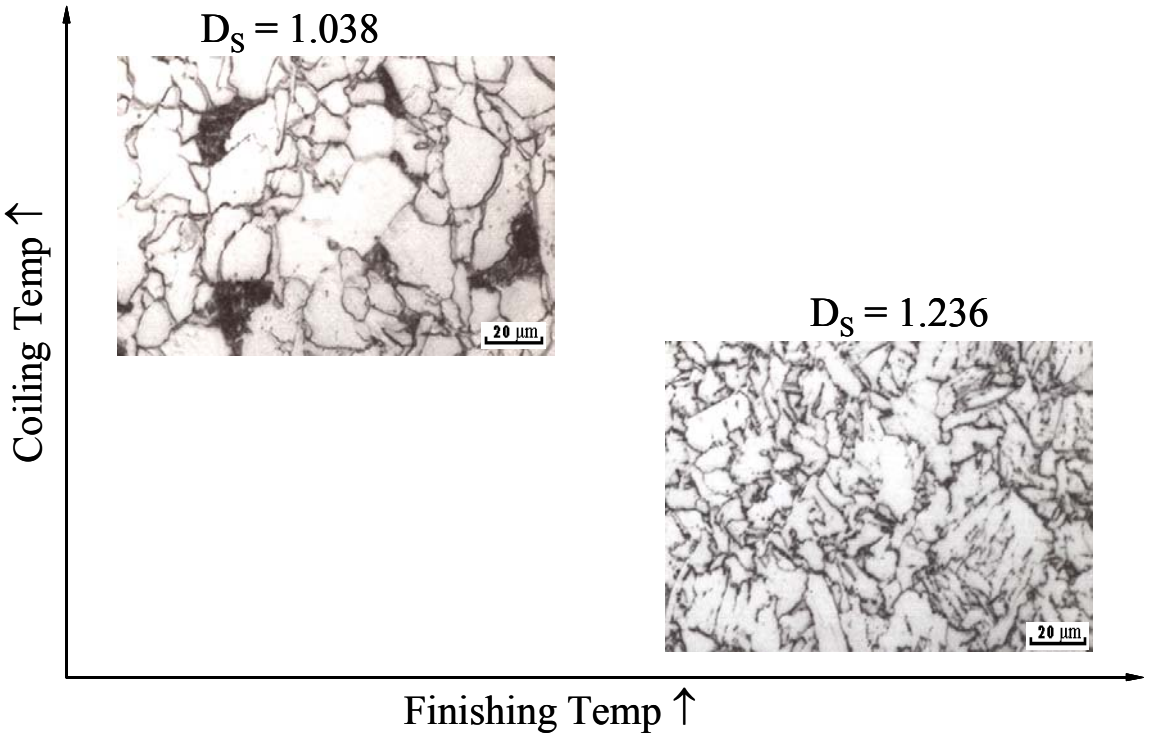

Figure 2.27 Correlation between the microstructure evolution and the fractal dimension variation under the effects of finishing and coiling temperatures.

The microconstituent variation with the processing temperatures, Figure 2.21, provides information on the microconstituent components under certain processing conditions. However, it has two important limitations. Firstly, the classification itself is based mainly on the morphology difference of various austenite decomposition products. Therefore, for a continuous cooling procedure, it is very difficult to identify some complicated microconstituents. The second limitation, which is actually caused by the first one, is that it is almost impossible to describe, quantitatively, these microstructures. In other words, for the microstructures with the same components but different volume fractions, they have the same description in Figure 2.21. Because of the second limitation, it is highly unlikely that the accuracy of the microstructure-mechanical properties relationship can be further improved because of the missing of the

required quantitative description of the microstructure. This highlights the importance and need of developing a new technique to identify and quantify various austenite decomposition products.

3.0 STATEMENT OF OBJECTIVES

The objective of this study is to develop a new technique(s) to quickly and accurately describe, identify and quantify different austenite decomposition products. During this study, the major challenges were:

To determine the various features, which should be measured and will provide valuable information on the microstructure description.

To develop some feasible techniques and/or theories to discern, identify, indicate and denote those features. Typical methods, like optical microscopy, SEM and EBSD, will certainly be used. The emphasis will be on developing new applications of those techniques for special interests.

To quantitatively analyze the microstructures based on the raw data obtained from the experiments. Mathematical treatment and physical metallurgy theories will be conducted subsequently to provide the volume fraction evaluation of each microconstituent in the microstructure.

To correlate the correctly measured microstructure features with the variations in mechanical properties.

To test and validate the newly developed microstructural analysis system using HSLA steels with complex microstructures.

4.0 EXPERIMENTAL PROCEDURES

4.1 MATERIALS STUDIED

Several different types of steels were used for the purpose of providing various microstructures. Those steels include IF steel, dual phase steel, and HSLA steel. All of these steels are commercially used and their compositions are shown in the Table 4.1.

Table 4.1 Composition of Steels under Study

Materials Code		Bulk Content, ppm.								
		Al	C	Mn	S	N	Nb	Ti	V	Ni
A	IF	410	20	1500	70	27	210	360	-	-
B	Dual Phase	10,900	1500	15500	60	30	30	-	-	-
C	HSLA	-	780	13,000	32	43	380	-	500	-
D	ASTM A572, Grade 50	340	800	14,200	30	-	30	30	1320	2100

4.2 MICROSTRUCTURAL DEVELOPMENT

To test and verify new techniques, various microstructures are needed for study. Those microstructures can be roughly grouped as simple, duplex and complex based on the number and types of microconstituents and their variations.

4.2.1 Simple Microstructures

Preliminary studies were focused on the microstructure of IF steel. There are two major advantages of using IF steel: clearly defined matrix microstructure and simple heat treatment. The first simple microstructure is the fully recrystallized polygonal ferrite. Polygonal ferrite with various grain sizes were developed for the purpose of studying the grain size effect on the accuracy and the feasibility of the new microstructural techniques. The thermomechanical procedure to obtain these different ferrite grain size is illustrated in Figure 4.1.

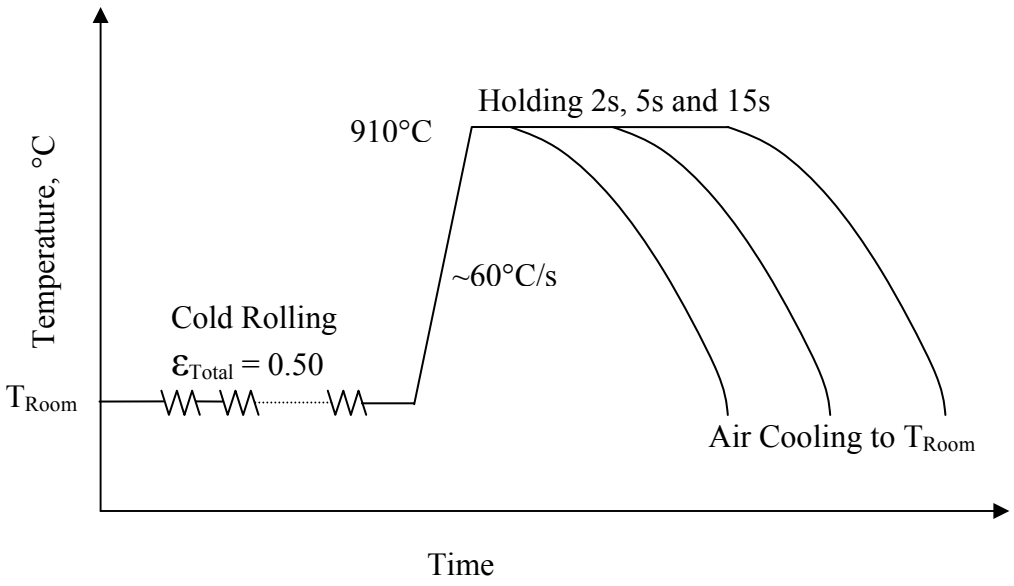

Figure 4.1 Illustration of the thermomechanical processing to develop polygonal ferrite microstructure with various grain sizes in IF steel.

Several passes of cold rolling with the total strain around 50% were applied to the commercial hot band of IF steel A before the heat treatments were conducted. The cold deformation introduced a very high S_V value, which implies a high density of nucleation sites

and high stored energy and therefore refined austenite and ferrite grain sizes are expected. By reheating the cold rolled specimens to just above the Ac_3, the austenite temperature and holding to different times, various ferrite grain sizes can be developed. As shown in Figure 4.1, three different holding times were selected, 2 seconds, 5 seconds and 15 seconds. The microstructure developed through each holding time is identified as A0, A1 and A2, respectively, with increasing grain size.

Continuing with the IF steel, another series of simple microstructures have been developed, as illustrated in Figure 4.2, for the purpose of studying the effect of dislocation density on the IQ distribution. The correlation between the ferrite formation and the dislocation density has been studied by many researchers [2, 9, 76-78]. Higher dislocation density is expected with lower transformation temperature and faster cooling rate. The difference in the crystal thermal expansion coefficients and the volume fraction change during the transformation are the two main source of the increasing dislocation density. With lower transformation temperature and faster cooling rate, more shear mechanism transformation and less self-annealing occurs, which also lead to higher dislocation densities. For the polygonal ferrite, the dislocation density varies from 10^9 to 10^{10} cm^{-2} [78]. The variation of the dislocation density increases with decreasing the transformation temperature.

In Figure 4.2, four different cooling methods, which indicate four different cooling rates, were employed to cool the specimens from the austenite temperature. Except for the grain size variation among these four conditions, the only difference is expected to be the dislocation density inside ferrite grains. The estimated cooling rates associated with each cooling method are given in Table 4.2 along with the microhardness measurement. With increasing the cooling rate, higher microhardness (higher dislocation density) has been observed as expected. One important

fact, which is somewhat out of the scope of this part of study, is that by water quenching the specimen from the austenite temperature, some other type of ferrite might be developed as well, which makes this so-called simple microstructure to be actually a duplex microstructure.

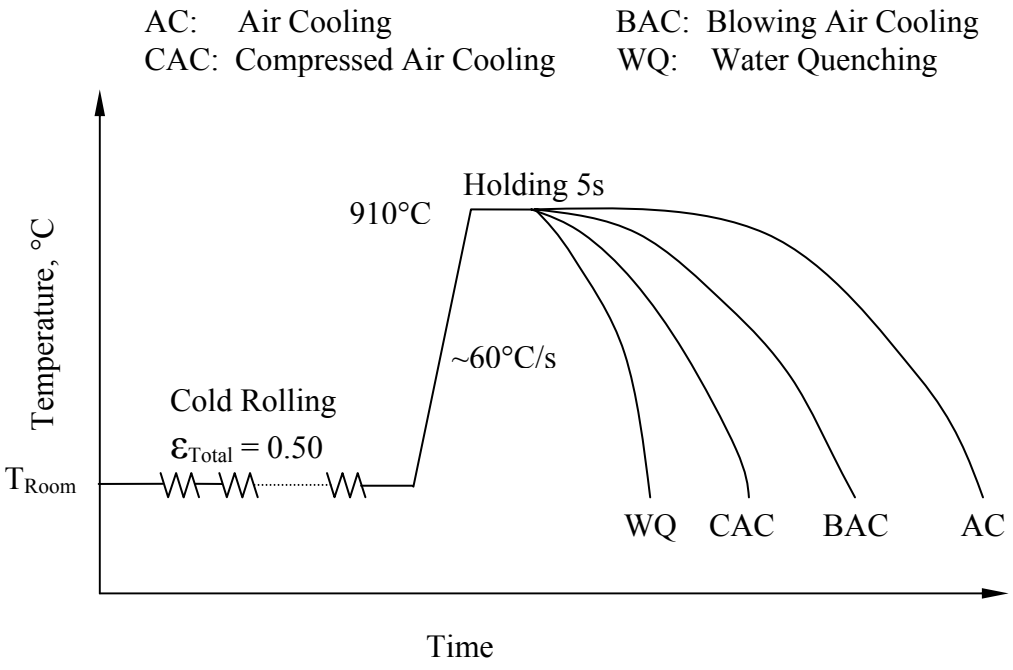

Figure 4.2 Illustration of the thermomechanical processing to develop ferrite microstructure with different dislocation density (IF steel).

Table 4.2 Estimated cooling rate and microhardness measurement of the continuous cooled IF steel specimens.

	Air Cooling, AC	Blowing Air Cooling, BAC	Compressed Air Cooling, CAC	Water Quenching, WQ
Cooling Rate, ^{o}C/s	~5	~20	~100	~1000
HV microhardness	64.4	66.9	72.1	100.8

The microstructures developed in this processing are identified as A1 (air cooling), A6 (blowing air cooling), A7 (compressed air cooling) and A8 (water quenching), respectively.

4.2.2 Cold Rolled Microstructures

The cold rolled microstructure is actually cold rolled polygonal ferrite microstructure developed from microstructure A2. The purpose of developing such a microstructure is to provide a condition between single phase and dual phase (or multi phase) microstructures, where only one phase (same lattice structure) exists, while with different lattice imperfections. With the initial A2 condition, three different amounts of cold deformation, 4 pct, 15 pct and 25 pct, were applied to develop microstructures A3, A4 and A5, respectively. A3 to A5 are basically polygonal ferrite as well, but having been deformed, they contain different dislocation densities.

4.2.3 Duplex Microstructures and Complex Microstructures

In this study, the duplex microstructure is defined as a microstructure containing two phases/microconstituents of significantly different features. In this case, these two phases/microconstituents were studied simultaneously. Duplex microstructures were used to testify the basic ability of the new techniques in distinguishing sharp difference in the characteristics. The results gained in the duplex microstructure analysis could be used as a reference when the complex microstructures are studied. Additionally, duplex microstructure analysis provides a simple condition for studying the interaction between different microconstituents during microstructural analysis. Therefore, it is a very important preliminary step to qualify these new techniques.

Two types of duplex microstructures were developed for similar purposes. One is the polygonal ferrite plus martensite microstructure developed from the dual phase steel, B, and the other one is the allotriomorphic ferrite (polygonal) plus acicular ferrite from the HSLA steel, C.

To develop the α'+ α microstructure, the cold rolled specimen is reheated to the two phase region, 810°C, held for 90 seconds and water quenched to the room temperature. The illustration of this treatment is shown in Figure 4.3. The microstructure developed through this procedure is identified as B0.

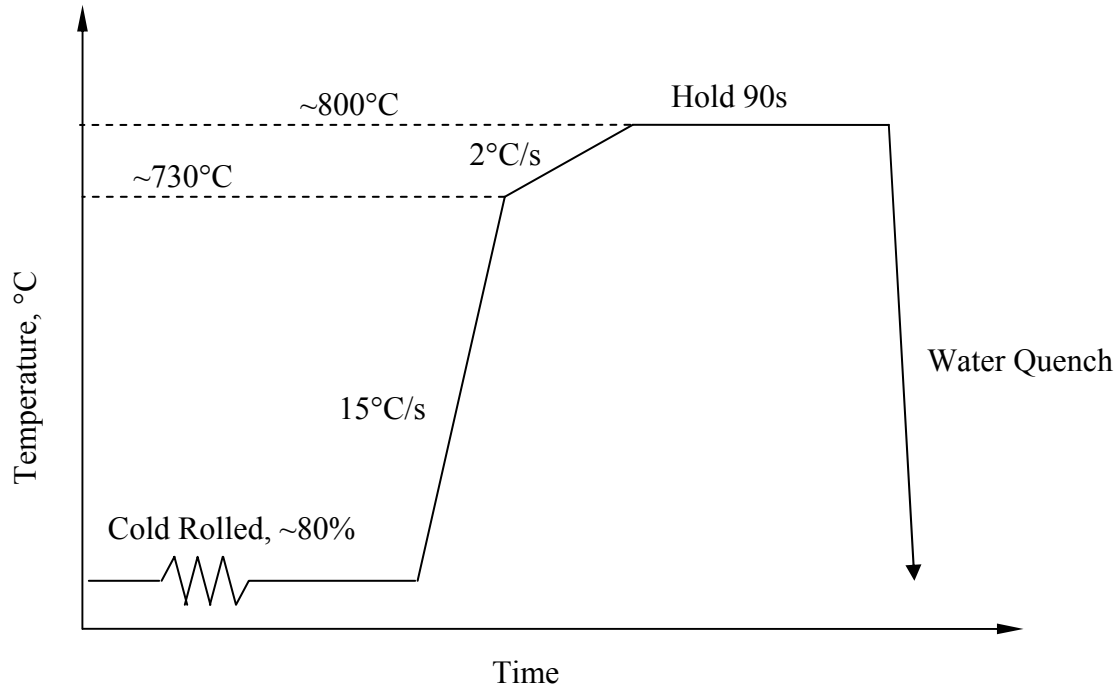

Figure 4.3 Illustration of the heat treatment procedure to obtain the α'+ α duplex microstructure.

The second type of duplex microstructure, polygonal plus acicular ferrite, is developed from a commercial as-cast microstructure of steel C. The heat treatment is illustrated in Figure 4.4.

The specimen is reheated to 1200°C and held for 30 minutes. A constant cooling rate of 1°C/s is used to continuously cool the specimen to the room temperature. The microstructure developed through this procedure is identified as C0.

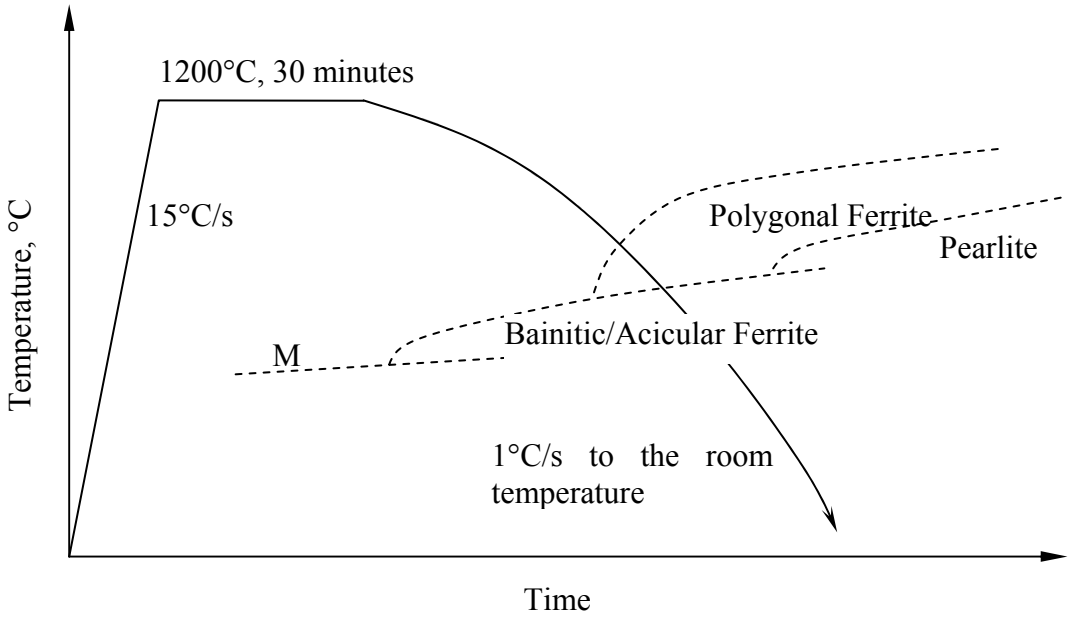

Figure 4.4 Illustration of the heat treatment procedure to obtain the polygonal ferrite and acicular ferrite duplex microstructure.

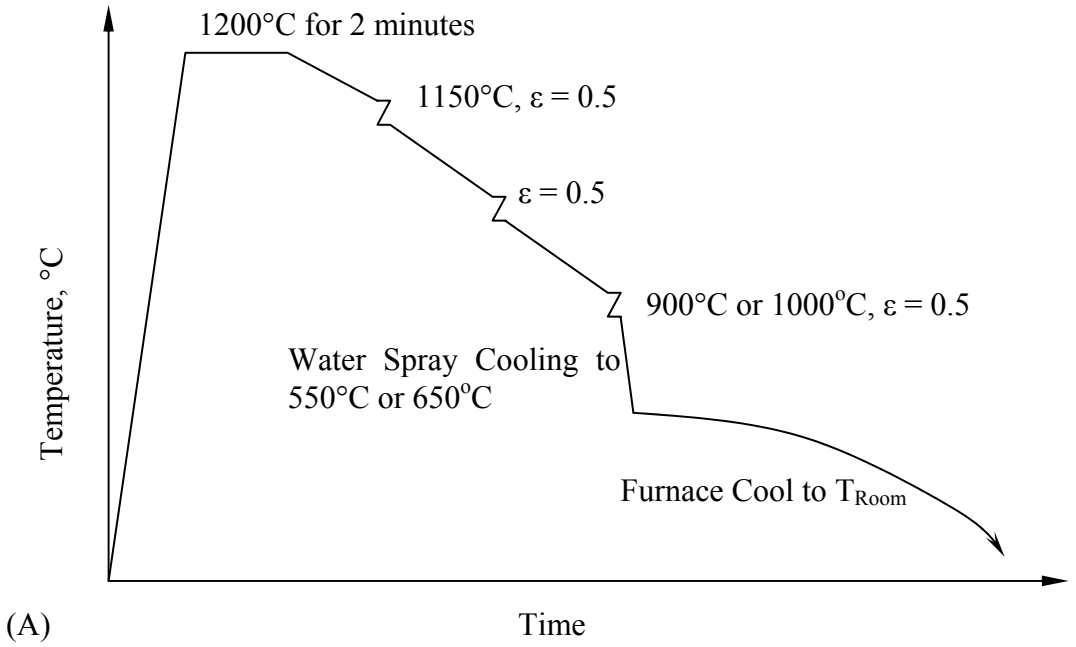

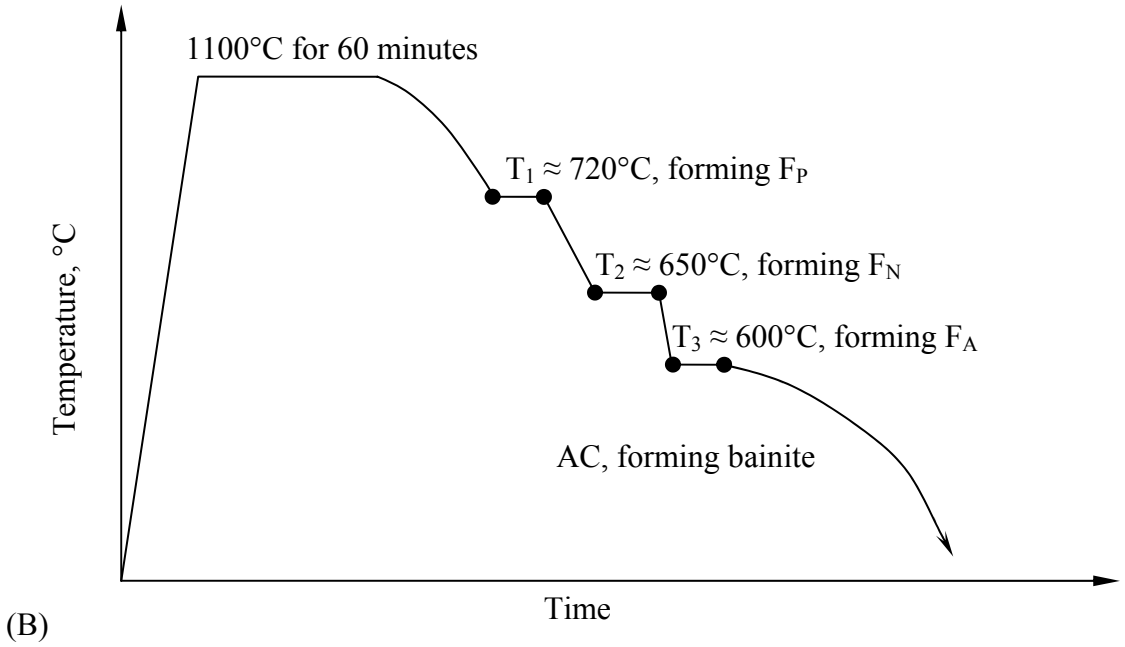

Figure 4.5 Illustration of the procedure to develop complex microstructure. (A) Simulating the hot rolling process using HSLA steel, steel C; (B) Developing various austenite decomposition products using ASTM A572 steel, steel D.

In this study, the complex microstructure is defined as the microstructure containing more than two different types of phases/microconstitutes. Several thermomechanical processing and heat treatments have been used to develop these microstructures. Those procedures are illustrated in Figure 4.5.

Steel C is used in the processing shown in Figure 4.5 (A), which is actually 12xx series hot rolled microstructures discussed earlier. The optical micrograph of 1231 microstructure is shown in Figure 4.6 as an example.

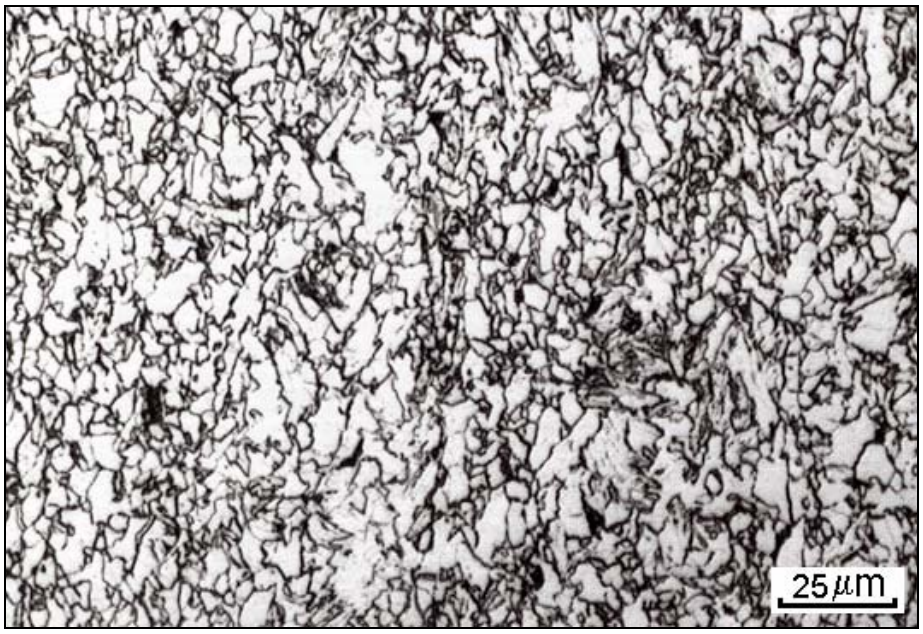

Figure 4.6 Optical microstructure of 1231 hot band developed by following the schedule shown in Figure 4.8 (A).

Another complex microstructure is developed using steel D. Based on the previous research on steel D from Al-Hajeri[79], the heat treatment schedule used is shown in Figure 4.5 (B). By holding the specimen at different intermediate temperatures and using different cooling rates, different austenite decomposition products could be developed at different temperature ranges.

According to Al-Hajeri's measurements, the austenite grain size before decomposition is around 100μm. With the holding temperature decreasing, polygonal ferrite, acicular ferrite, bainite and martensite will be formed in order at their preferred locations. A typical microstructure developed through this treatment is shown in Figure 4.7 and this microstructure is identified as D0.

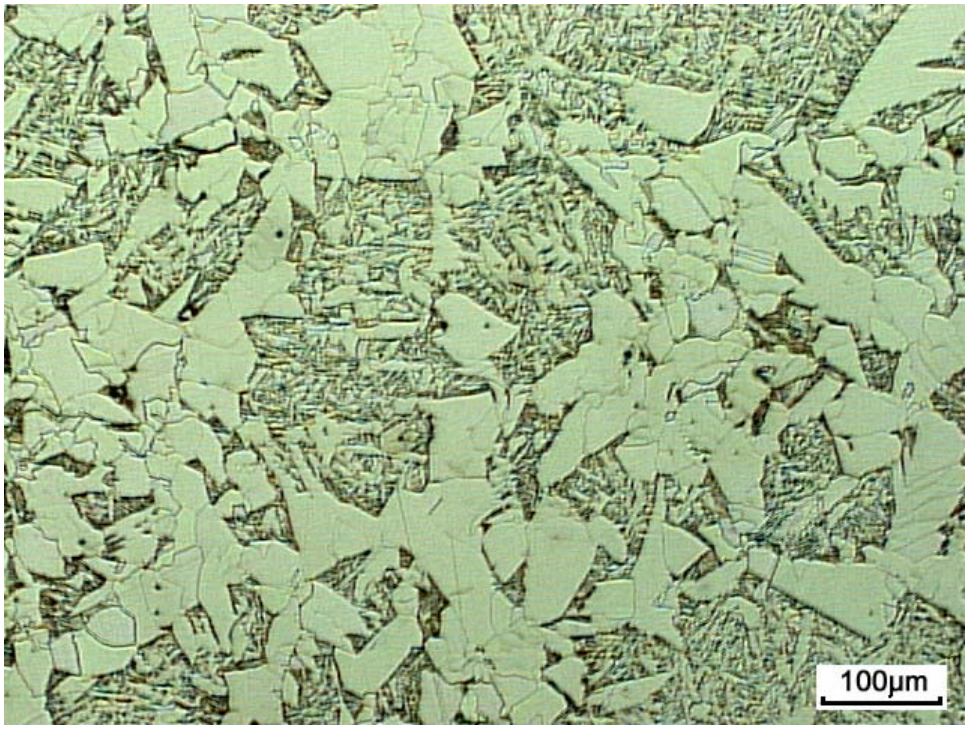

Figure 4.7 Optical microstructure developed by following the schedule shown in Figure 4.5 (B).

Table 4.3 is a summary of all the microstructures developed and to be studied with different microstructural techniques. The microstructural descriptions shown in Table 4.3 were determined through the observation of the optical micrographs of the specimens with 2% nital etched. Not

many details are included in the description, but it provides clear classifications of the microstructures for the purpose of testifying different techniques.

Table 4.3 Description of microstructures developed

Code	Material	Description
A0	IF	Small grain size polygonal ferrite
A1	IF	Medium grain size polygonal ferrite
A2	IF	Large grain size polygonal ferrite
A3	IF	4% cold deformed A2 microstructure
A4	IF	15% cold deformed A2 microstructure
A5	IF	25% cold deformed A2 microstructure
A6	IF	Polygonal ferrite with low level dislocation density
A7	IF	Polygonal ferrite with medium level dislocation density
A8	IF	Polygonal (non-polygonal) ferrite with high level dislocation density
B0	Dual Phase	Ferrite + Martensite microstructure
C0	HSLA	Allotriomorphic ferrite + acicular ferrite
12xx	HSLA	Simulated hot band with mixed austenite decomposition products
D0	ASTM A572	Mixture of different types of ferrite

4.3 QUANTITATIVE ANALYSIS OF MICROSTRUCTURES

Traditional methods have been used to determine the volume fraction of different austenite decomposition products. Those methods have been discussed in the previous sections. The measurement results are used to compare with those gained through using new techniques.

Two types of equipment were used to develop new quantitative analysis techniques, AFM and EBSD.

4.3.1 AFM

The idea of using AFM to quantify microstructures comes from two facts. The first fact is that AFM is a well-developed tool to observe the surface conditions (topography); and the other is that after certain polishing procedures, the topography condition of the surface should be related to the a microstructure as well as to the mechanical properties.

Before applying AFM, the specimens were polished through the standard procedure for optical microscopy usage as mentioned earlier. After that, there are three hours additional polishing applied using the **Vibromet 2** Vibratory Polisher. A typical image of the topography condition of the surface right after fully polishing is given in Figure 4.8.

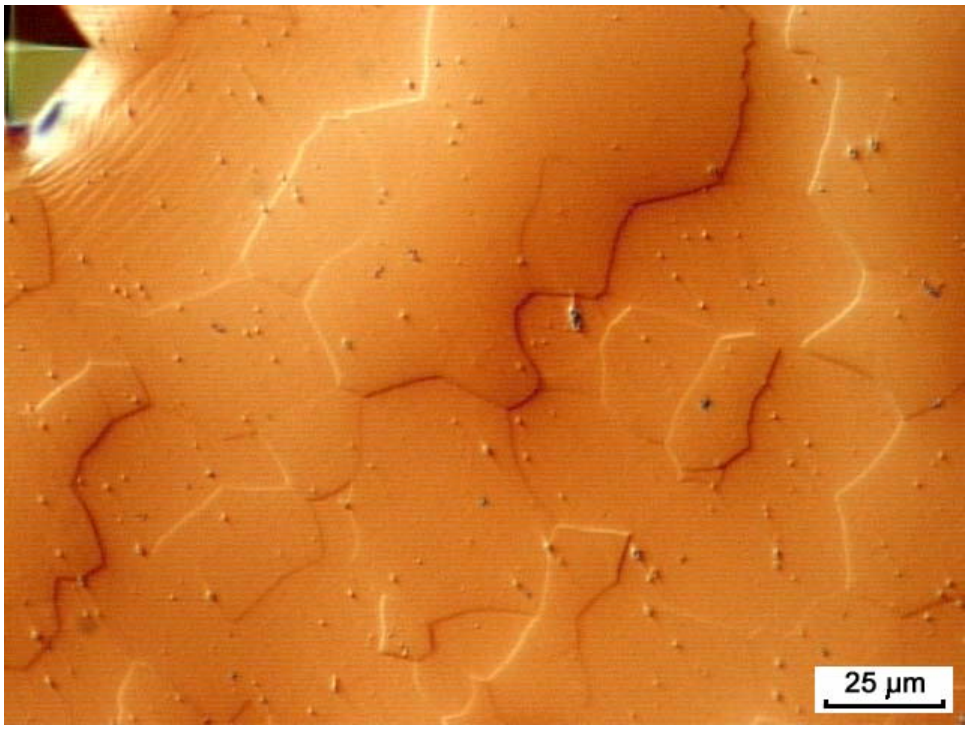

Figure 4.8 Topography of the IF steel specimen surface after fine polishing by using the Vibromet 2 Vibratory Pollisher.

Some selected areas with the maximum size of 100μm x 100μm, which is limited by the AFM equipment, have been selected for collecting the topography information. On those selected areas, EBSD analysis and classical optical microscopy have also been conducted.

For a fully developed AFM technique characterizing microstructures, there must be a pre-detected microconstituent as a reference point, which can be determined using the traditional techniques, such as OM or SEM. This reference point might be called topographic zero point and will be used to calculate the relative topographic positions of other areas. The microconstituents of the other areas could be determined by both their relative topographic positions and the reference microconstituent. However, all of these are based on the assumption that after fine polishing the surface topography condition is directly related to the microstructure present in the sample. Since there is no proof of this correspondence, it was decided not to go any further with this technique.

4.3.2 EBSD/Image Quality

The Vibromet 2 Vibratory Polisher is also used for fine polishing of the specimens for EBSD experiments. In this case, the total polishing time on the Vibromet 2 is 60 minutes. Standard operation procedure of EBSD observation is employed in this part of work. For every observation, 15kV voltage and the spot size of 4 are applied. The frame number is always set at 8 and the hexagonal scan mode is used with the step size varying from 0.5μm to 2μm determined by the grain size and the features of interest. All data collection is accomplished by using the OIM data collector software.

General analysis of the EBSD data is conducted by using the OIM Analysis software. Grain boundaries and subgrain boundaries can be determined and measured. Information on the texture

of the specimens can also be calculated. Initially recorded data of the diffraction pattern image quality (IQ) and the confidence index (CI) may also be normalized and presented by using this software. Except all of those functions provided by the basic package of the software, to satisfy special requests for quantification analysis, some computer programs have been developed for better understanding and more comprehensive description of the microstructures. These programs have been used to study the following several aspects:

The multi-modal distribution;

The grain boundary and IQ correlation;

The subgrain boundary distribution and hardness correlation.

The detailed statement of the purposes of those programs and their algorithms will be given in the Results and the Discussion section of this thesis.

4.4 MICRO/NANOHARDNESS MEASUREMENTS

Micro and nanohardness measurements are the key to correlate the quantified microstructure and the mechanical properties of the microstructure. In the case of large ferrite grain size (D_α>30μm), the microhardness of the ferrite grains can be measured by ignoring the effects from the grain boundaries. The microhardness information might help us to build up the correlation among subgrain boundaries, image quality and mechanical properties. The typical load used during the microhardness measurement in this study is 10 gram with the dwell time of 15 seconds. An example SEM image showing the large ferrite grains and the microhardness indentations is given in Figure 4.9.

While in most cases, the austenite decomposition products have a very small grain size and complex grain boundaries, microhardness measurement might not be used, being limited by its indentation size. In this case, the nanohardness measurement can be used instead. Through nanohardness measurement in a pre-selected area, every detail of the hardness information of the microstructure can be collected. This measurement covers not only the grain boundaries, but also the grain matrix among these grain boundaries; the nanohardness is affected not only by the grain boundaries, subgrain boundaries, but also by the defect density of the location of interest. The defect density variation is certainly associated with different types of austenite decomposition products. Therefore, such a detailed description of hardness variation can be used to connect microstructure, image quality and mechanical properties. An example image showing the nanohardness indentation is given in Figure 4.10.

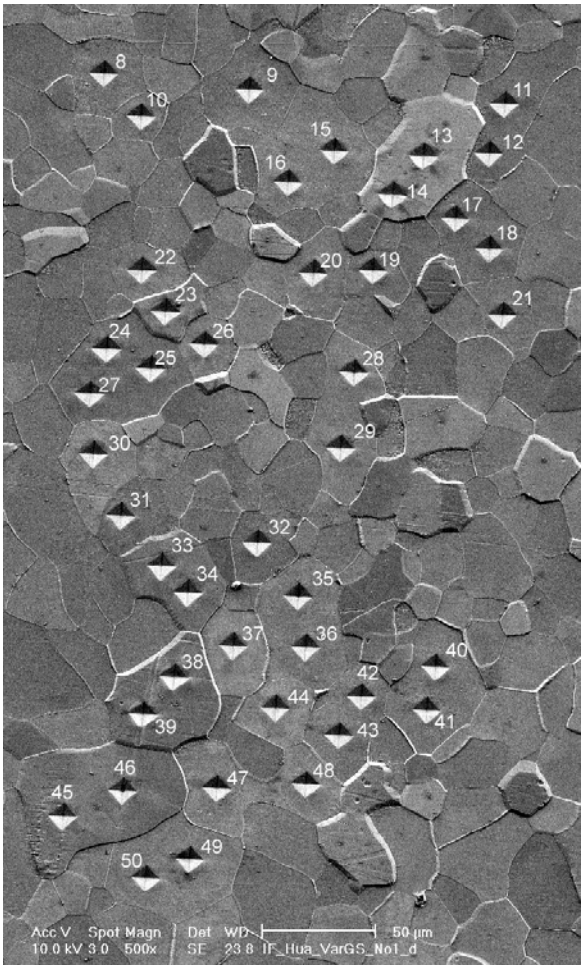

Figure 4.9 SEM image showing the large ferrite grains and the microhardness indentations.

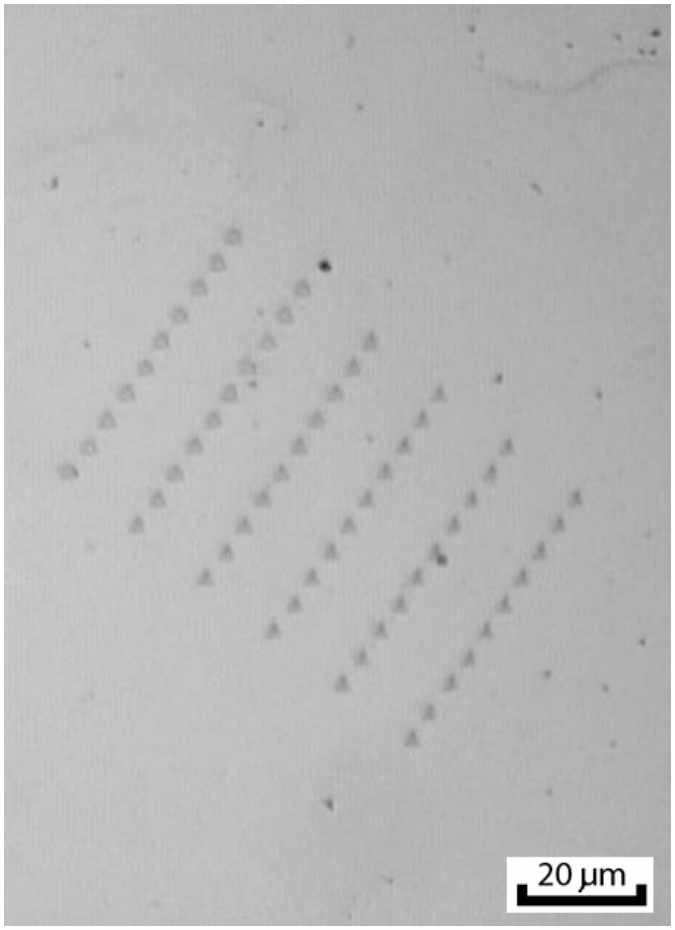

Figure 4.10 Nanohardness indentations on a fully polished sample surface.

5.0 RESULTS

5.1 TOPOGRAPHY ANALYSIS USING AFM

As shown in Figure 4.8, the specimen's surface is not ideally flat even after very carefully refined mechanical polishing. This surface topography implies at least two messages about the material properties: the crystal orientation and the hardness. The hardness as a characteristic of certain type of microstructure might be used in the identification and quantification of the microconstituent. However, the feasibility of using the hardness information for this purpose is complicated by the influence of orientation. If the topography variation caused by the orientation difference is less than or ignorable compared to the contribution of the hardness, the topography information might be modified for microstructure analysis. Otherwise, the situation is more complicated and cannot be interpreted without deeper understanding. To compare the contribution from the orientation and the hardness, a fully recrystallized polygonal ferrite microstructure and a dual phase (α'+α) microstructure have been studied by using AFM and EBSD, and images are showed in Figure 5.1 and Figure 5.2 respectively.

In Figure 5.1, the circled area has been studied. Since this 40μm x 40μm area is composed of the same types of high temperature polygonal ferrite, given unique crystal orientation, an ideally flat surface is expected. However, as shown in Figure 5.2 (C), a distinguishable change of height of approximately 100nm has been observed between two neighboring grains. This height change is caused only by the different crystal orientation.

Similar observations of a dual phase microstructure have also been conducted and the images are shown in Figure 5.2. Because of the crystal orientation difference, the ferrite grains are having different height values as expected. This can be observed by comparison of these two areas located in the red and green rectangular areas. In the center of each rectangular, there is a ferrite grain. Both of these ferrite grains have a distinguished height difference from their surroundings. However, in the red rectangle, the ferrite area is higher and in the green rectangle, the ferrite area is lower. Considering the area connecting these two ferrite grains, which has been found to be martensite, it is found surprisingly that the hard microconstituent (e.g. martensite) might not appear to be higher than those soft microconstituents (e.g. ferrite) after this polishing procedure. Hence, the crystal orientation plays a very important role in the surface topography development. Without correction of the orientation contribution, topography analysis using AFM cannot independently be used as a tool to identify and quantify microstructures.

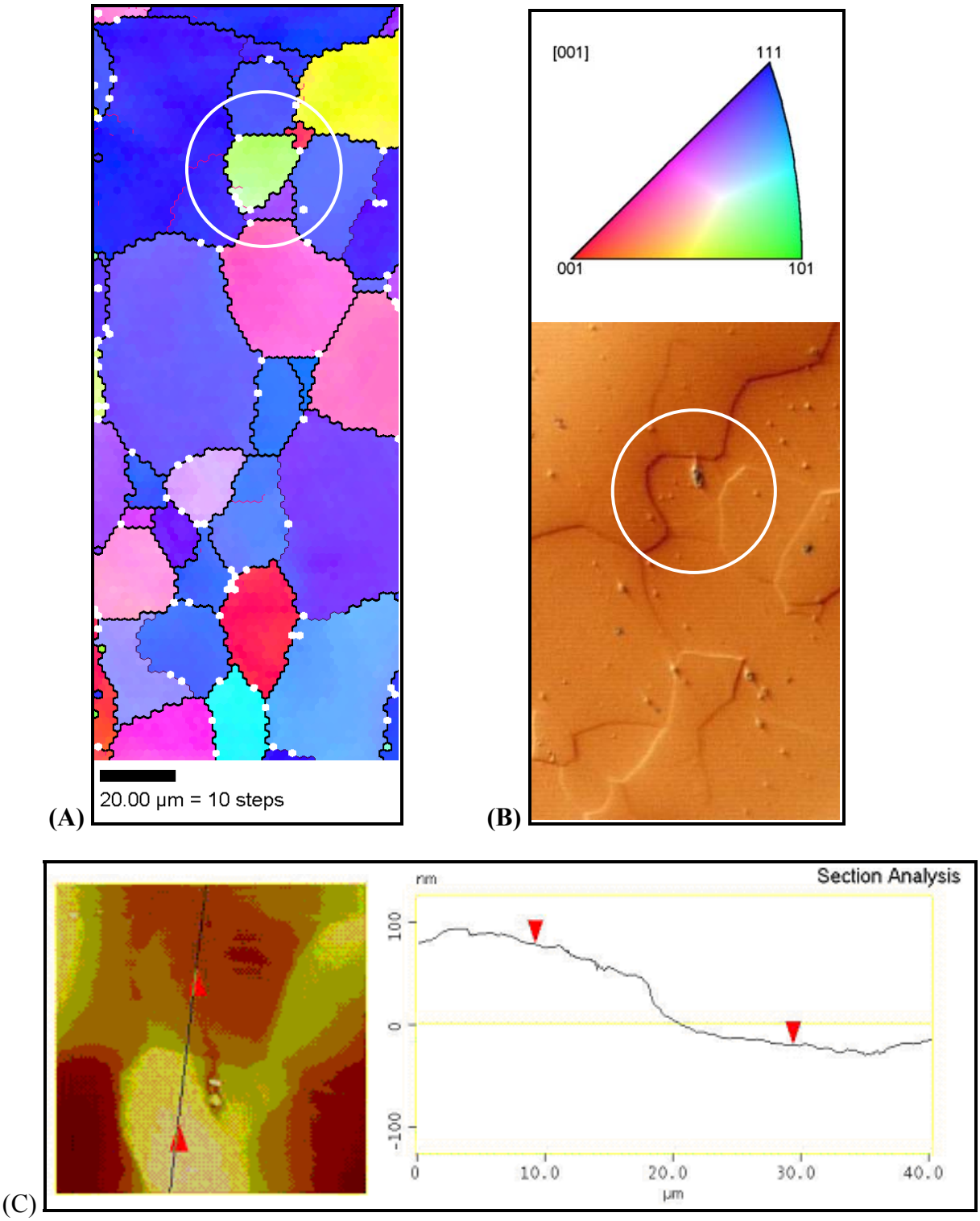

Figure 5.1 Topography analysis of the fully recrystallized ferrite microstructure of IF steel. The area in the white circle is of interest. (A) Inverse pole figure map; (B) Nomarski interference contrast image; (C) AFM image with section analysis.

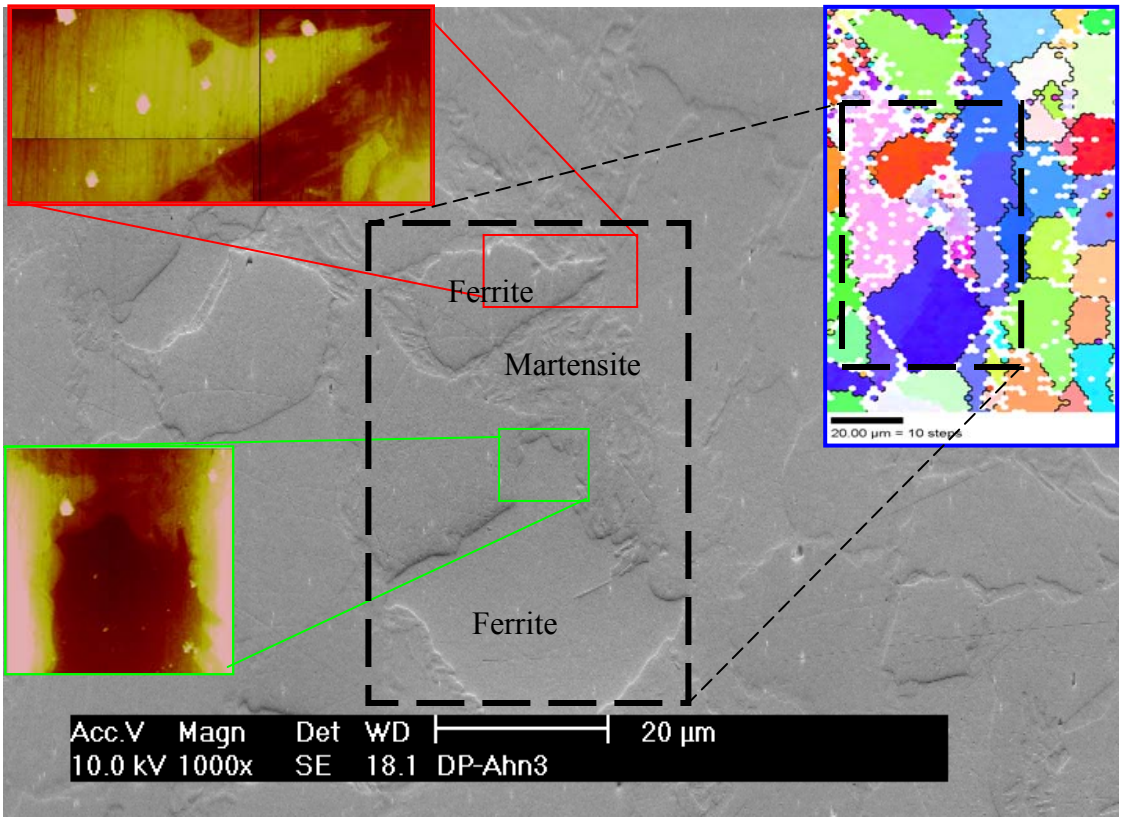

Figure 5.2 Topography analysis of the α+α' microstructure of dual phase steel. In the background SEM image, the left two insides are AFM images showing the topography information in the two sealed areas (in red and green). The area in the black dashed rectangle has been studied by EBSD and the inverse pole figure of this area is shown as the right inside.

5.2 IMAGE QUALITY (IQ) ANALYSIS USING EBSD

For all results in this part of study, the initial IQ data were collected by using the OIM data collector software and with the same EBSD experimental conditions. For every scanning, 15kV voltage and the spot size of 4, are applied. The frame number is set at 8 and the hexagonal scan mode is used with the step size varying from 0.5µm to 3.0µm determined by the grain size and the microstructure.

5.2.1 Normalization of IQ values

The most important factor impeding the application of image quality in phase identification is that the IQ value is very sensitive to many experimental factors, including the image processing conditions. These factors may blur/confuse the information from the microstructure itself and significantly reduce the comparability of IQ values. Normalization of IQ values is the way to minimize these misleading effects.

Assuming that such experimental factors have equal effect on each microconstituent in the microstructure, it is the absolute image quality values, not the relative image quality values from microconstituent to microconstituent, that is really influenced by the experimental conditions. The normalized IQ value can be calculated as.

$$IQ_{Normalized} = \frac{IQ_{Initial}}{IQ_{S\tan dard}} \times 100 \qquad \textbf{5.1}$$

where $IQ_{Initial}$ is the absolute IQ value gained directly from experiment; and $IQ_{S\tan dard}$ is the average IQ value of a standard sample, which is presumed to have a perfect crystal structure and to give the highest IQ value under the same EBSD processing conditions.

Equation (1) can be used to normalize various kinds of microstructures with extremely different microconstituent components, because they are normalized according to an independent $IQ_{S\tan dard}$. For comparing microstructures with the same components but different volume fractions, a simplified equation, equation (2), can be used. The expression of equation (2) does not need the information of the standard specimen and saves time in scanning.

$$IQ_{Normalized} = \frac{IQ_{Initial} - IQ_{Min}}{IQ_{Max} - IQ_{Min}} \times 100 \qquad \textbf{5.2}$$

where IQ_{Max} and IQ_{Min} are, respectively, the maximum and the minimum IQ values in the scanning set.

5.2.2 Bi-modal and multi-modal distribution

Typically, the histogram of the IQ distribution is bell- or Gaussian- shaped [66], which is also confirmed in our results and will be shown later. If we further assume a normal distribution, then the group mean and standard deviation must be considered for any histogram of the IQ distribution of a single microconstituent and a symmetric shape of the histogram is always expected. Whenever an asymmetric shaped histogram is observed, it implies that more than one microconstituent of different mean IQ values exists. The multi-peak model is developed on this assumption and used to divide the whole histogram into several normal distributions, each of which represents a certain microconstituent.

The multi-peak model can be described as:

$$N = \sum_{i=1}^{k} n_i \qquad \textbf{5.3}$$

$$IQ \cong \sum_{i=1}^{k} ND(n_i, \mu_i, \sigma_i) \qquad \textbf{5.4}$$

$$Min(k) \qquad \textbf{5.5}$$

$$\left| IQ - \sum_{i=1}^{k} ND(n_i, \mu_i, \sigma_i) \right| \leq \varepsilon \qquad \textbf{5.6}$$

where N is the number of the total scan points in the file; k is number of normal distributions in the simulation; ε is the minimum acceptable error; $ND(n_i, \mu_i, \sigma_i)$ is the ith normal distribution with the total data number of n_i, the group mean value of μ_i and the standard deviation of σ_i.

Determination of the value of k is an extremely important step, because the more normal distributions involved, the better fit can be achieved, but, which might not be reasonable for the real microstructures. A nice fitting can be always achieved through a mathematical way, but might not be correct from a metallurgical view. Therefore, k must be determined both mathematically and metallurgically. Basic physical metallurgy analysis and optical microstructure observation are suggested during determining the k value.

Adjusting every normal distribution and satisfying the Equations 5.3 to 5.6 would reach a minimized error between the initial IQ distribution and the sum of all single normal distributions as shown in Equation 5.6. Each of these normal distributions represents one microconstituent component in the microstructure.

The bi-modal distribution is a simple case of multi-modal when only two microconstituents exist.

5.2.3 Concerns on grain boundaries

A grain boundary is the interface of two bulk materials with different crystal orientations and/or different crystallographic structures. In either case, because both sides of the grain boundary have contribution to the diffraction pattern, a significantly reduced IQ value is expected at the

grain boundary location. Depending on the purpose of the analysis, the low IQ area in the vicinity of grain boundaries might be treated differently in the data processing.

When the IQ values are used to quantify microconstituents, the low IQ region from grain boundaries would be a source of misleading information. And, the scan points from the vicinity of grain boundaries should be carefully taken care of or just simply filtered. While the image quality values are related to the mechanical properties, grain boundaries, as a significant source of strengthening, should certainly be included in the analysis. The point here is, whatever treatment is to be done with the grain boundary, those scan points in the grain boundary region must be identified and marked.

In this work, the grain boundary is defined by the misorientation of the two neighboring scanning points. In the TSL software, the statistical information on grain boundary misorientation can be calculated; however, there is no clue to identify and study the properties of any special grain boundaries of interest. In other words, it is impossible to filter out those pixels from the grain boundary region (GBR). To mark out the GBR scan points, a program was developed. In this program, the misorientation between every two neighboring scan points is calculated based on its definition as described by Randle [80]. The grain boundary is defined as any interface with the misorientation larger than 15°. The GBR covers the scan points that are contiguous with the grain boundaries, which is illustrated in Figure 5.3. After calculating through all scan points, the GBR points can be marked for further analysis.

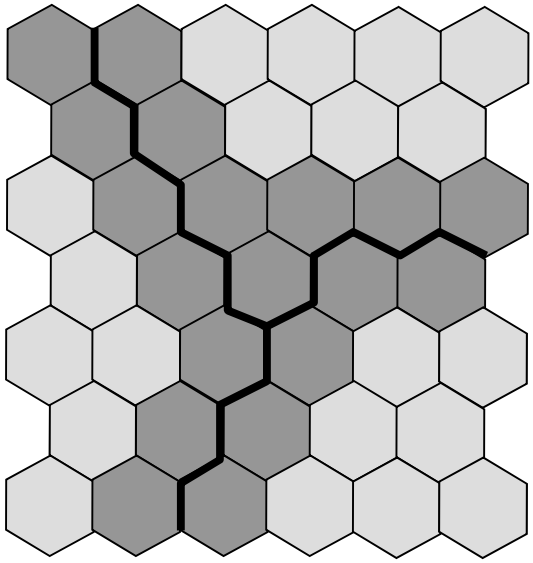

Figure 5.3 Schematic of the Grain Boundary Region (GBR). Each cell represents a scan point; the heavy black line is the grain boundary and the cells in dark gray are GBR points.

5.2.4 Effects of the employed scanning step size on IQ analysis results

The scanning step size can certainly affect the accuracy when EBSD is used to measure the grain size. This topic has been reviewed earlier. In this part of the study, the effects of the employed scanning step size on IQ analysis results will be discussed.

Microstructure A8 is studied using EBSD with different scanning step size from 0.6 μm to 3.0 μm. The optical micrograph of A8 is given in Figure 5.4 and the grain size is approximately 10 μm.

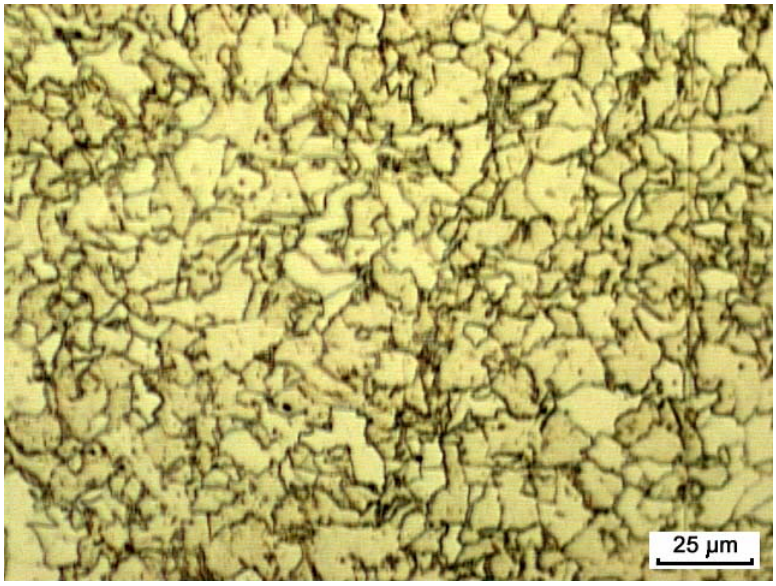

Figure 5.4 Optical micrograph of Microstructure A8.

The normalized IQ distribution curves using different scanning steps are shown in Figure 5.5. All experimental data including the GBR are presented in Figure 5.5; therefore, the Multi-Peak model is not applied in this part of the study to quantify each microconstituent. Only the profiles of IQ distribution curves are of interest here. It is found that the step size has strong effects on the profiles of the distribution curves. Increasing the step size leads to higher fraction of the low IQ peak. This increase in the low IQ peak is so large that significant error could be introduced if an appropriate step size is not employed.

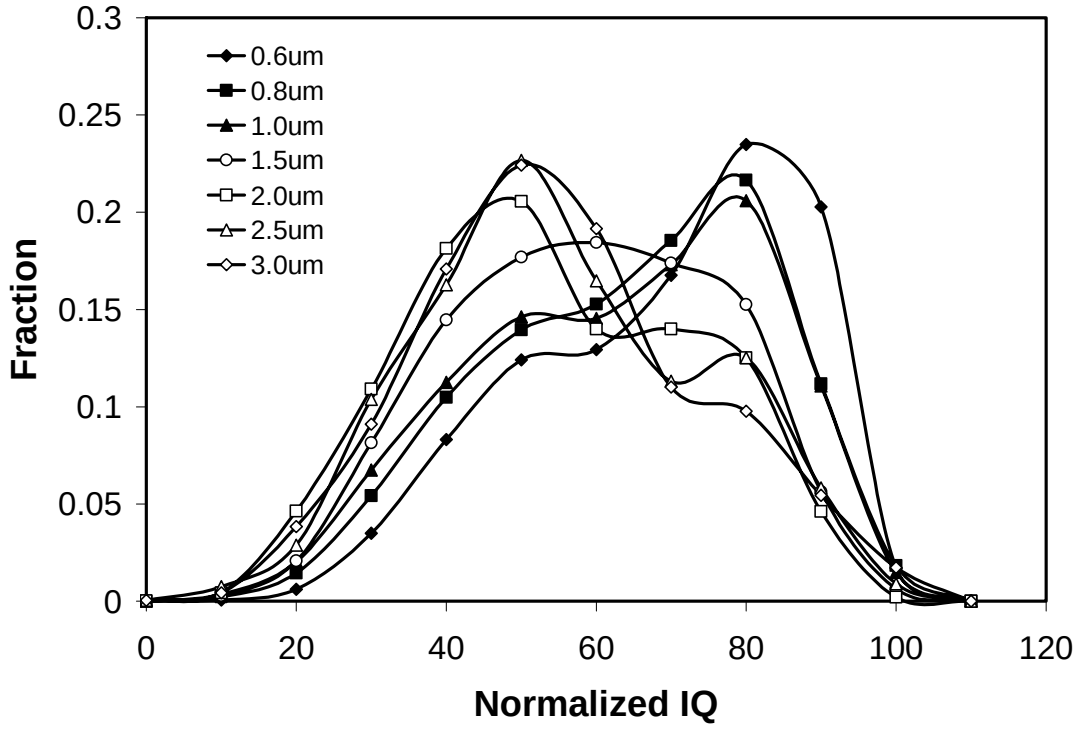

Figure 5.5 The IQ distribution curves of A8 microstructure analyzed using different scanning step sizes.

The low IQ peak comes from the areas of relatively high defect densities. These areas could be one-dimensional features, e.g., grain boundaries, or two-dimensional features, e.g., acicular ferrite grains. Considering a total scanning area, A, as shown in Figure 5.6, the number of the scan points in this area can calculated as:

$$N \approx (L \times W)/S^2 = A/S^2 \qquad \textbf{5.7}$$

The number of the scan points along grain boundaries can be determined by

$$N_{GB} \approx 2 \cdot L_{GB} / S \qquad \textbf{5.8}$$

And the number of the scan points in the low IQ microconstituent area and its perimeter is determined by

$$N_{LIQ} \approx \frac{A_{LIQ}}{S^2} + \frac{2\sqrt{\pi \cdot A_{LIQ}}}{S} \qquad \textbf{5.9}$$

where the first part comes from the area and the second one comes from its perimeter. Therefore, the fraction of the low IQ peak can be evaluated as

$$F_{LIQ} = (N_{GB} + N_{LIQ}) / N = a \cdot S + b \qquad \textbf{5.10}$$

where *a* and *b* are constant for a certain microstructure, and they are determined by

$$a = 2 \cdot (L_{GB} + \sqrt{\pi \cdot A_{LIQ}}) / A \qquad \textbf{5.11}$$

$$b = A_{LIQ} / A \qquad \textbf{5.12}$$

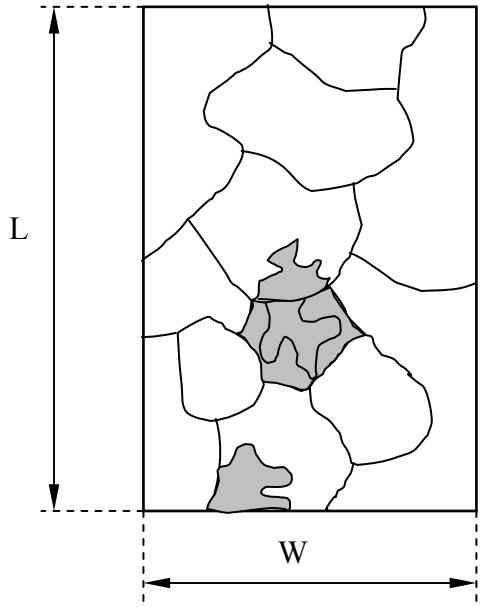

Scan Area: $A = L \times W$;
Total GB length: L_{GB}
Total Low IQ Area (in gray): A_{LIQ}
Step Size Employed: S
Number of Total Scan Points: N

$$N \approx (L \times W)/S^2 = A/S^2$$

Number of Scan Points on GB: N_{GB}

$$N_{GB} \approx 2 \cdot L_{GB}/S$$

Number of Scan Points in LIQ Area: N_{LIQ}

$$N_{LIQ} \approx \frac{A_{LIQ}}{S^2} + \frac{2\sqrt{\pi \cdot A_{LIQ}}}{S}$$

Fraction of LIQ Peak: F_{LIQ}

$$F_{LIQ} = (N_{GB} + N_{LIQ})/N = a \cdot S + b$$

Figure 5.6 Illustration of the correlation of the scan step size and the IQ distribution profile.

From Equation 5.10, it is found that the low IQ peak fraction is linearly related to the scanning step size. This equation might be used to explain what is observed in Figure 5.5. However, the over simplified equations should not be used to evaluate the optimal step size during scanning.

As observed in Figure 5.5, evident variation of the distribution profile occurs at the step size of 1.0 μm, which is approximately one tenth of the estimated grain size of the microstructure. Considering the grain boundaries are included in Figure 5.5 and they might significantly affect the low IQ peak based on Equations 5.10 and 5.11, it is reasonable to conclude that a step size smaller than one tenth of the grain size should be used in the IQ analysis.

5.2.5 Fully recrystallized polygonal ferrite (simple phase) analysis

The gray scale IQ maps of two fully recrystallized polygonal ferrite microstructures with different grain size are shown in Figure 5.7. It is not surprising to find that the darker areas, which indicate lower image quality, are especially located in the vicinities of grain boundaries. When the GBR is included, as shown in Figure 5.8 (a), for both microstructures, there are two distinguishable peaks in the IQ histogram. Since there is only one simple microconstituent in both microstructures, the lower IQ peak could only correspond to the GBR points. With a smaller grain size, there is a higher area fraction of grain boundary per unit volume than that with larger grain size. This higher fraction of grain boundaries implies a larger low IQ peak, which is observed in the IQ histogram of smaller grain size, as expected. After filtering out the GBR points with the algorithm mentioned earlier, two symmetric IQ histograms for both microstructures are achieved, as shown in Figure 5.8 (b). This confirms that the lower IQ GBR points are the only source of the second peak observed in low IQ range and for a single microconstituent microstructure, its IQ distribution is symmetric.

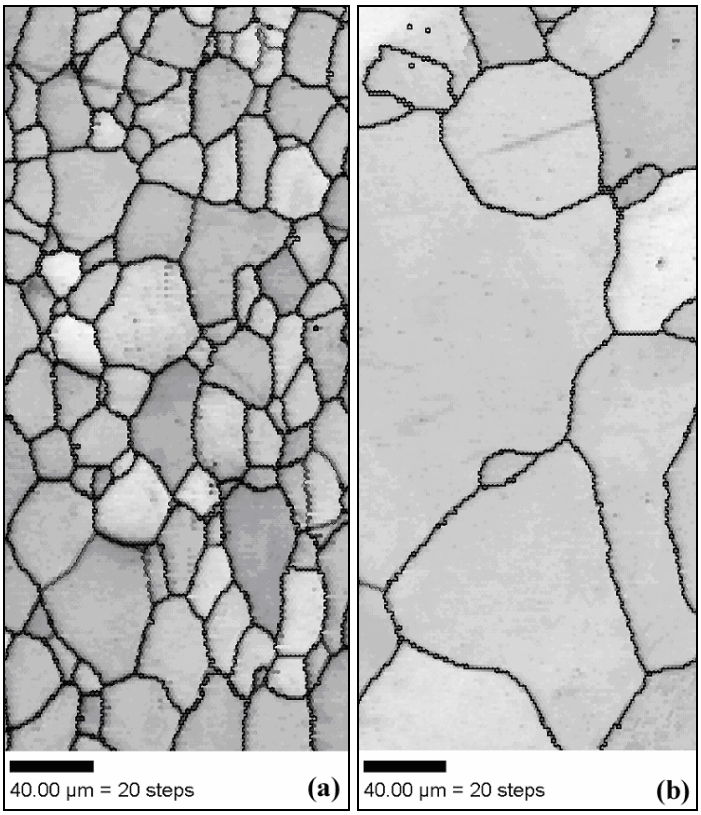

Figure 5.7 Gray scale IQ maps of (a) A0 and (b) A1 microstructures.

The GBR could also affect the mean IQ value of each peak in the histogram. As seen in equation 5.2, IQ_{Min} and IQ_{Max} are normalized to be 0 and 100, respectively. For a certain absolute IQ distribution, IQ_{Min} and IQ_{Max} values would affect the mean IQ value of the peaks after normalization. In A0 and A1 microstructures, the IQ_{Min} value most likely comes from the low IQ GRB peak. For unknown reasons, the IQ values of the GBR usually have a large variation. This makes the normalized IQ distribution less predicable. Under the effects of the GBR, the peak positions of the two distributions, as shown in Figure 5.8 (a), are not well matched. While in Figure 5.8 (b), with GBR filtered, the mean IQ values are approximately the same.

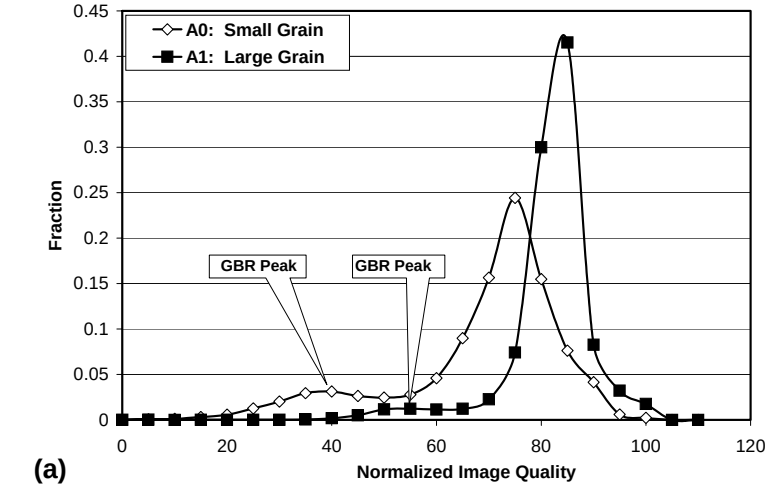

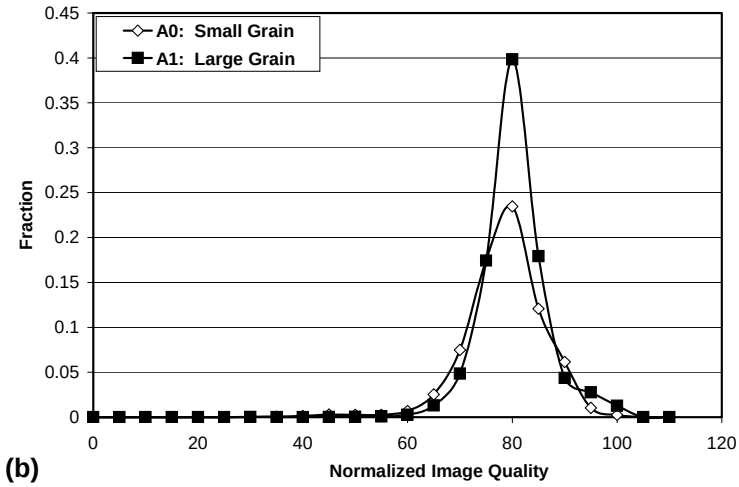

Figure 5.8 The IQ distribution profile of A0 and A1 microstructures. (a) Normalized IQ data including those of GBR; (b) Normalized IQ data without the GBR contribution.

5.2.6 Image quality and the defect density

There are two main purposes of this part of study. One is to confirm that the image quality is directly related to the lattice imperfection (subgrains, dislocations); the other one is, based on the

symmetric distribution of the single phase and multi-peak model, to evaluate the correlation between the lattice imperfection and the IQ distribution curve. Two series of microstructures were used in this part of study: cold rolled specimens and continuously cooled specimens.

5.2.6.1 Cold Rolled Condition The image quality maps of microstructures A4 and A5 strained 15 and 25 pct. respectively, are shown in Figure 5.9. The areas in gray have the normalized IQ values lower than 60, and the areas in white are those with higher normalized IQ values. From a comparison of the IQ maps of Figure 5.9 with the misorientation maps of the same regions shown in Figure 5.10, it is evident that the low IQ areas are directly associated with low angle grain boundaries. Developed from the same initial microstructure, the difference of the low angle misorientation distribution in these two microstructures could only come from the different amounts of cold deformation applied. The apparent correlation between the high dislocation densities introduced by cold deformation and the low image quality is clearly detected. Based on this, the distribution of the retained strain can be examined. As shown in Figure 5.9, the strain distribution indicated by the low image quality areas is inhomogeneous. When the strain is relatively small, Figure 5.9 (a), there are very few low angle misorientation boundaries found inside the grains. This means the applied strain could be accommodated by the grain boundary sliding or by reverse shear inside grains. With increasing strain, as in Figure 5.9 (b), the low IQ area extended into some grain centers. The selection of grains where strain is retained, which is directly related to the yielding behavior of steels, might be determined by the orientation of the grains. However, this important topic is outside the major scope of this work and will not be discussed further here.

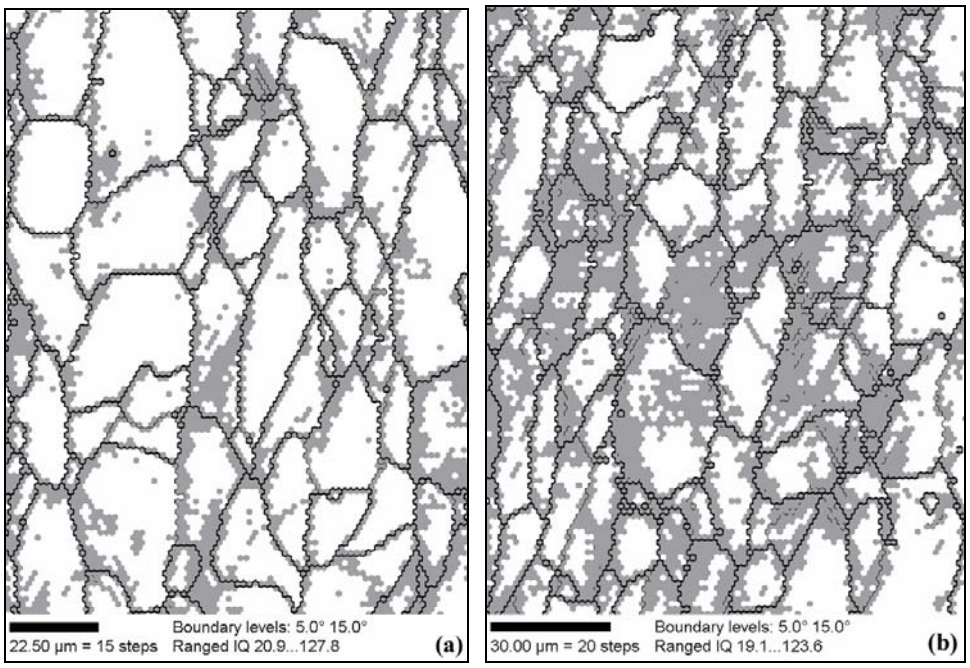

Figure 5.9 IQ maps of (a) A4 microstructure and (b) A5 microstructure. Areas in gray have normalized IQ value lower than 60 and the areas in white have relatively higher IQ values.

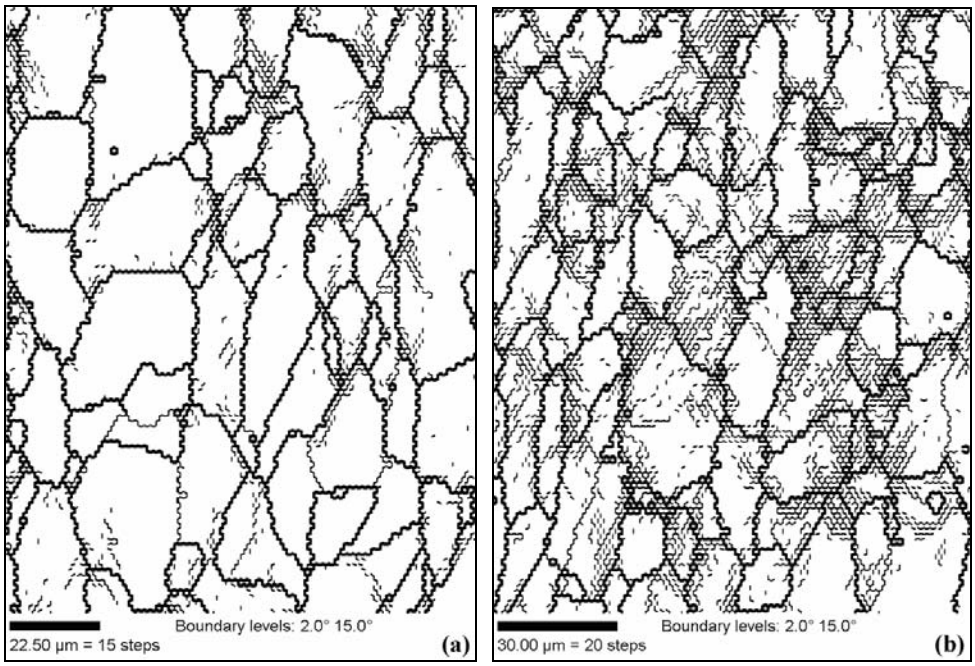

Figure 5.10 EBSD misorientation maps of (a) A4 microstructure, and (b) A5 microstructure. The black thick lines are grain boundaries with misorientations larger than 15°; and the gray thin lines are those misorientation from 2° to 15°.

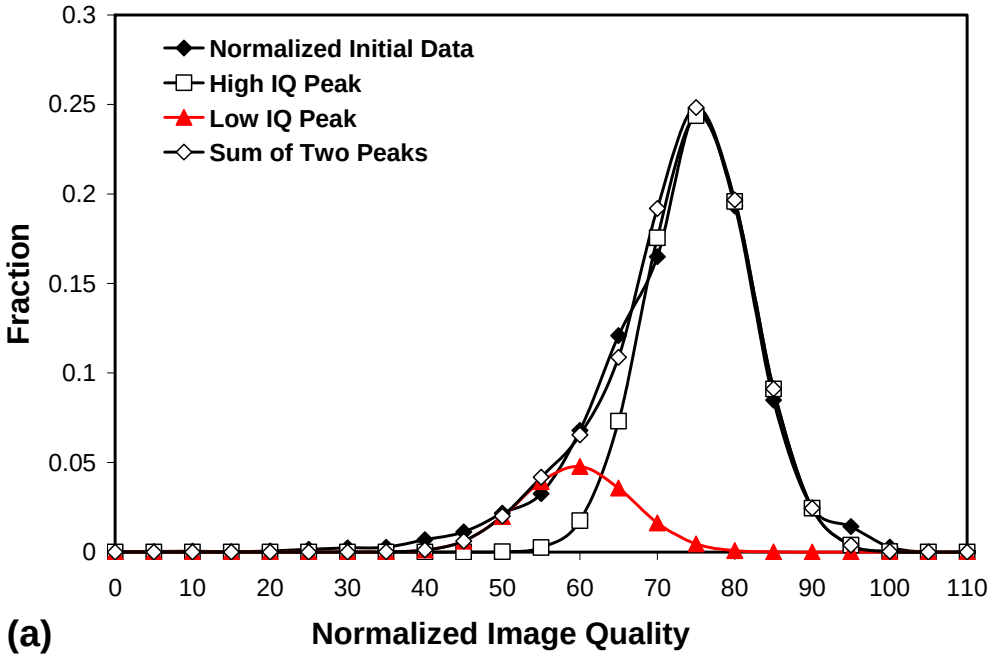

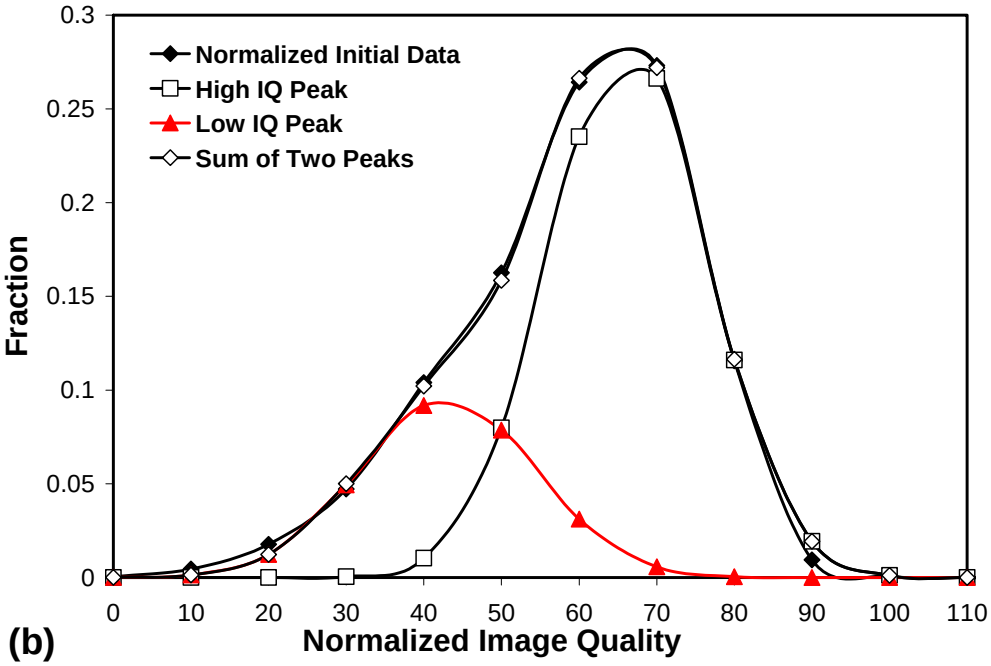

Figure 5.11 The IQ distribution analysis of (a): A4 microstructure and (b): A5 microstructures using the Multi-Peak model.

Table 5.1 The Multi-Peak analysis results of the cold rolled A1 microstructure

Microstructure Code	Low IQ Peak	High IQ Peak	Cold Strain
A4	0.17	0.83	0.15
A5	0.27	0.73	0.25

The multi-peak model has been used to analyze the cold deformed A4 and A5 microstructure, and the results are shown in Figure 5.11. The initial EBSD data have been normalized and the grain boundaries have been filtered. For both microstructures, the histogram of IQ distribution could be best fitted with two normal distribution curves. The low IQ peak corresponds to the areas with retained strain; while the high IQ peak represents those areas that are affected very little by the deformation. The fraction of the data points of each peak is given in Table 5.1. It is surprisingly found that the fraction of the low IQ peak numerically matches very well with the strain applied. This appears to support the idea that the IQ analysis and the multi-peak model can be used to identify the strain-retained area and quantify the amount of cold deformation. Further work is in progress to decide whether this good agreement is real or fortuitous.

5.2.6.2 Continuously Cooled Condition IF steel specimens that are cooled from austenite with different cooling rates have different dislocation densities in the ferrite grains. This difference in dislocation density is the most important feature of the ferrite except the grain size difference and the grain morphology variation, which only exist when the cooling rate is extremely fast. The dislocation density variation cannot be easily detected and quantified using

conventional techniques. In this part of the work, IQ analysis is applied to study this topic to "see" dislocation densities in a new way.

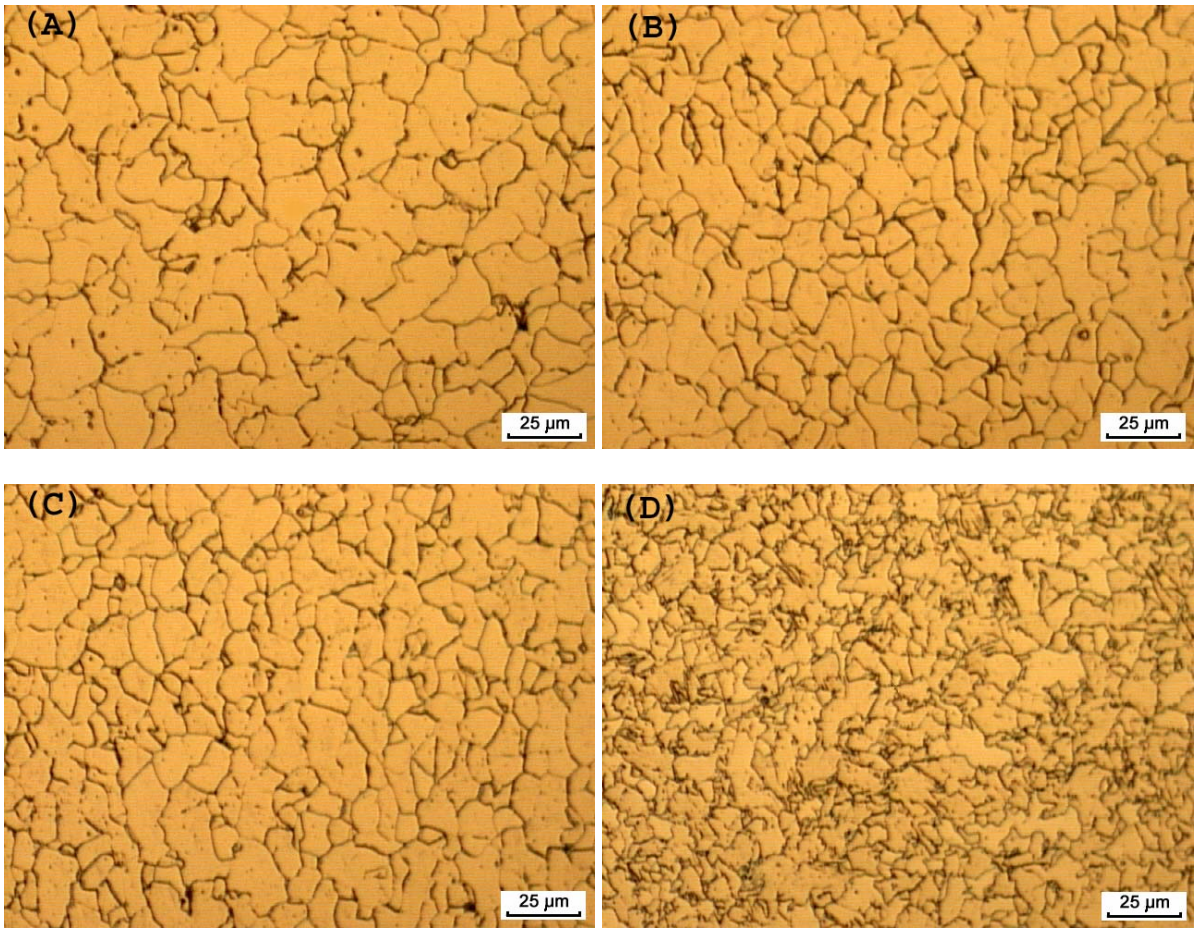

Figure 5.12 The optical micrographs of the IF specimens continuously cooled from 910°C to room temperature. (A) Microstructure A1, air cooled; (B) Microstructure A6, blowing air cooled; (C) Microstructure A7, compressed air cooled; and (D) Microstructure A8, water quenched.

The optical micrographs of the microstructures under study are given in Figure 5.12. Based only on those images shown in Figure 5.12, there is no obvious change in the grain morphology

through (A) to (C), where different air cooling methods (air cooling, blow air cooling and compressed air cooling) are used. All of them can be roughly described as polygonal ferrite microstructure, which is actually what they were designed to be. However, there are also several individual grains exist in all these conditions that have relatively irregular grain perimeters. Those grains could be defined as non-polygonal ferrite; the identification of which is hard to be made grain by grain and the amount of which is therefore difficult to be measured. As another fact in Figure 5.12 (A) to (C), the decrease in the ferrite grain size is detectable, while it is very slight from (B) to (C). Figure 5.12 (D) is evidently different from the others. It is actually a complex microstructure with several types of ferrite developed under much faster cooling rates, water quenching. Figure 5.12 (D) is expected to have significantly different IQ analysis results from those of the first three conditions.

The IQ distribution curves of the continuously cooled IF specimens are shown in Figure 5.13. Figure 5.13 (A) shows all experimental data including the contribution from GBR. It has been observed that, generally, with increasing cooling rate, the fraction of the low IQ peak increases, which indicates higher dislocation density and also larger grain boundary area. For the water quenched specimen, the profile of the distribution curve in the low IQ region is evidently different from the others, where there seems to be one extra peak. Further analysis of this curve will be given later using the Multi-Peak model.

Since grain size variation with the cooling rate change has been detected, filtering the GBR points will certainly increase the accuracy of the analysis. Figure 5.13 (B) shows the IQ distribution curves after GBR points have been filtered. Similar changes of the distribution profile with cooling rate have been observed even more clearly. Two peaks in the low IQ region are observed for the water quenched specimen; and there is only one peak for each of the other

three conditions. All these confirm that the grain boundary region is not the only source of the distribution profile variation in the low IQ region. The formation of some different types of ferrite and the dislocation density change are certainly accounting for it.

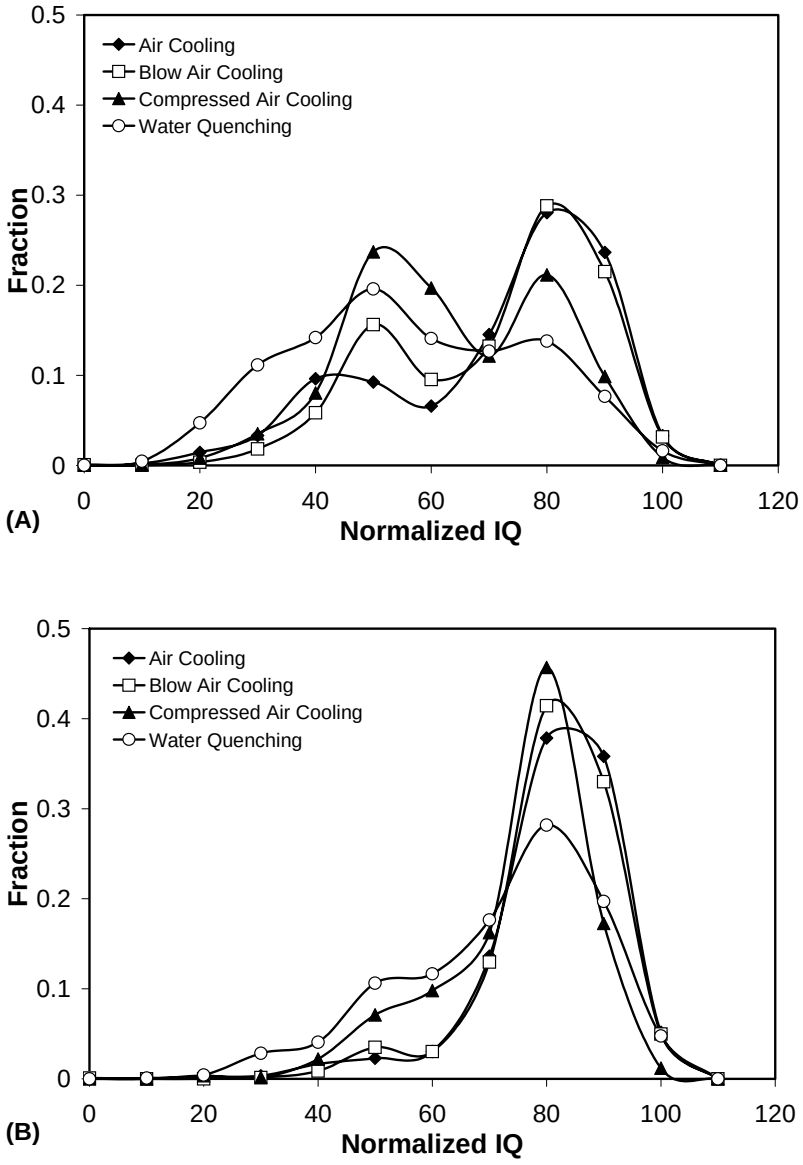

Figure 5.13 Effects of the cooling rate and the dislocation density on the image quality distribution. (A) GBR data included; (B) GBR data filtered. Microstructure A1: Air cooling; Microstructure A6: Blow air cooling; Microstructure A7: Compressed air cooling and Microstructure A8: Water quenching.

The Multi-Peak model has been applied to analyze the IQ distribution curves shown in Figure 5.13 (B) and the results are presented in Figure 5.14. The microstructures A1, A6 and A7, which were initially thought to have 100 percent polygonal ferrite, have more or less irregularly shaped grains. The amounts of this so called non-polygonal ferrite are so difficult to be determined using traditional microstructure characterizing techniques, while a certain fraction of low IQ peak is clearly observed in Figure 5.14 (A) to (C).

The low IQ peak is the result of both of increasing dislocation density and the formation of non-polygonal ferrite. It is can be concluded through the comparison of Figure 5.12, Figure 5.13 and Figure 5.14.

Based on the optical micrographs, Figure 5.12 (B) and (C), microstructures A6 and A7 are expected to have the most similar IQ distribution because of their very similar grain size and microstructure components. And, this similarity should not be affected whether or not GBR is included. However, as shown in Figure 5.14 (B) and (C), a significant increase in the low IQ peak fraction is observed from microstructure A6 to A7. Therefore, this increase is caused mainly by the dislocation density change due to the higher cooling rate.

When the GBR is included, Figure 5.13 (A), it has been found that A1 and A6 microstructures have a similar profile of the high IQ peak. Since the grain size difference has been observed in Figure 5.12 (A) and (B), it might be predicted that the difference in the low IQ peak is caused by the grain boundary (or GBR) only and there is no other significant contribution. This prediction is confirmed in Figure 5.14 (A) and (B), where almost identical IQ distribution curves have been observed after filtering the GBR points for those two conditions. This result, together with the finding in the previous paragraph, draws out the continuous effects of the cooling rate on the microstructure development. For the IF steel under study, increasing the

cooling rate from the austenite region will first decrease the ferrite grain size. At this stage, there is no significant change in either the grain morphology or the dislocation density as the ferrite changes characteristics. Further increasing cooling rate will result in the significant increase of dislocation density. This change can hardly be observed in the optical micrographs through either the grain size or grain morphology. Since the dislocation density plays an important role in determining the mechanical properties; its importance was certainly under-evaluated because of limited quantification techniques in conventional metallography.

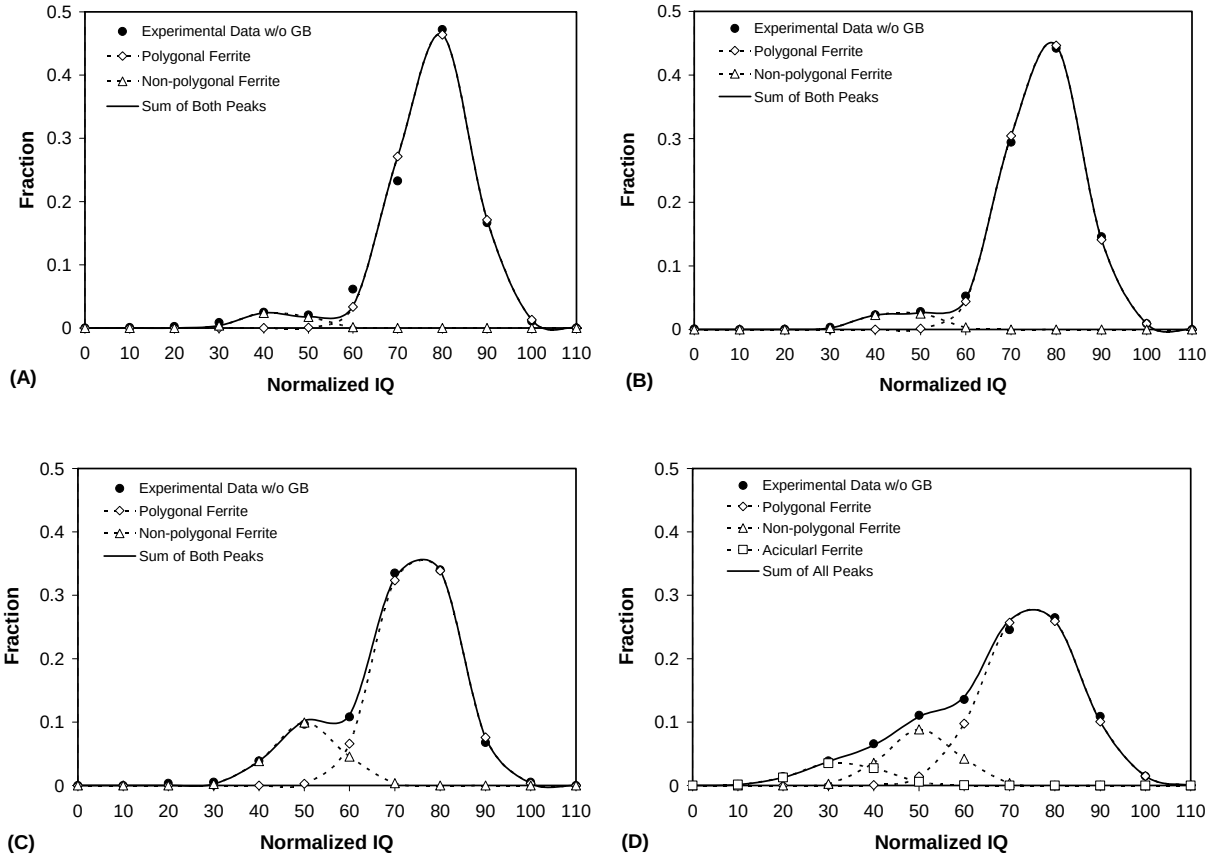

Figure 5.14 IQ distribution curves of A1, A6, A7 and A8 microstructures with GBR data filtered. (A) Microstructure A1, air cooled; (B) Microstructure A6, blowing air cooled; (C) Microstructure A7, compressed air cooled; and (D) Microstructure A8, water quenched.

Microstructure A8, water quenched, is a strange one in this group because of its multi microconstituents. The Multi-Peak model results indicate that three different types of ferrite exist in this microstructure, Figure 5.14 (D). Except for the polygonal and non-polygonal ferrites, the low IQ peak in Figure 5.14 (D) comes from the acicular ferrite, which has been detected in Figure 5.12 (D).

The Multi-Peak model analysis results shown in Figure 5.14 have been quantified and the detailed information on each peak is shown in Table 5.2. With increasing cooling rate, the fraction of the high IQ peak decreases from 95.4 percent to 74.5 percent, which indicates the second or third type of ferrite was formed and the dislocation density was increased. For the water quenched specimen, the standard deviation of the high IQ peak is also detectably higher than that of the previous three conditions. This could be caused by the significantly increased dislocation density, which introduces a larger range of variation of defect density in the polygonal ferrite grains. As for the mean IQ value, increasing cooling rate also introduced a slight decrease of it in the high IQ peak. This slight change is also explained here as the result of the increasing dislocation density in the polygonal ferrite grains.

As for the Peak II (Medium IQ) in Table 5.2, which was referred to as low IQ peak in the previous text discussing A1, A6 and A7 microstructures, the fraction is found to have the similar tendency with Peak I with changing cooling rate. So does the standard deviation. The mean IQ value of Peak II is found surprisingly to increase with increasing cooling rate. There are two explanations of this. Number one is that increasing cooling rate reduces the IQ_{Max}, which could affect the normalized IQ data through Equation 5.2. About the variation of normalization, more discussion will be given in section 6.0. The second explanation comes from the distribution of

dislocations. The dislocations reduce the IQ value. For the polygonal ferrite with high concentration of dislocations, their corresponding IQ value might shift from Peak I to Peak II. The contribution from these areas will certainly increase the mean IQ values of Peak II. From this point of view, the fraction of Peak II is actually a sum of both non-polygonal ferrite and low IQ polygonal ferrite. Before it is further divided, the IQ peaks could be considered as a new concept describing microstructures, which is based on the lattice imperfection, not the conventional grain morphology.

Table 5.2 The Multi-Peak analysis results of A1, A6, A7 and A8 microstructures with GBR data filtered.

Materials Code		Peak I (high IQ)			Peak II (Medium IQ)			Peak III (Low IQ)		
		Mean IQ	Fraction (%)	Std. dev.	Mean IQ	Fraction (%)	Std. dev.	Mean IQ	Fraction (%)	Std. dev.
A1	AC	76.0	95.4	7.5	41.0	4.6	6.2	-	-	-
A6	BAC	75.0	94.6	7.5	43.0	5.4	6.2	-	-	-
A7	CAC	72.8	81.1	7.5	48.0	18.9	7.0	-	-	-
A8	WQ	72.6	74.5	9.8	48.0	17.3	7.2	30.5	8.2	8.3

Both the cold deformation and the transformation procedure could introduce the low IQ peak that indicates area with higher dislocation densities. However, the mean IQ values of the low IQ peaks caused by different processing are different. The mean IQ value of the low IQ peak caused by cold deformation is usually lower than that of the case caused by transformation. The cold deformation also has a more significant effect on the overall average IQ value and could shift the entire IQ distribution to the left. From this point of view, IQ analysis could possibly be used to study and distinguish those dislocation density distributions.

5.2.7 Duplex microstructure analysis

As mentioned earlier, two types of duplex microstructures have been developed in this study: B0, which is a ferrite + martensite microstructure; and C0, which is a mixture of allotriomorphic ferrite and acicular ferrite.

For the B0 microstructure, the martensite volume fraction has been estimated, and the microstructure observation and the IQ analysis results are shown in Figure 5.15 to Figure 5.17.

An optical micrograph of the B0 structure in Figure 5.15 shows the mixture of polygonal ferrite and martensite. The image quality map of this microstructure is presented in Figure 5.16. As expected from the difference in dislocation density of these two phases, two distinct image quality regions are observed in Figure 5.16, with polygonal ferrite being the light area with high IQ component and martensite being the dark area with low IQ component.

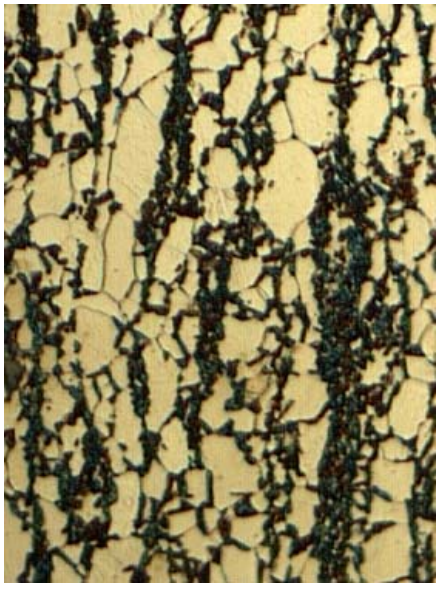

Figure 5.15 Optical micrograph of the B0 microstructure etched with 2% nital. The black area is martensite.

Further analysis of the normalized IQ data was conducted by using the multi-peak model. As shown in Figure 5.17, two normal distribution peaks have been designated and the sum of them makes a perfect match with the histogram of the experimental data. Assuming all data points in the low image quality peak come from martensite, the fraction of the low image quality peak gives the volume fraction of the martensite phase in this mixed-phase microstructure, which is found to be 43.9%. Compared to the manual measurement from optical microscopy, which is approximately 40%, the martensite volume fraction estimated using IQ analysis has a very satisfying accuracy.

Figure 5.16 IQ maps of B0 microstructure. White areas have normalized IQ values larger than 60; light gray areas have normalized IQ values between 40 and 60; and the dark gray areas have the values lower than 40.

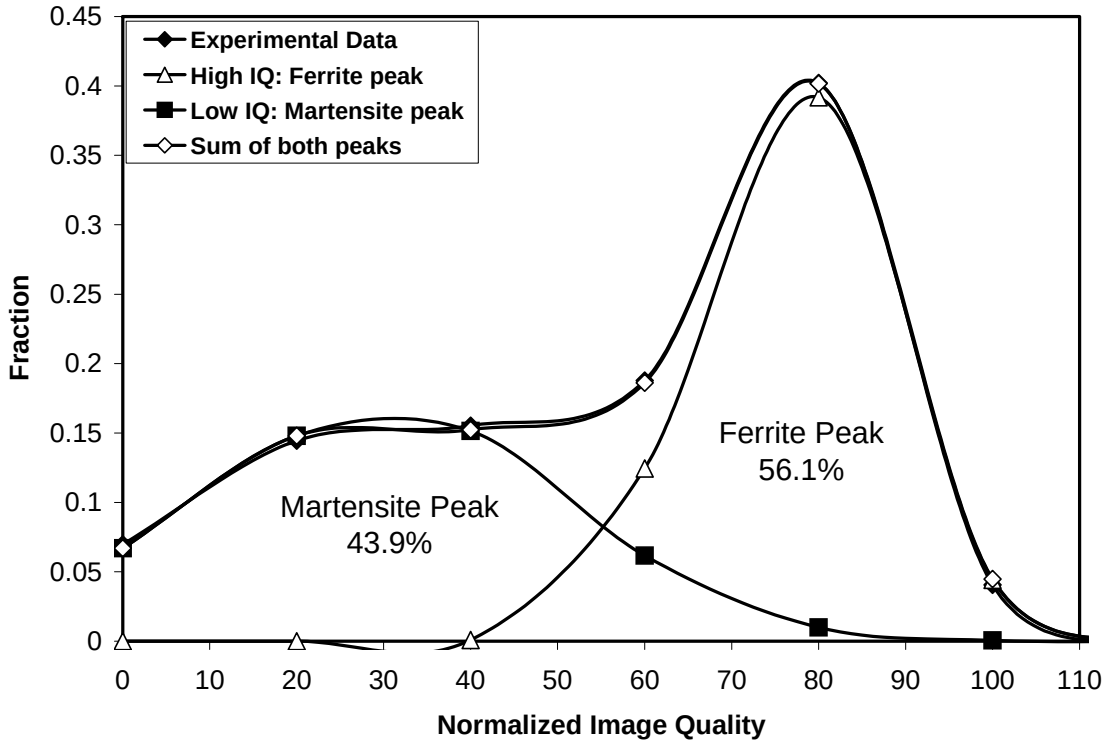

Figure 5.17 The IQ analysis of B0 microstructure as shown in Figure 5.16 using the Multi-peak model.

The major advantage of adopting the multi-peak model for IQ analysis is that it can be applied to various kinds of IQ histograms as long as they are asymmetric. IQ analysis has been used to evaluate martensite volume fractions in $\alpha + \alpha'$ microstructures only in the case of the double peaks detected [64]. In the current work, the new multi-peak model does not require any threshold to be pre-selected and the capability of this technique has been much highly developed by considering the grain boundary influence and dealing with the condition when no trough exists.

The accuracy of the IQ analysis can be affected when there are unexpected high dislocation density areas developed. For the B0 microstructure, during the martensitic transformation upon quenching, a significant amount of dislocations is produced in the ferrite grains surrounding the martensite [81, 82]. The IQ values of these areas are much reduced and they might be mistakenly considered as martensite. This explains why the measurement using this new technique is higher than the one gained from traditional optical or SEM methods. The study on how to minimize and correct this error could be a very interesting topic for future work.

For the second type of duplex microstructure, C0, a mixture of allotriomorphic ferrite and acicular ferrite, there is only one phase, ferrite with bcc lattice structure, but of different densities of lattice defects. The optical micrograph of C0 microstructure is given in Figure 5.18.

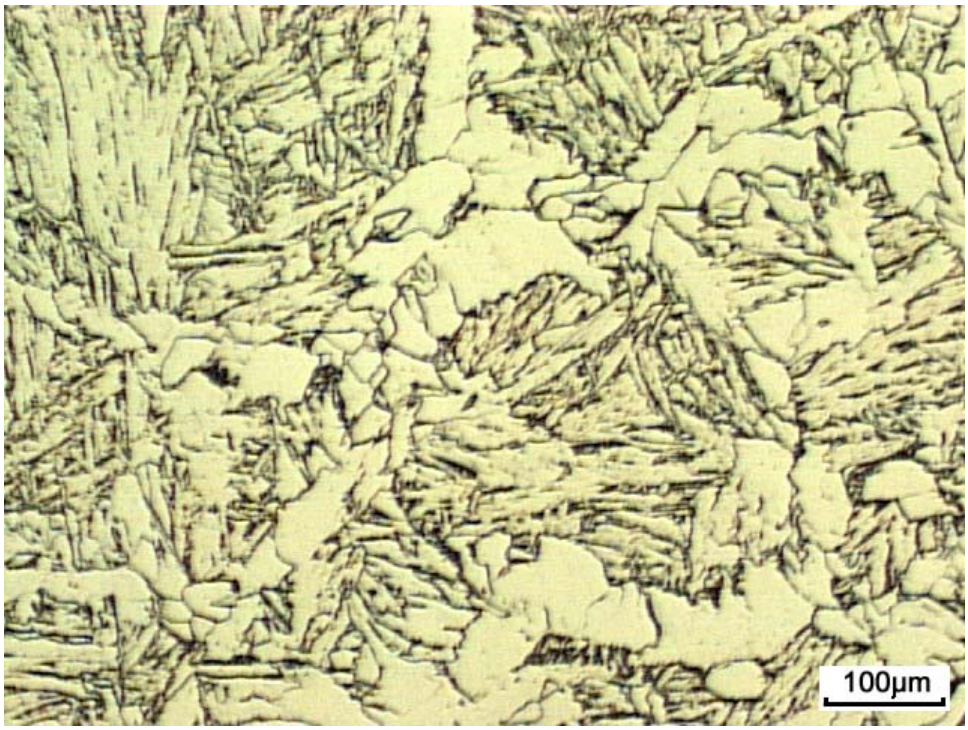

Figure 5.18 Optical micrograph of C0 microstructure developed with HSLA steel by continuously cooling from austenite temperature.

The normalized IQ data of the C0 microstructure has been analyzed using the Multi-Peak model, and the results are shown in Figure 5.19. When all EBSD data are included in the analysis, Figure 5.19 (A), three peaks have been developed for the best fit. These three peaks represent the contribution from allotriomorphic ferrite, acicular ferrite and the grain boundaries, respectively. While the GBR data are filtered, as shown in Figure 5.19 (B), only two peaks are left. Those two peaks are the two types of ferrite, which have the same IQ values as shown in Figure 5.19 (A). The important message delivered in Figure 5.19, which will be appreciated later, is that C0 is a mixture of only two types of ferrite. Other microconstituents might exist, but their amounts are negligible.

A gray scale IQ map of C0 microstructure is shown in Figure 5.20 (A). As expected, the bright area, which indicates a higher IQ value, is associated with the allotriomorphic ferrite areas; and the acicular ferrite is in the darker area with lower IQ values. A comparison of Figure 5.20 (A) and (B) shows the misorientation interfaces of C0 microstructure of the identical area, and it is clearly observed that the IQ variation is closely related to the concentration of low angle misorientations.

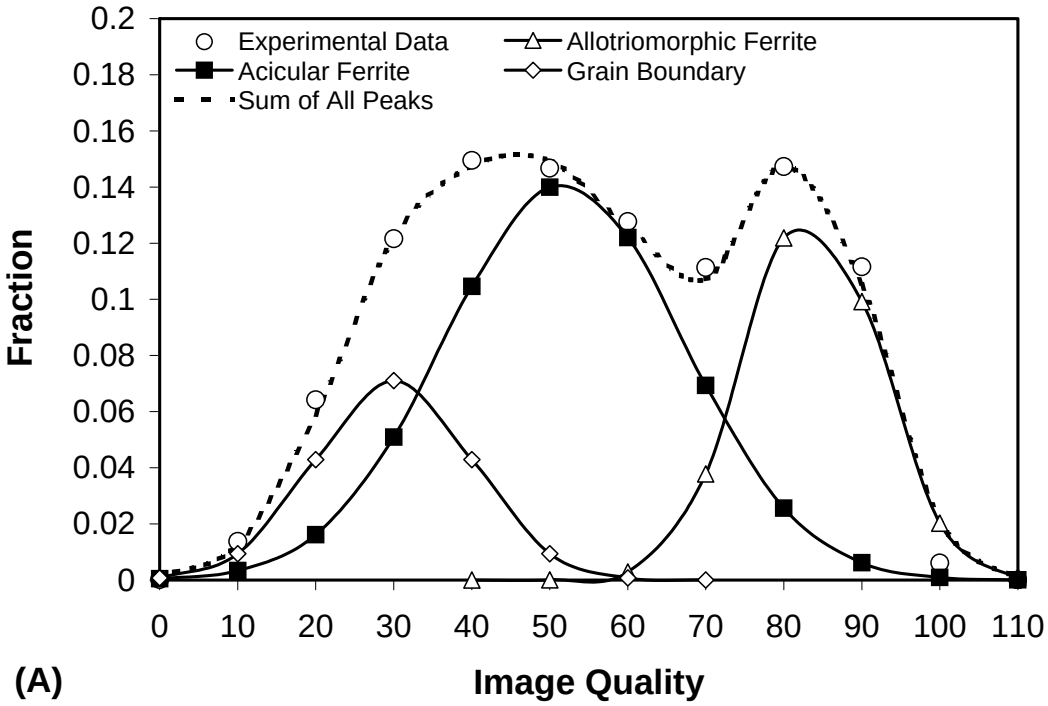

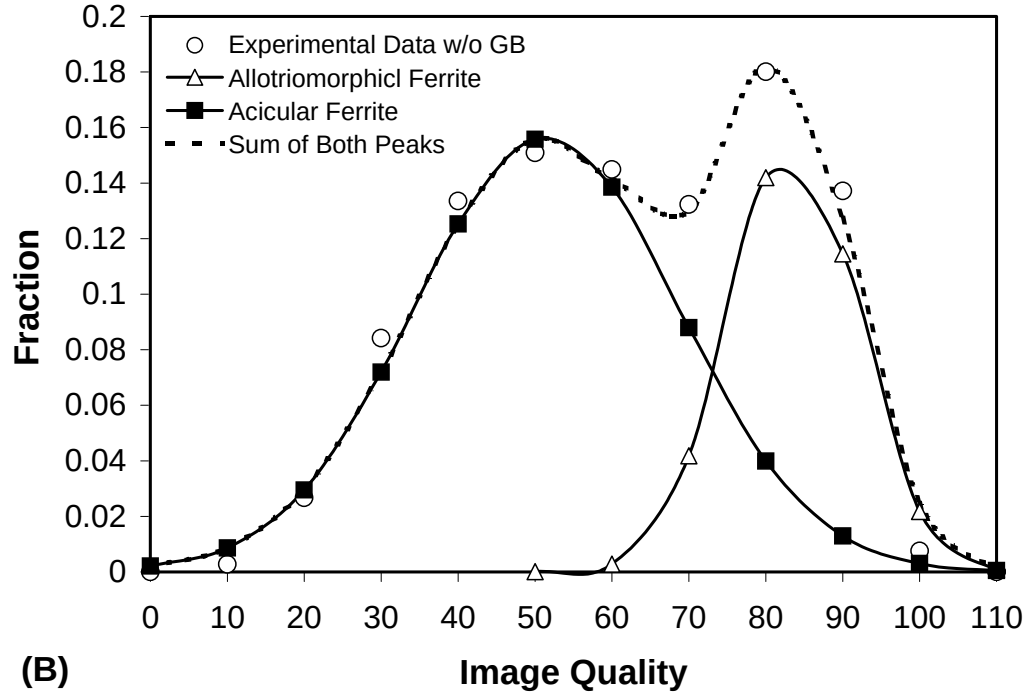

Figure 5.19 IQ distribution profile of C0 microstructure and the analysis result using Multi-Peak model.

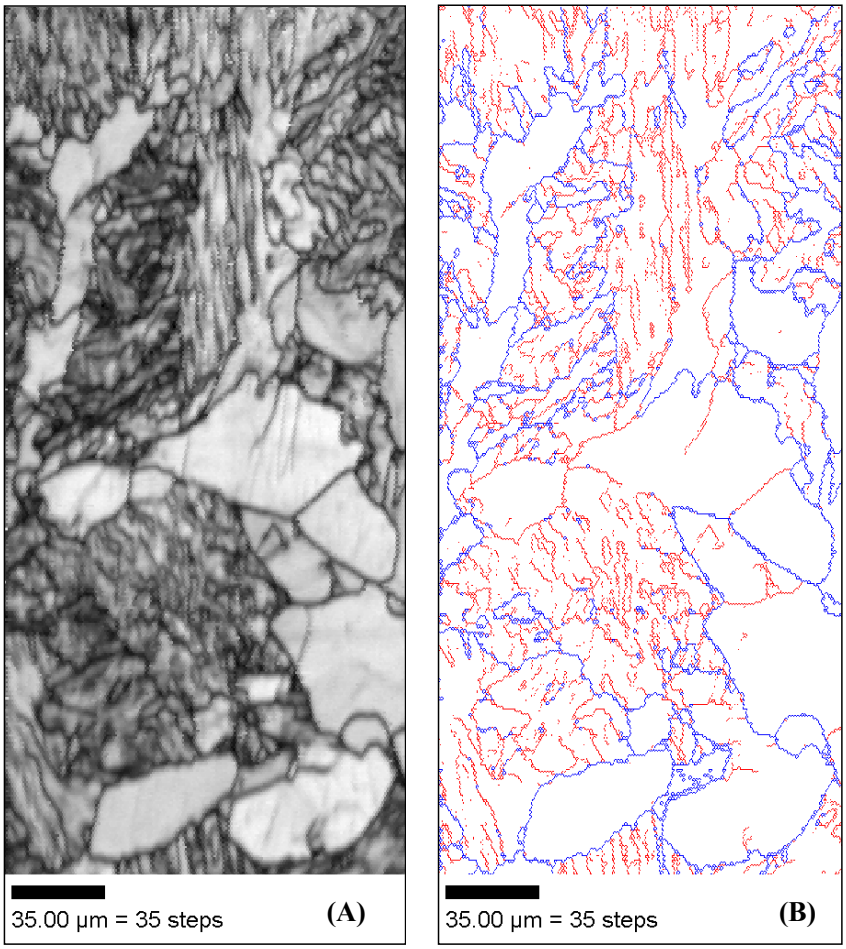

Figure 5.20 C0 microstructure. (A) Gray scale image quality map; (B) Misorientation map.

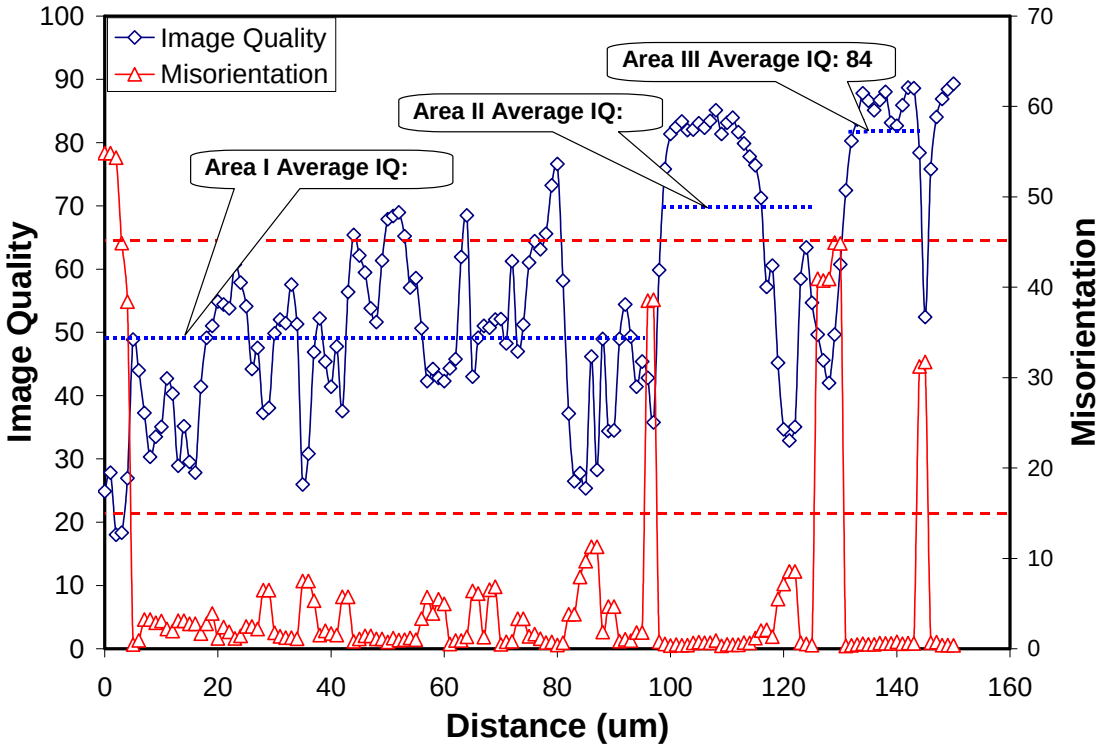

Figure 5.21 An individual line scan result of C0 microstructure

To quantify the correlation between IQ values and the low angle misorientation distribution, a special data processing program has been developed. In this so-called line scan program, along every horizontal line in the area of interest, the misorientation and the average IQ value are calculated from every two neighboring scan points. Both the misorientation and the mean IQ values are recorded as a function of the distance from the current location to the left edge of the area. One typical line scan result is shown in Figure 5.21. If the grain boundary is defined as the misorientation that is larger than 15^{o} and the subgrain boundaries are those between 5^{o} and 15^{o}, in the line scan shown in Figure 5.21, three and a half grains are covered and in those grains different amounts of subgrain boundaries exist. The concentration of subgrain boundaries can be

quantified by the ratio of the number subgrain boundaries (N) to the distance between the grain boundaries at the two ends. This ratio is defined as subgrain boundary density is this study. In Figure 5.21, the area I has the highest subgrain boundary density and also the lowest average IQ value, while area III has the highest average IQ value with no subgrain boundary detected.

Using the line scan program, both IQ values and the low angle misorientation concentration can be measured. However, critical errors could be introduced by this program and that could make the result unreliable. As illustrated in Figure 5.23, low IQ values could be mistakenly assigned to some intercepts, which actually have no subgrain boundaries, because of the GBR. In the line scan II in Figure 5.23, there are three intercepts named II-a, II-b and II-c. Each of them is expected to have high IQ and low N/L and the line scan result is reasonable. While in the line scan I, which has five intercepts, the intercept I-b and I-d might be very misleading. Both I-b and I-d have low N/L, which is ideally zero, but the IQ value might be significantly low because of the nearby grain boundaries. Those small intercepts, called edge intercepts, like I-b and I-d, are a serious source of error that might blur the correlation between IQ and N/L and make the results confusing.

To minimize this error, a threshold is selected for the purpose of filtering out the edge intercepts. There are two ways to set the threshold. The first one is based on the minimum grain size of the area under study; and the other one is based on the maximum intercept length, L_{max}. Essentially, both of them are based on the grain size; however, the intercept length might also be affected by the morphology of the grains. When the grain shape is more irregular, the second method should be more reliable. In the data processing of the C0 microstructure, intercepts that are shorter than one tenth of L_{max} are filtered.

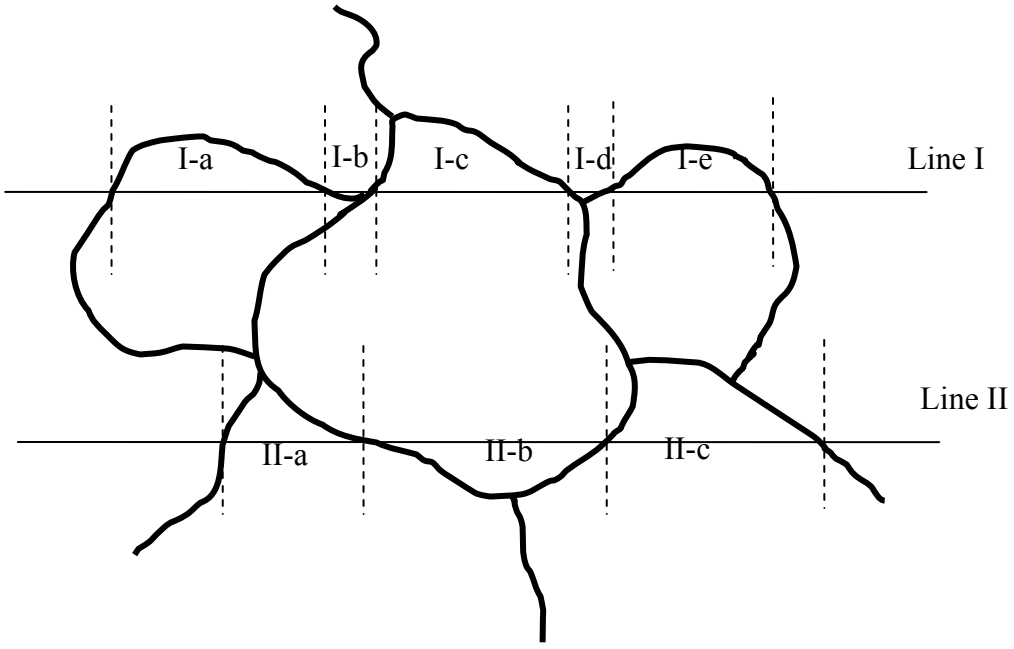

Figure 5.22 Illustration of the line scan result correction

Using repeated line scan through over the whole area, each intercept being represented with an N/L value and an IQ value, the "area" scan result of the C0 microstructure is presented in Figure 5.23. The analysis of Figure 5.23 consisted of two steps. The first step is reading the distribution of the subgrain boundary density, which is shown by the triangle line with the Y-axis in the right side of the diagram. One important message gained through step one is that there are two peaks observed in the N/L distribution. These two peaks indicate the distinguishing features about the subgrain boundary density for the two types of ferrite in C0 microstructure.

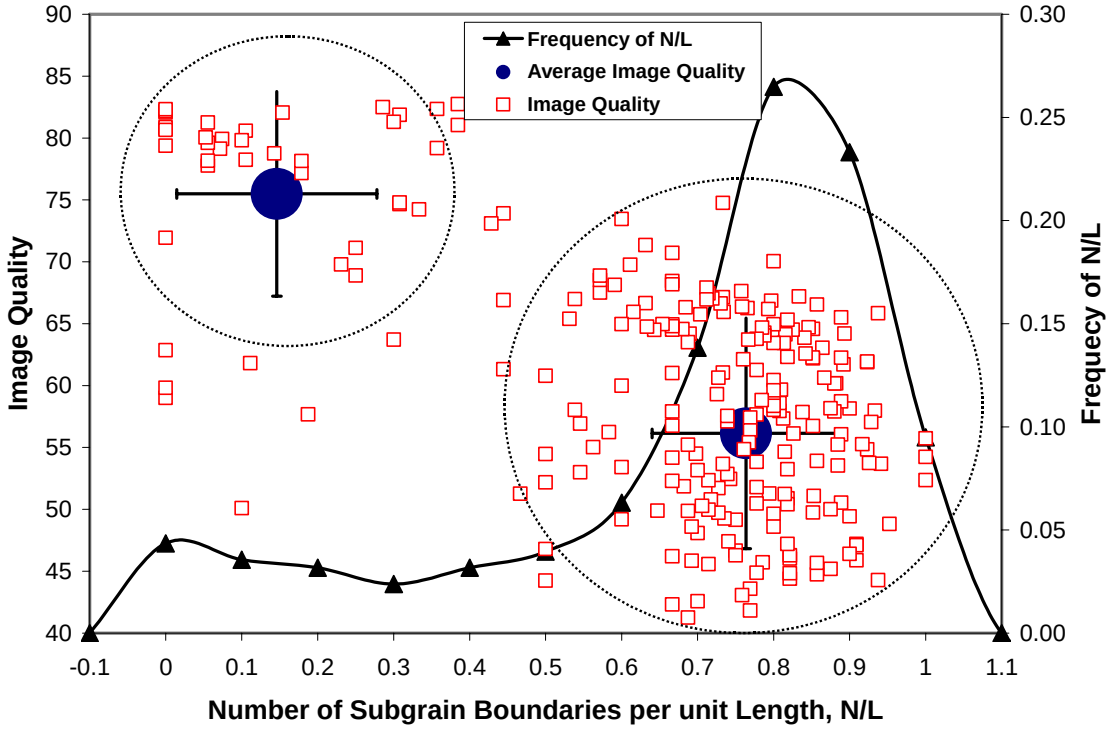

Figure 5.23 Correlation of the IQ value and the subgrain boundary density in the C0 microstructure.

Based on the N/L distribution curve, the second step is to divide all data points into two groups that represent allotriomorphic and acicular ferrite respectively. In Figure 5.23, the two dash circles roughly include the data points belonging to each group with the big black dot representing the mean IQ value of each. At the low subgrain boundary density end, the average IQ value is approximately 76; and at the high subgrain boundary density end, where there is a larger population of data points, the average IQ value is only around 56. The subgrain grain boundary density and the IQ value have been quantitatively correlated through this treatment. For the duplex microstructure, C0, several facts have been gleaned from Figure 5.23:

Two peaks in the N/L distribution indicate the main microstructural components;

IQ value decreases with increasing N/L showing the correlation between IQ and the defect density;

The low IQ group has a larger data population, which is reasonable considering the fact that the acicular ferrite has smaller grain size and shorter intercepts during line scanning.

5.2.8 Complex microstructure analysis

As the initial purpose of developing this IQ analysis technique, the hot band microstructures of the laboratory rolled HSLA steel, steel C, have been studied in this part of the work. Four hot band microstructures have been studied. They are coded as 1211, 1212, 1231 and 1232. The optical micrographs of the hot band after these processing conditions are shown in Figure 5.24. Because various cooling rates were used in the run-out-table simulation, i.e., air cooling and water spray cooling, followed by coiling, taken together with the complex CCT diagram expected for this steel, several types of ferrite were formed at different temperatures during cooling. For a complex microstructure like these, the visual identification of the ferrite types based on the morphological differences is extremely difficult, if not impossible. It is therefore nearly impossible to get an accurate measure of the volume fraction of the austenite decomposition products by using any of the traditional microstructural analyses. In Background Part of this thesis, some attempts to describe these microstructures from the conventional view of microstructure development have been made without providing many details. In this part, IQ analysis results will describe these microstructures from a totally different point of view.

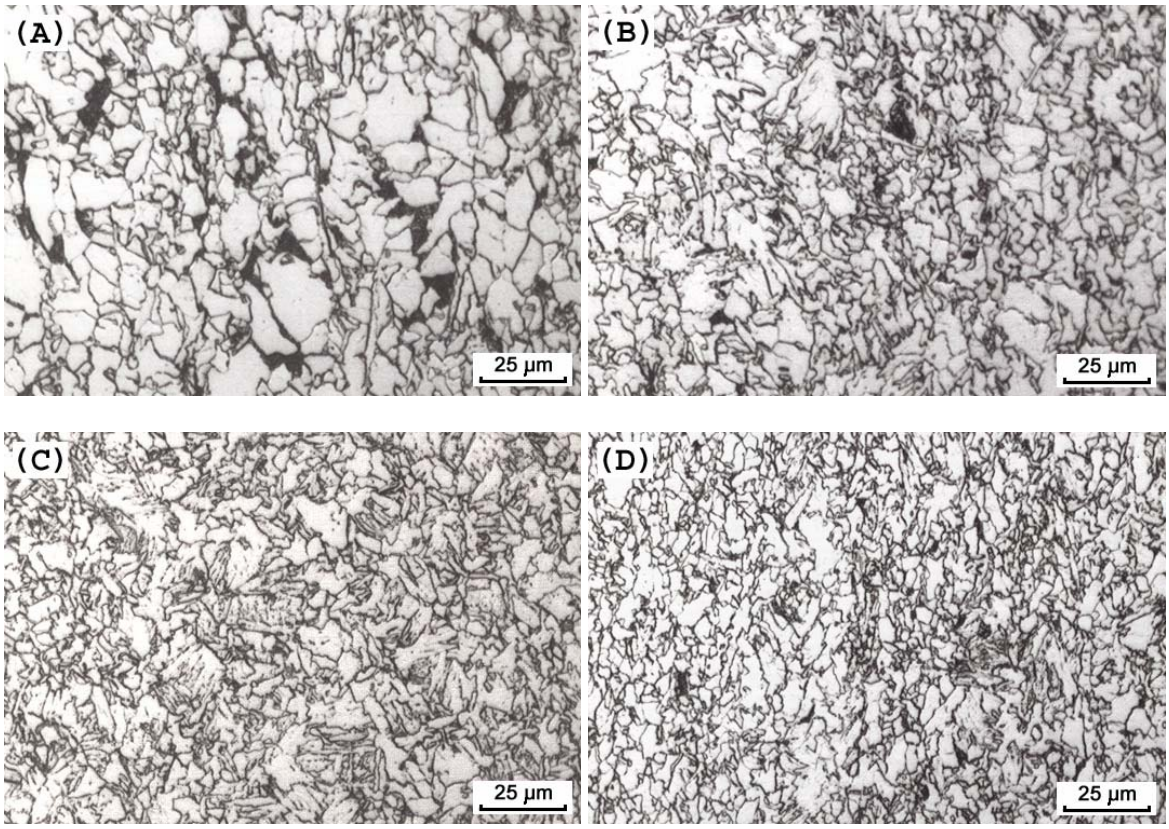

Figure 5.24 Optical micrograph of the laboratory rolled hot band microstructure. (A) 1212; (B) 1232; (C) 1211 and (D) 1231.

The 1211 condition is selected as an example showing how the IQ analysis is applied. EBSD maps of the 1211 microstructure are shown in Figure 5.25, in which (a) is the grain boundary and subgrain boundary map and (b) is the gray scale image quality map. It is observed that the grains with interior subgrain boundaries always have relatively lower IQ values compared to those without subgrains. The ferrite types formed at low temperatures, e.g., acicular and bainitic ferrites, have a higher degree of lattice distortion and a larger density of subgrain boundaries. Even for the grains without subgrain boundaries, the IQ values vary noticeably from one grain to another. This variation of IQ values implies a difference in lattice imperfection, e.g., dislocation

density, which is strongly influenced by the mechanism and temperature of formation of the ferrite type. Consequently, the differentiation of IQ values caused by the lattice imperfection serves to identify the different types of ferrite.

After normalization, the GBR points are determined and marked. The IQ distribution curves before and after the GBR filtering are compared in Figure 5.26, in which the distribution of the GBR points is also included. As shown in Figure 5.26, the GBR points could significantly affect the distribution curve profile. The IQ values of the GBR points cannot be simply represented as a single Gaussian distribution, which is the case for the simple microstructure. When there is a mixture of several different types of microconstituents, the IQ values of the GBR points are very much influenced by the IQ values of both the microconstituents contiguous to the grain boundary. Therefore, the GBR distribution curve in Figure 5.26 covers the whole range of IQ values. And, at the lower IQ range, the higher fraction of GBR points is detected. This is explained by the fact that the low IQ microconstituents usually have smaller grain size and, therefore, larger length of the grain boundaries.

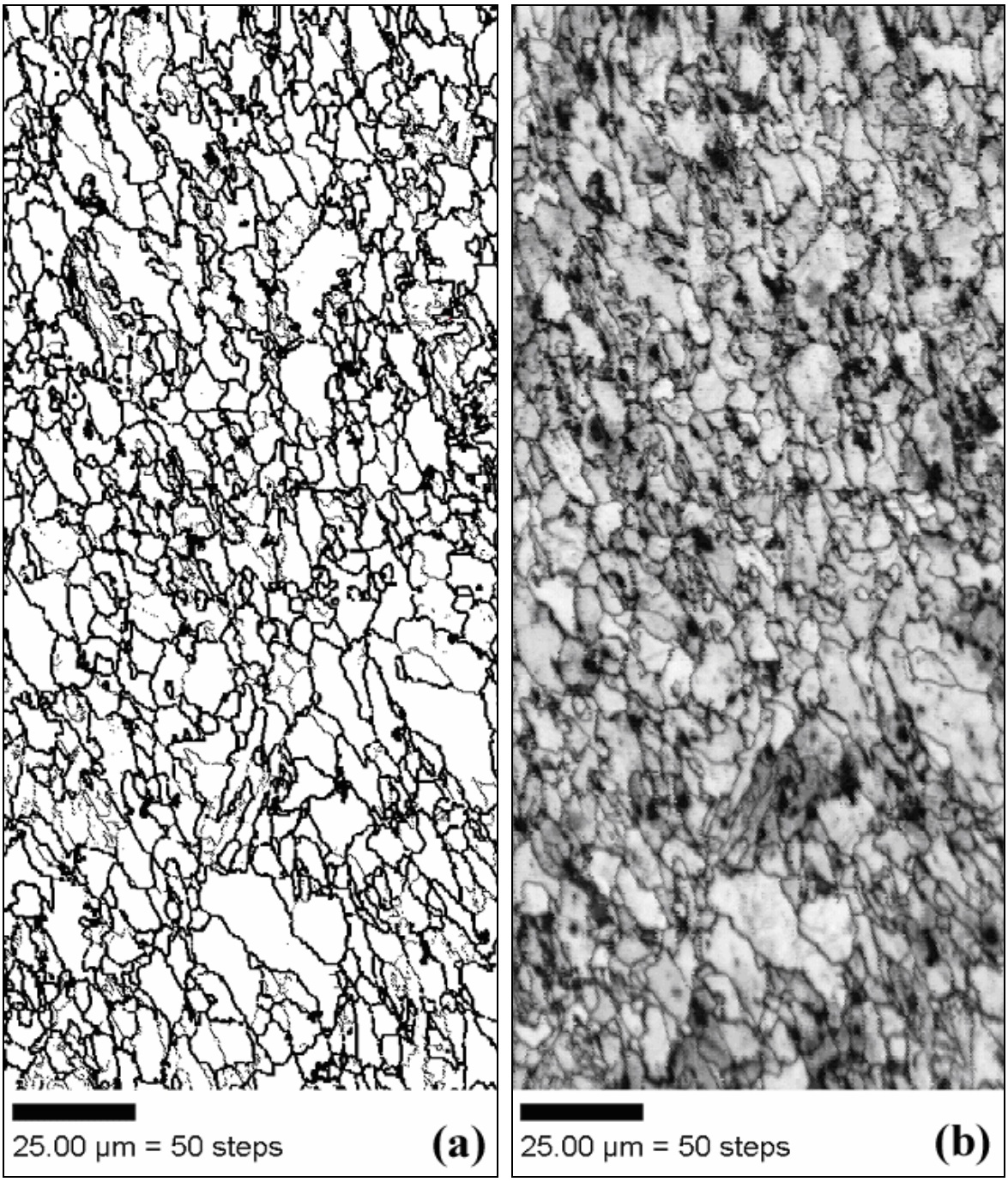

Figure 5.25 EBSD maps of the 1211 microstructure. (a) The grain boundary and misorientation map, where the thick curves are for grain boundaries with misorientations larger than 15° and the thin curves are for those from 2° to 15°. (b) The gray scale image quality map of the identical area of (a).

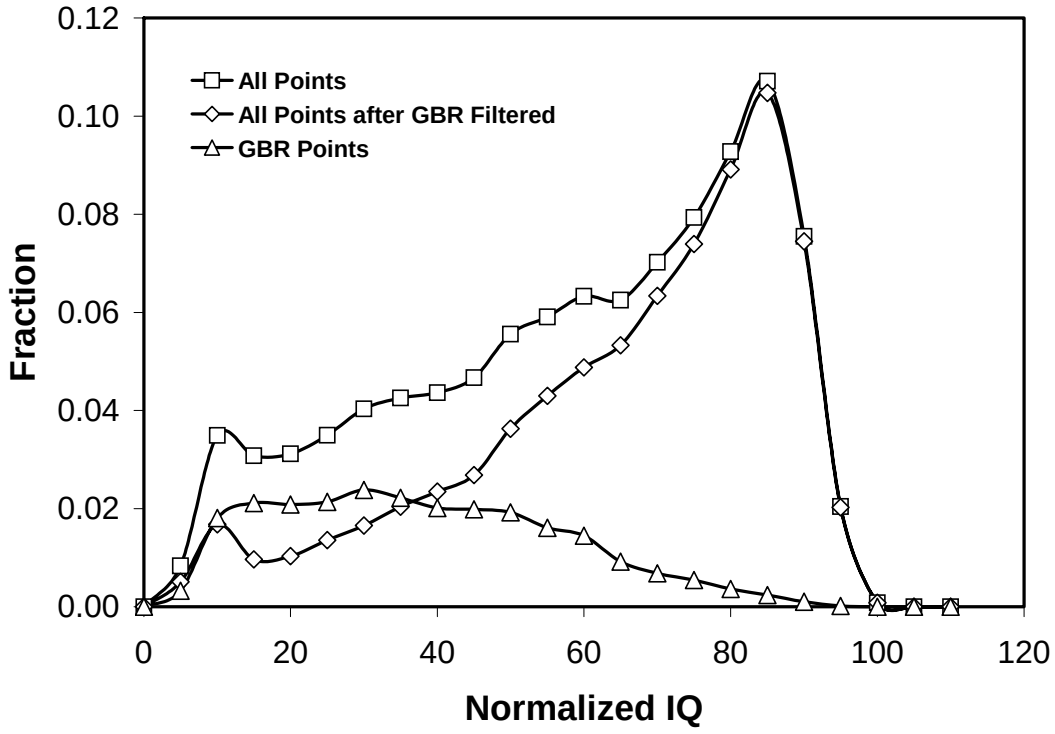

Figure 5.26 The IQ distribution curves of 1211 hot band before and after GBR filtering.

After filtering the GBR points, the IQ distribution curve shows a distinguishable low IQ peak with the mean IQ value at approximately 10. To the right of the low IQ peak, the distribution curve is still asymmetric and several different microconstituents are still expected to exist there. Therefore, the Multi-Peak model has been applied and the result is shown in Figure 5.27. A total of five normal distribution peaks are summed up and the difference from the experimental data curve is around 1.7 pct. Because the traditional classification of ferrite is mainly based on the visualized grain morphology and the IQ method relies on the lattice imperfection, the correspondence of the multi-peaks in Figure 5.27 to the particular ferrite types can only be assumed at present. The first assumption is that each component of the final microstructure has its own, individual characteristic peak in the IQ distribution curve. The

second assumption is that the mean value for each IQ peak decreases with the falling transformation temperature of each type ferrite. Thus, some correspondence of the microstructural variation and the IQ distribution curve may be possible, as indicated in Figure 5.27.

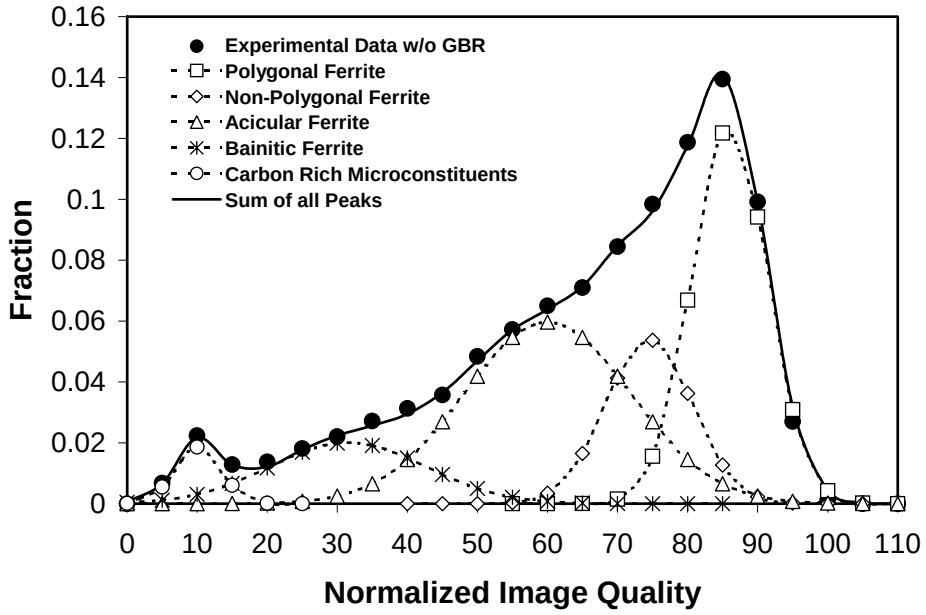

Figure 5.27 The IQ analysis result of 1211 microstructure using the Multi-Peak model.

Similarly, the Multi-Peak model has also been applied to 1212, 1231 and 1232 conditions and the results are shown in Figure 5.28 to Figure 5.30.

In Figure 5.24 (A), a significant amount of pearlite has been observed, while the fraction of the carbon rich microstituent peak in Figure 5.28 is, relatively, much smaller. As a lamellar mixture of ferrite and cementite, the pearlite is different from the other single phase microconstituents. The IQ values of the pearlite is very much affected by the thickness of ferrite

and cementite layers, the distance between layers and also the spatial resolution and the step size used. When the resolution and the step size are not fine enough to distinguish the layers of ferrite and cementite, under most cases, the pearlite would be identified as ferrite with various IQ values. Because of this, the fraction of pearlite could be under estimated. It could be improved when higher resolution SEM is used.

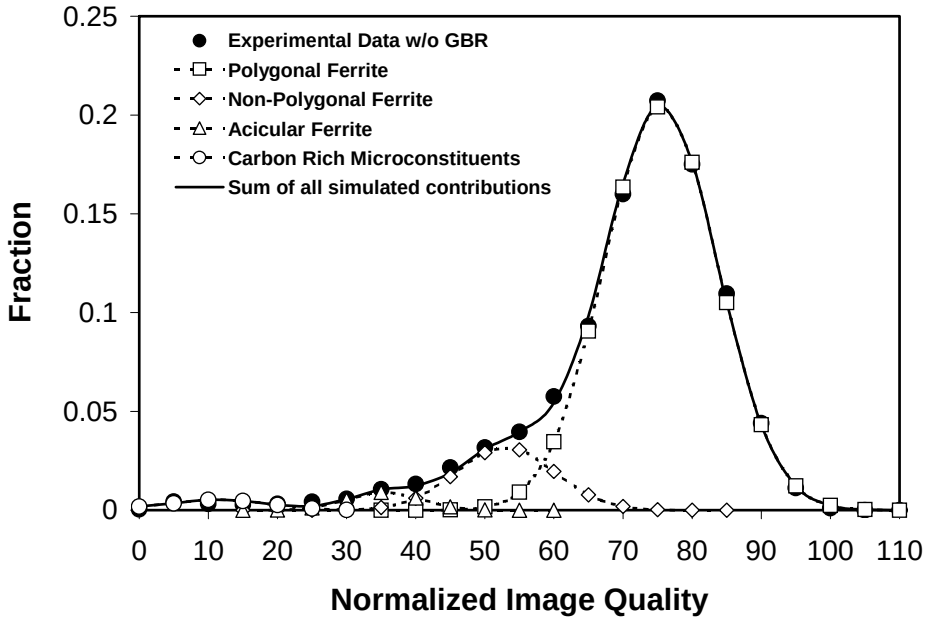

Figure 5.28 IQ analysis result of 1212 microstructure using the Multi-Peak model.

As for the 1231 microstructure, Figure 5.29, there are, totally, four individual peaks consisting of the entire distribution. Combined with Figure 5.24, these four individual peaks can be determined as the contribution from non-polygonal, acicular, bainitic ferrites and some carbon-rich microconstituents. The fraction of each can be estimated by the area under the corresponding Gaussian distribution. Again, this quantification is based on the difference in IQ

values determined by the lattice imperfection, which might be different from the conventional description based on the morphology.

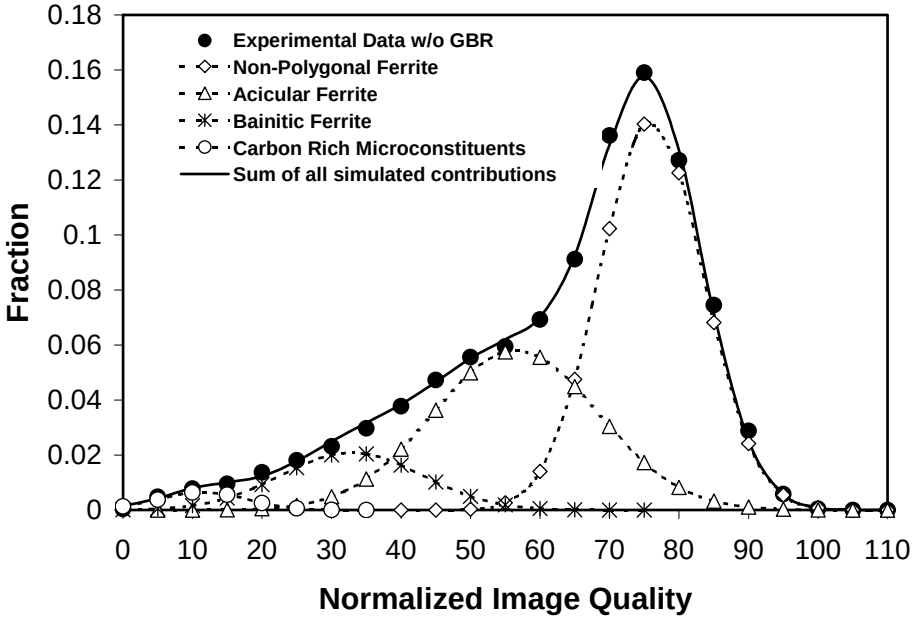

Figure 5.29 IQ analysis result of 1231 microstructure using the Multi-Peak model.

Results on the 1232 microstructure are shown in Figure 5.30, in which only three individual peaks exist corresponding to non-polygonal, acicular and bainitic ferrite, respectively. As shown in Figure 5.24 (B), a small amount of pearlite has been observed, while there is no detectable peak found in Figure 5.30 accounting for it. The absence of the pearlite peak has been discussed, previously, in relation to the 1212 microstructure. That is, the effect from cementite is relatively weak and, therefore, pearlite is mostly identified as ferrite during EBSD scanning. Since pearlite is one of the high temperature austenite decomposition products and it is formed through the diffusion controlled nucleation-growth mechanism with incoherent interface with the austenite,

very low defect density is expected in the ferrite component among the pearlite areas. Therefore, the location of the pearlite peak is very unpredictable. When IQ analysis is applied, the effect of formation temperature and undercooling would not only act on the defect density in the ferrite lamellae, but also on the spacing between the lamellae in the pearlite. Decreasing the spacing of the lamellae would enhance the influence of cementite on the IQ value and decrease the IQ values gained from the pearlite area.

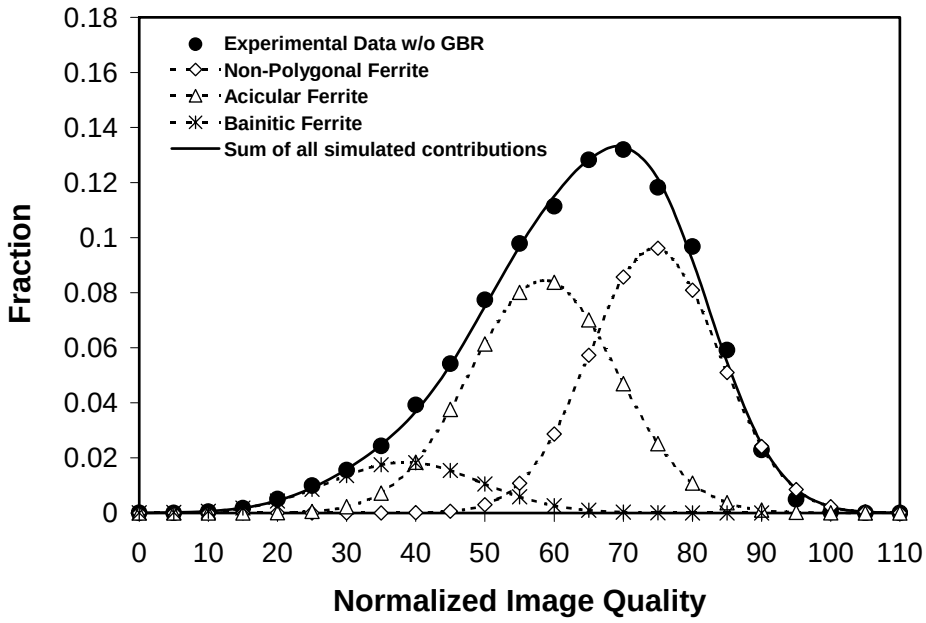

Figure 5.30 IQ analysis result of 1232 microstructure using the Multi-Peak model.

If data from Figure 5.27 to Figure 5.30 are considered, a new microstructure evolution map can be developed as shown in Figure 5.31. Compared to Figure 2.21, more information, especially the quantitative information on the microstructures, has been provided in Figure 5.31 and Figure 5.32.

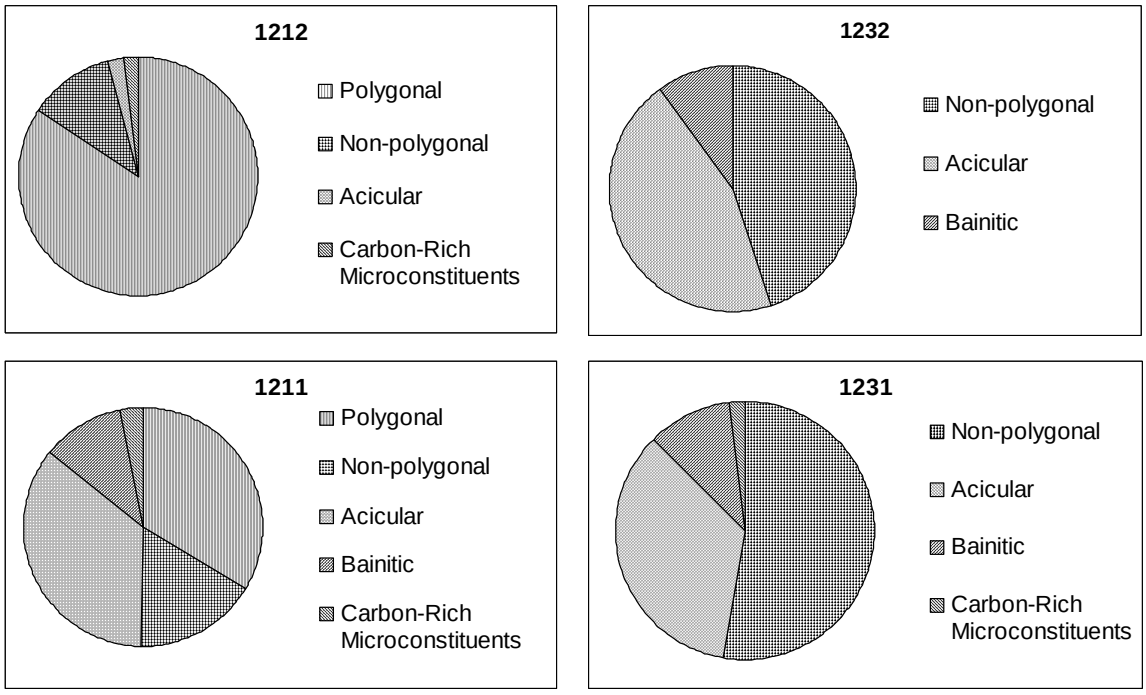

Figure 5.31 Microstructure evolution map developed based on the results from IQ analysis.

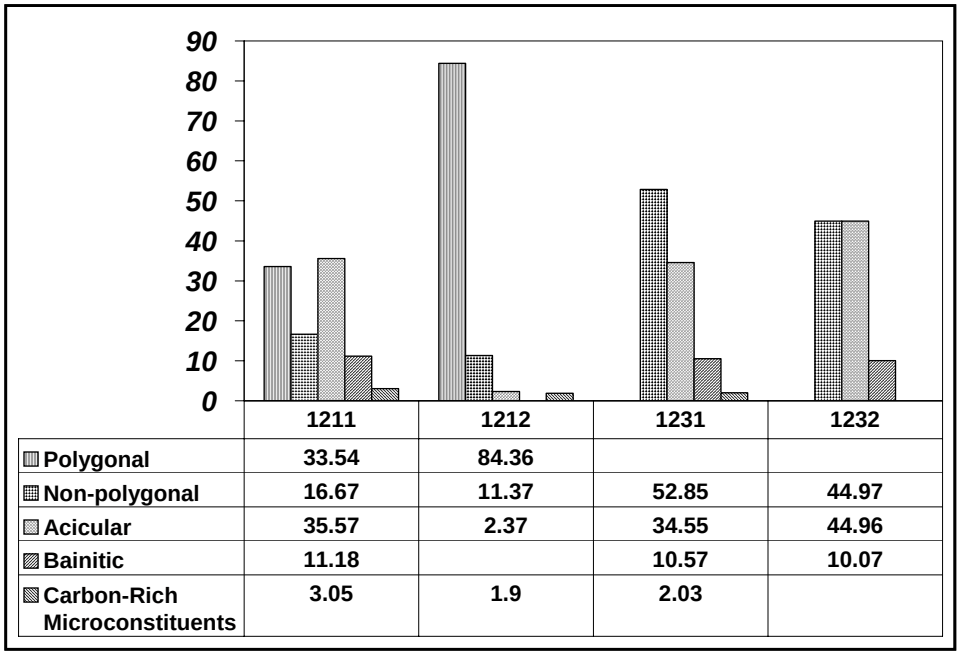

	1211	1212	1231	1232
Polygonal	33.54	84.36		
Non-polygonal	16.67	11.37	52.85	44.97
Acicular	35.57	2.37	34.55	44.96
Bainitic	11.18		10.57	10.07
Carbon-Rich Microconstituents	3.05	1.9	2.03	

Figure 5.32 Quantification of the microconstituents in the 12xx microstructures.

5.3 MICROHARDNESS AND NANOHARDNESS MEASUREMENTS

The IQ is proportional to the sharpness of the Kikuchi Pattern, which is related to the presence of crystalline defects. An elastically distorted lattice will have a smeared Kikuchi Pattern and a low IQ. A highly dislocated lattice will be expected to have a low IQ and a high nanohardness. In this part of the study, nanohardness measurements were taken on pre-selected areas of known IQ using the Nanoindentor II^{TM} equipment at the Oak Ridge National Laboratory (ORNL). In addition, microhardness measurements were conducted in the grain centers of different IQ values.

5.3.1 Microhardness and image quality

The microstructure used for the microhardness measurements is a mixture of the polygonal and non-polygonal ferrites of larger grain size (>30μm) developed by steel D. The load used in this study was 10 gram with a dwell time of 15 seconds.

As shown in Figure 5.33, large ferrite grains with different IQ values have been successfully developed. Measurement is conducted in the center of these grains to study the correlation between the image quality and the microhardness under the minimized effects from the grain boundaries. The results are shown in Figure 5.34, in which each dot represents the average value of all measurements gained from the same grain. The Vickers microhardness is found to be related to the IQ values. When the IQ value decreases from around 97 to 65, the microhardness correspondingly increased from 110 to about 190, which is a variation larger than 80%.

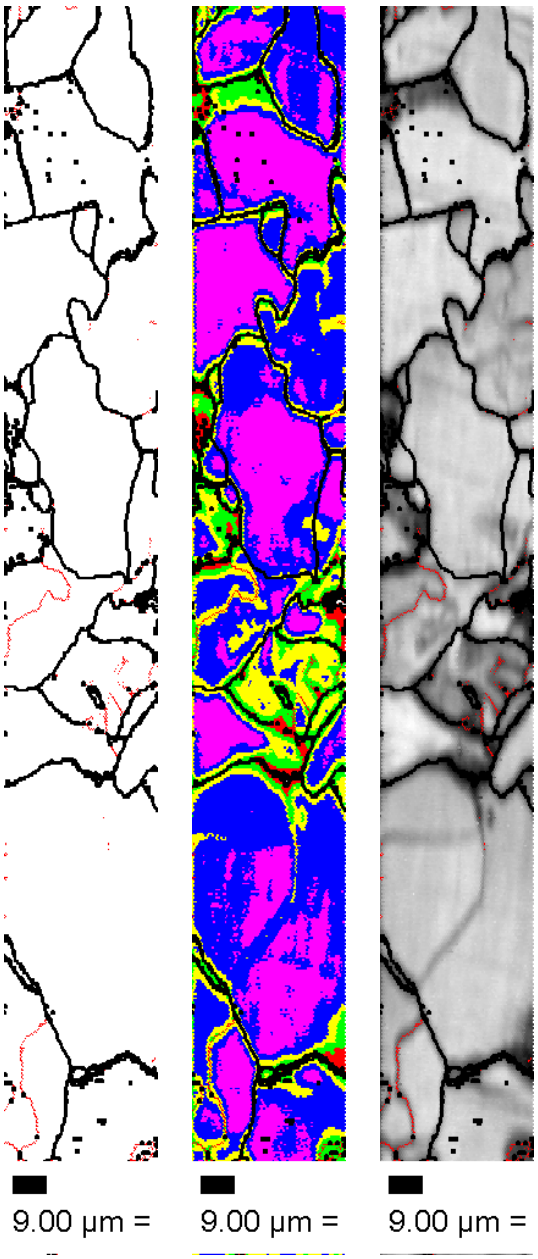

Figure 5.33 Microstructure map developed by EBSD data. Left: Grain boundary and subgrain boundary map, where the subgrain boundary is in red; Center: Range color image quality map; and Right: Gray scale image quality map.

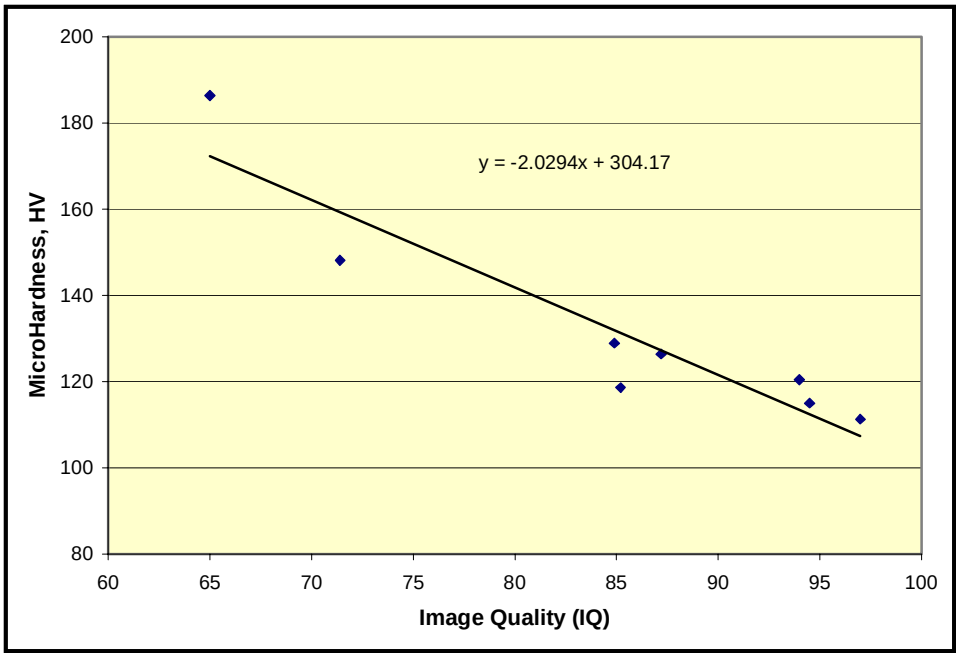

Figure 5.34 The correlation between the image quality and the microhardness.

5.3.2 Nanohardness and image quality

Compared to microhardness measurement, the benefit of nanohardness is that it provides the exact information on the local lattice properties, which are rarely affected by the grain boundaries if they are not of interest. The correlation between nanohardness and the image quality values have been developed using an IF steel specimen with different types of ferrite. The results are shown in Figure 5.35. The nanohardness values have been found to decrease with increasing IQ values, which is the same tendency as that of microhardness, but the dependence of nanohardness on IQ is relatively weak.

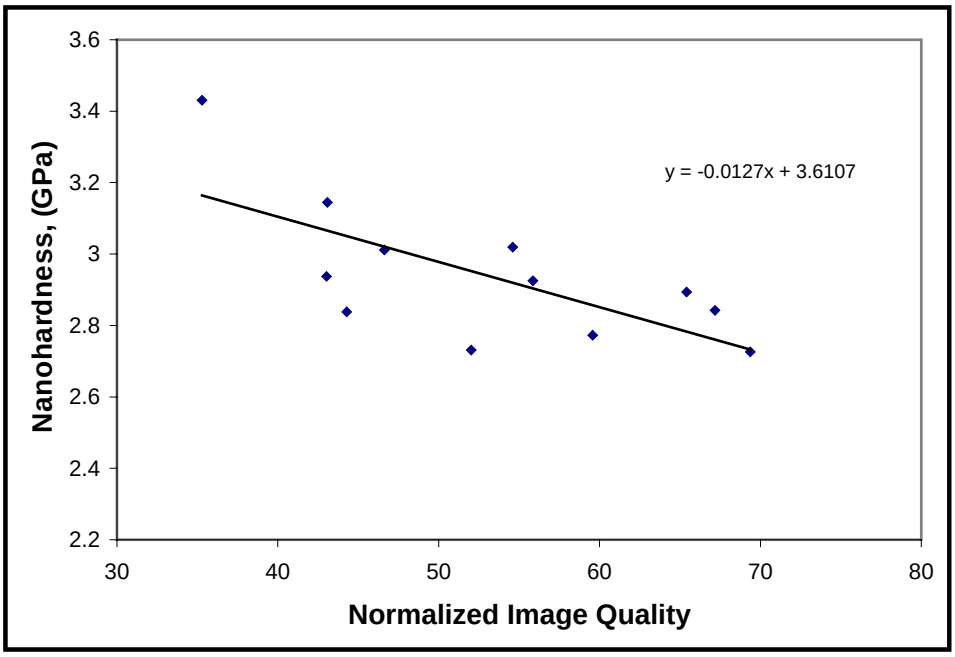

Figure 5.35 The correlation between the image quality and the nanohardness.

6.0 DISCUSSION

6.1 THE SIGNIFICANCE OF THE NEWLY DEVELOPED TECHNIQUES

Three different techniques have been studied in this work to quantitatively characterize complex microstructures. They are fractal analysis, AFM analysis and EBSD/IQ analysis. The fractal analysis could be considered as a feasible method to identify complex microstructures. But its scope is limited because it cannot provide an accurate volume fraction of each microconstituent. And fractal analysis is not an effective microstructural technique because of its requirement of a huge amount of preliminary experimental work. Therefore, it is not an ideal method for quantitatively characterizing microstructures. AFM analysis failed because the strong effect from texture on the topography condition masks the different features from the microconstituents. The EBSD/IQ analysis is the only one that can do identification and quantification successfully.

The IQ analysis gives a deeper description of the microstructures. It is called “deeper”, because it characterizes microstructures from a 3-D point of view concerning the defect densities in the lattice structure. The evolution in description of the microstructure has, also, been evaluated using the Multi-Peak model. The IQ analysis has provided more detailed information on the microstructures, especially on the volume fraction of each component. At the current stage of development, more accurate microstructure quantification can be expected by wisely combining the conventional and the IQ analysis techniques. When multiphase microstructures are studied, the conventional technique will continue to provide some valuable information on the second phase or mixed phases microconstituents formed at low temperature.

6.2 IDENTIFICATION OF GBR: ALGORITHM AND LIMITATION

Grain Boundary Region (GBR) is identified in two steps: finding the grain boundary and determining the affected area. The grain boundary is defined by the misorientation and the affected area is assumed to be the scan points contiguous to the grain boundaries. In the following sections, the algorithm and the limitation of GBR identification will be discussed.

6.2.1 Algorithm of the GBR identification

The scanning mode used in the data collection is the hexagonal mode. The scan point arrangement of the hexagonal mode is illustrated in Figure 6.1. The numbers of scan points in the odd rows and in the even rows are different; therefore, every two rows (odd and even) are combined as a group for the purpose of looping calculation. If there are n scan points in each even row, the total number of scanning points in one group equal to $2n+1$. For the whole scanning area with N scanning points, the number of loops is determined as $N/(2n+1)$ or it stops when there are no more neighboring scanning points.

During every loop, there is another small loop going through all points in the group calculating its misorientation to its neighboring points. There are basically three calculations to be conducted for each point. If all points are marked with a number from 1 to N in the regular reading order (from left to right, from top to bottom), for scanning point i, which is not at either end of the rows, the misorientations to three points marked as $i+1$, $i+n$ and $i+n+1$ are calculated. When the misorientation is larger than a pre-defined value, which is usually 15 degrees, the interface between these two points is defined as a grain boundary, and these two points, under current assumptions, are defined as GBR points. For the points at the beginning or the end of each row, because of the area boundaries, the number of calculations might be different, which is

clearly illustrated in Figure 6.2. The interface always involves two scanning points and the misorientation between points *i* and *j* is exactly the same as the misorientation between points *j* and *i*. Using the algorithm described above, no interface will be double calculated and the computational time is significantly saved.

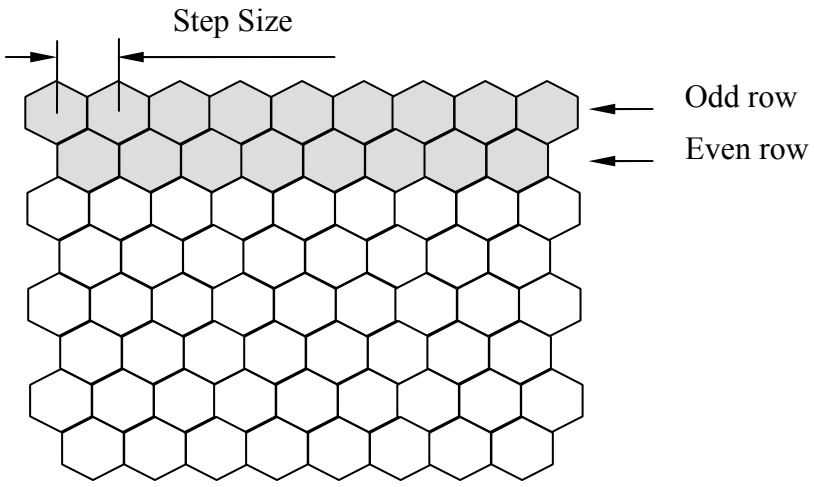

Figure 6.1 Illustration of the scan points arrangement of the hexagonal mode scanning.

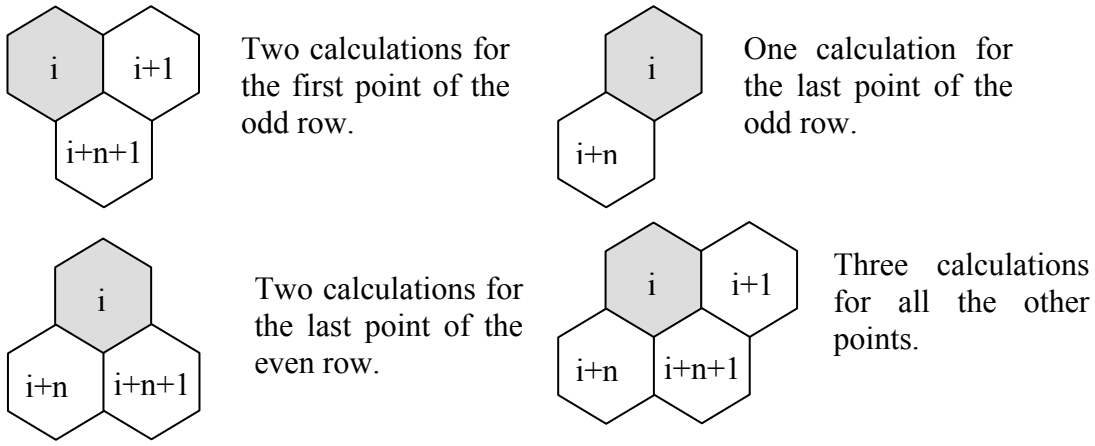

Figure 6.2 Number of calculations required to determine the misorientation between all adjacent scan points.

6.2.2 The limitation of GBR identification

The GBR identification starts with the grain boundary determination. Any errors in calculating the misorientation would certainly affect the accuracy of the GBR identification and also the IQ analysis results. The typical effects on the grain boundary determination usually come from the area with extremely high dislocation densities, such as the martensite area and the heavily cold deformed area.

In the area with extremely high dislocation densities, the heavily distorted lattice structure could significantly change the orientation from point to point. In this case, a single scan point or a group of several scan points could be considered as an individual grain with very small grain size, which is actually just a small part of a large martensite grain or a part of a deformation band in a heavily deformed area. The GBR fraction could be extremely over evaluated under these situations.

For a martensite + ferrite microstructure, the accuracy of the GBR identification can be significantly improved by introducing the phase identification into the GBR algorithm. The grain boundary is not only determined by the misorientation of the interface, but also the phase identification of the scan points on both sides of the interface. The grain boundary is defined as an interface of at least one ferrite scan point with another scan point, and with the misorientation larger than a pre-defined value (usually 15 degrees). Based on this modified definition, the martensite to martensite grain boundaries would not be identified. While in most hot band microstructures, the martensite is usually the minority phase compared to the BCC ferrite microconstituents, the area fraction of the martensite-martensite grain boundaries is low. This could be included in future work for further improvement of the accuracy.

6.3 GBR FILTER AND ITS EFFECTS ON MEASUREMENT ACCURACY

GBR is currently defined as these scan points that are contiguous to the grain boundaries. The area fraction of the GBR is strongly related to both the total length of the grain boundary, which is a feature of the microstructure under study, and the scan step size employed, which determines the covered area of each scan point and could be a source of operational errors.

As illustrated in Figure 6.1, the step size is the distance between every two neighboring scan points in the same row. Therefore, edge of the hexagonal cell, which is defined as the unit grain boundary length, can be determined by $l_{GB} = \frac{\sqrt{3}}{3} \cdot s$, where s is the step size. Considering a microstructure with the total length of grain boundaries of L, the number of grain boundary units in this microstructure, n_{GB}, can be calculated as $n_{GB} = L / l_{GB}$. For each grain boundary unit,

two contiguous hexagonal cells are identified as GBR. However, the number of GBR cells, n_{GBR}, does NOT easily equal $2 \cdot n_{GB}$. Some further consideration is illustrated in Figure 6.3.

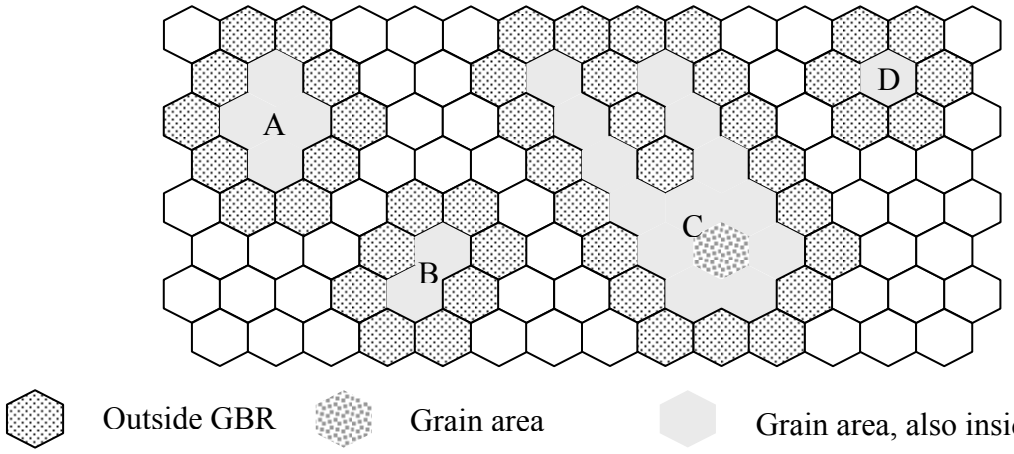

Grain A:	n_{GB} : 14	n_{GBR} : 14 (10+4)
Grain B:	n_{GB} : 10	n_{GBR} : 10 (8+2)
Grain C:	n_{GB} : 42	n_{GBR} : 35 (22+13)
Grain D:	n_{GB} : 6	n_{GBR} : 7 (6+1)

Figure 6.3 Illustration of the relation between the grain boundaries and the GBR.

In the hexagonal structure, any cell could be declared as the GBR cell by up to 6 grain boundary units, as shown in the case of grain D in Figure 6.3. For any convex shaped grain with the grain size larger than one cell, the n_{GB} always equal the n_{GBR}. This statement can be mathematically proven, but will not be discussed here. Two examples are given in Figure 6.3 as grains A and B. For those irregularly shaped grains, which have the dendrites separated by no more than one cell, grain C in Figure 6.3, the n_{GB} could even be larger than n_{GBR}. So, the

relation between n_{GB} and n_{GBR} can be summarized as: $n_{GBR} = 7 > n_{GB} = 6$ for single cell grain; $n_{GBR} = n_{GB}$ for convex shaped grains and $n_{GBR} = \alpha \cdot n_{GB}$ for all the other shaped grains, where α is a parameter between 0 to 1 and related to the curvature and the fractal features of the grain boundaries. Since the single cell grain is usually ignored during analysis, the relation can be simplified as $n_{GBR} = \alpha \cdot n_{GB}$ for all conditions.

The total GBR area can be calculated as $A_{GBR} = n_{GBR} \cdot A_{Cell} = \alpha \cdot n_{GB} \cdot A_{Cell}$, where A_{Cell} is the area of each cell, which is determined as $A_{Cell} = \frac{\sqrt{3}}{2} \cdot s^2$. For a scanning area, A, with n_G grains, the total length of grain boundaries can be estimated as $L = \sqrt{\pi \cdot A \cdot n_G}$.

Therefore,

$$n_{GB} = L / l_{GB} = \frac{\sqrt{3 \cdot \pi \cdot A \cdot n_G}}{s} \quad \textbf{6.1}$$

$$n_{GBR} = \alpha \cdot n_{GB} = \frac{\alpha \cdot \sqrt{3 \cdot \pi \cdot A \cdot n_G}}{s} \quad \textbf{6.2}$$

$$A_{GBR} = n_{GBR} \cdot A_{Cell} = \frac{3 \cdot \alpha \cdot \sqrt{\pi \cdot A \cdot n_G}}{2} \cdot s \quad \textbf{6.3}$$

The area fraction of GBR equals to

$$A_{GBR} / A = \frac{3 \cdot \alpha \cdot \sqrt{\pi \cdot n_G / A}}{2} \cdot s \quad \textbf{6.4}$$

If the average grain size is expressed as $A_G = A / n_G$, the fraction of GBR could be rewritten as:

$$A_{GBR} / A = 1.5\alpha \cdot \sqrt{\pi} \cdot \frac{s}{\sqrt{A_G}} \qquad \textbf{6.5}$$

Equation 6.5 indicates that the fraction of GBR is directly related to the scanning step size and the average grain size of the microstructure. The effects of grain morphology on the GBR fraction is realized by the factor, α, which ranges from 0 to 1.0. For polygonal ferrite microstructures, α equals 1.0. As long as the GBR covers all grain boundary affected area, decreasing step size would always improve the accuracy of the analysis. It is still not clear how to determine the range of area whose IQ values are reduced because of the nearby grain boundaries only, and none of its own lattice imperfections, for example, in the case of dual phase microstructure B0. To simplify the whole problem, grain boundaries might also be included in all analysis as a special member of the microconstituents. The only difference of this special member from the others is that its IQ distribution does not obey the normal distribution and is strongly affected by the real microconstituents associated with it.

6.4 MISLEADING FACTORS INTRODUCED BY IQ NORMALIZATION

Normalization has been used to minimize the operational effects on the IQ values, which makes it possible for IQ data gained from different EBSD processing to be compared. Two formulas have been developed to normalized raw IQ data, Equations 5.3 and 5.4. Great care should be taken in using both of these formulas to develop accurate and reasonable results.

$$IQ_{Normalized} = \frac{IQ_{Initial}}{IQ_{S\tan dard}} \times 100 \qquad 5.1$$

$$IQ_{Normalized} = \frac{IQ_{Initial} - IQ_{Min}}{IQ_{Max} - IQ_{Min}} \times 100 \qquad 5.2$$

Equation 5.4 has been widely used in this study, in which the normalized IQ value is very much affected by IQ_{Min} and IQ_{Max}. These two values would be normalized to be 0 and 100 respectively. If, for any reason, a mistakenly low IQ value is taken as IQ_{Min}, the entire normalized IQ distribution would mistakenly shift to the higher IQ value end; similarly, if the IQ_{Max} is mistakenly high, the normalized IQ distribution would shift to the low IQ end. In most cases, the population of either IQ_{Min} or IQ_{Max} is very small. Sometimes it could be just a single scan point, which is far away from the main group. In this case, the single scan point is more likely to be a bad data point and the normalization based on it would mislead the IQ analysis results.

To reduce the risk of taking bad data points as IQ_{Min} or IQ_{Max}, some pre-treatment could be done. One feasible algorithm is cutting off and averaging the ends. For a group of raw IQ data, the smallest and the largest 0.5% data points are filtered and will not be included in the further analysis. Afterwards, based on the left data group, the average IQ values of the top and the bottom 0.5% data points are defined as IQ_{Max} and IQ_{Min}, respectively. This technique will significantly reduce the possibility of taking error data points into the normalization. This pre-treatment has been applied in this study. Since there is no significant error data point included in

normalization, no obvious difference has been obtained before and after using this pre-treatment. However, in some other studies, with using this pre-treatment, much more improved and reasonable results have been achieved.

Another misleading feature of Equation 5.4 comes from its assumption, which is always neglected by the users. Equation 5.4 is applicable to those microstructures that have similar microconstituent components, but different population. This assumption implicates that the IQ analysis results are comparable only when the IQ_{Min} and IQ_{Max} values introduced by certain microconstituents in the different microstructures are almost the same. Usually the first judgment on the microconstituent components is made based on the thermal processing and/or the optical micrographs. It is suggested to compare and improve the IQ analysis results with the initial observation in order to increase the accuracy.

6.5 QUANTIFICATION OF PEARLITE AND MARTENSITE

Pearlite is not a simple phase. It is a mixture of two phases, ferrite and cementite. Therefore, the IQ value of pearlite is actually under the combined effects from ferrite, cementite and their interface. For the pearlite formed at relatively high temperature and low undercooling, the ferrite component has low defect density and the laminar space is relatively large. In this case, pearlite can be considered as two phases and can be quantified separately given a fine spatial resolution. Based on the difference in the lattice structure, the EBSD can easily identify each phase and therefore, the area fraction of each can be determined.

When the laminar space is refined or under large scanning step size, the layers of ferrite and cementite cannot be differentiated under regular spatial resolution. In this case, the IQ values of

the pearlite area will be reduced because of the combined effects from two phases. Theoretically, a single low IQ peak is expected. However, the experimental and modeling results showed that the fraction of the low IQ peak, as theoretically predicted as a pearlite peak, is much lower than the optical observation. This indicates that the IQ values of the ferrite area might not be reduced that much by its neighboring cementite. The IQ distribution of pearlite area could be a sub bi-modal distribution, and the fraction of pearlite should be the sum of the low IQ peak from cementite and some other higher IQ peak representing the ferrite. However, it is not clear yet that how the peak of the ferrite in the pearlite area can be identified and/or subtracted from all those peaks. Further study is required to resolve it.

Martensite might also introduce analysis errors. When martensite exists, two issues must be considered during IQ analysis: the GBR identification and the over-evaluation of the martensite volume fraction. The GBR identification has been discussed in the previous section. Methods have been suggested to improve the accuracy. As for the over-evaluation of the martensite volume fraction, it is caused by the ferrite grains around a martensite area, where a high dislocation density has been introduced during the martensite formation. IQ analysis based on lattice imperfection cannot distinguish those high dislocated ferrite areas from its neighboring martensite. However, this over-evaluation could be reduced if some additional treatment is applied.

Considering the microstructure shown in Figure 5.15 and Figure 5.16, the mistakenly considered martensite area is the ferrite area along the ferrite and martensite grain boundaries. The amount of these ferrite areas is determined by the total length of the ferrite/martensite interface and the region (or distance) of the area under effect. Therefore, these areas to be corrected can be determined by

$$A_{Corr} = \beta \cdot n_{GB-\alpha\alpha'} \cdot A_{Cell} \qquad \textbf{6.6}$$

where $n_{GB-\alpha\alpha'}$ is the number of the ferrite/martensite grain units and β is the parameter reflecting the distance of the high-dislocation density affected area. Parameter β might be different under various scanning step size.

When multi phases are involved, another important issue is the effect of the crystal structure on the IQ values. For certain lattice imperfection, different lattice structure might lead to different IQ distributions. However, no systematic research on this topic has been done yet. It could be a very interesting future work to be accomplished.

6.6 QUANTITATIVE CORRELATION OF THE IQ VALUE AND THE MECHANICAL PROPERTIES

IQ values have been found to be related to the microhardness and the nanohardness, which are very closely related to the UTS properties of the materials. Considering UTS as an important mechanical property, there is certainly a potential of IQ analysis to predict the general microstructure-mechanical property relations. A model to realize this potential will be proposed and discussed in this part.

Assuming the IQ value and the microhardness are related as $HV = a \cdot IQ + b$, where a and b are parameters. For a random IQ distribution described by multi-modal distribution as shown in Equation 5.6, $IQ \cong \sum_{i=1}^{k} ND(n_i, \mu_i, \sigma_i)$, each individual normal distribution $ND(n_i, \mu_i, \sigma_i)$ can be described by a function of the IQ value and the corresponding area fraction.

$ND(n_i, \mu_i, \sigma_i)$ ➔ $F_j = f(IQ_j)$

where F_i is the fraction of the areas with the IQ values at $IQ_j \pm 0.5\delta IQ$, Figure 6.4. Therefore, the mechanical property contributed by the *i*th normal distribution, MP_i, can be expressed as:

$$MP_i = \int_0^{100} \alpha_i \cdot HV_j \cdot F_j \cdot d(IQ_j) = \int_0^{100} \alpha_i \cdot HV_j \cdot ND(n_i, \mu_i, \sigma_i) \cdot d(IQ_j)$$

where, α_i is the parameter that correlates the microhardness with some macro mechanical property. The macro-mechanical property of this certain microstructure then can be predicted as:

$$MP = \sum_{i=1}^{k} MP_i = \sum_{i=1}^{k} \left[\int_0^{100} \alpha_i \cdot \left(a \cdot IQ_j + b \right) \cdot ND(n_i, \mu_i, \sigma_i) \cdot d(IQ_j) \right]$$

Similar models could also be developed for the IQ/nanohardness vs. mechanical properties. For either case, the key is to develop a reliable correlation between IQ value and the hardness measurement. This is a task requiring a huge amount of experimental measurements of both IQ and micro/nano hardness. Based on the limited amount of data gained in this study, the proposed model can hardly be verified. It is presented here for further discussion and future investigation.

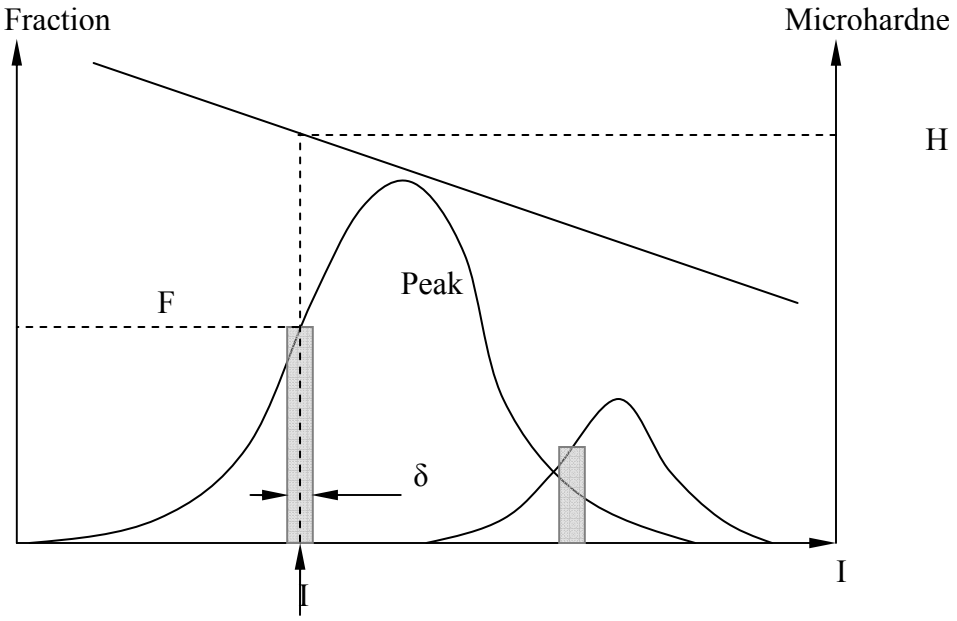

Figure 6.4 Illustration of the proposed model predicting the macro-mechanical properties using IQ distribution and microhardness measurement.

7.0 CONCLUSIONS

This thesis study started with a project on reducing the variation in mechanical properties of the hot rolled HSLA sheet steel, which led to the complex world of HSLA hot band microstructures. This complex and interesting world of microstructure limited our further understanding of microstructure-mechanical properties relations and also stimulated a new microstructure characterization technique to be developed, which is the second part of this study. As the end of this thesis study and the start of this new methodology, the main results in this study led to the following conclusions.

AFM has been tried to identify different austenite decomposition products based on the idea that the topography of the polished sample surface indicates some features of the microconstituents and could be used as identification. This attempt failed because of the fact that texture has a stronger effect on the topography than any other features.

Image quality has been introduced to identify and quantify various decomposition products based on the idea that the IQ is determined by the lattice imperfection, which is one of the most important features of different microconstituents.

IQ normalization models have been proposed in order to minimize the experimental effects on the IQ value. This model makes the IQ data gained from different EBSD processing comparable.

Based on the misorientation, grain boundaries have been identified and the Grain Boundary Region (GBR) has been defined and marked. Filtering GBR could significantly improve the

accuracy of IQ analysis, especially for the ferrite microstructure. For dual phase microstructures, special care should be taken for GBR filtering.

The IQ distribution curve of a single microconstituent has been found to be a symmetric normal distribution. The implication is that any asymmetric IQ distribution must be a sum of several individual distribution curves. This is the basis of developing the Multi-Peak model.

The Multi-Peak model has been developed, which makes it possible for different microconstituents in the same complex microstructure to be quantified.

Several different microstructures have been studied using the IQ analysis technique. Strong correlations between IQ distribution curve and the defect density have been observed.

HSLA steel hot bands have been analyzed using the IQ technique. The volume fraction of each type of ferrite has been evaluated.

A strong correlation between micro/nano hardness and the IQ value were observed. Based on this, a model predicting the macro mechanical propertiy using IQ distribution has been proposed.

Some limitations and misleading factors of this new technique have also been presented and discussed. There are still things not clear in applying this new technique. However, the IQ analysis proved to be a powerful tool with great potential in characterizing microstructures.

REFERENCES

1. Oren, E.C., *Automotive materials and technologies for the 21st century.* Ironmaking and Steelmaking, 1998. **25**: p. 67-71.

2. Baker, T.N., *Microalloyed Steels.* Science Progress, 1978. **65**: p. 493-542.

3. Graf, M.K., et al. Relationship Between Microstructure and Mechanical Properties of Thermomechanically Treated Large Diameter Pipe Steels. in HSLA Steels: Technology and Applications. 1983. Philadelphia, PA: ASM.

4. Brown, L.M. and R.K. Ham, *Dislocation-Particle Interaction*, in *Strengthening Methods in Crystals*, A. Kelly and R.B. Nicholson, Editors. 1971, Applied Science Publishers: London. p. 9-129.

5. Marder, A.R. Structure/Property Relationships in Ferrous Transformation Products. in Phase Transformation in Ferrous Alloys. 1983. Philadelphia, PA: AIME.

6. Petch, N.J., *The Cleavage Strength of Polycrystals.* Journal of the Iron and Steel Institute, 1953. **174**(May): p. 25-28.

7. Kelly, A. and R.B. Nicholson, *Precipitation Hardening.* Progress in Materials Science, 1963. **10**: p. 330.

8. Sun, F.Y., W. Xu, and X. Ma. Hall-Petch Analysis of Nb-V Microalloyed Steel Controlled-rolled in the Two Phase Gamma/Alpha Region. in International Conference on HSLA Steels'85: HSLA Steels: Metallurgy and Application. 1985. Beijing, China: ASM International.

9. Baker, T.N., *Subgrain and Dislocation Strengthening in Controlled-rolled Microalloyed Steels*, in *Hot Working and Forming Processes*, C.M. Sellars and G.J. Davies, Editors. 1980, Metals Society Book Nr264: London. p. 32-37.

10. Okamoto, H., Journal of Phase Equilibria, 1992. **13**: p. 543.

11. Smith, W.F., *Structure and Properties of Engineering Alloys*. Second ed. 1993, New York: McGraw-Hill.

12. Dubé, C.A. 1948, Carnegie Institute of Technology.

13. Aaronson, H.I., Symposium on the Mechanism of Phase Transformation in Metals. 1955, London: Institute of Metals.

14. Zhao, J.-C. and M.R. Notis, Continuous Cooling Transformation Kinetics versus Isothermal Transformation Kinetics of Steels: a Phenomenological Rationalization of Experimental Observations. Materials Science and Engineering, 1995. **R15**: p. 135-208.

15. Thewlis, G., *Classification and Quantification of Microstructures in Steels.* Materials Science and Technology, 2004. **20**: p. 143-160.

16. Aaronson, H.I. The Proeutectoid Ferrite and the Proeutectoid Cemenite Reactions. in Decomposition of Austenite by Diffusional Processes. 1962. New York: Interscience.

17. Honeycombe, R.W.K. and H.K.D.H. Bhadeshia, *Steels Microstructure and Properties*. second ed. Metallurgy and Matetrials Science Series, ed. R. Honeycombe and P. Hancock. 1995, New York, NY, USA: Halsted Press.

18. Okaguchi, S., H. Ohtani, and Y. Ohmori, *Morphology of Widmanstatten and Bainitic Ferrites.* Materials Transactions, JIM, 1991. **32**(8): p. 697-704.

19. Aaronson, H.I., The mechanisoms of Phase Transformation in Crystalline Solids. 1969.

20. Krauss, G. and S.W. Thompson, *Ferritic Microstructure in Continuously Cooled Low- and Ultralow-Carbon Steels.* ISIJ International, 1995. **35**(8): p. 937-945.

21. Massalski, T.B., *Phase Transformations*. 1970, Metals Park, OHIO: ASM.

22. Aaronson, H.I., et al., *Bainite viewed three different ways.* Metallurgical Transactions A, 1990. **21A**(June): p. 1343-1380.

23. W. T. Reynolds, J., H.I. Aaronson, and G. Spanos, *A summary of the Present Diffusionist Views of Bainite.* Materials Transactions, JIM, 1991. **32**(8): p. 737-746.

24. Zhao, J., *Continuous Cooling Transformation in Steels.* material Science and Technology, 1992. **8**(November): p. 997-1003.

25. Porter, D.A. and K.E. Easterling, *Phase Transformations in Metals and Alloys*. Second ed. 1992: Chapman & Hall.

26. Palmiere, E.J. Precipitation Phenomena in Microalloyed Steels. in Microalloying '95 Conference Processings. 1995.

27. Cahn, R.W., *Physical Metallurgy*. Second ed. 1970, London, UK: North-Holland Publishing.

28. Krielaart, G.P., J. Sietsma, and S.V.d. Zwaag, *Ferrite Formation in Fe-C Alloys During Austenite Decomposition under Non-equilibrium Interface Conditions.* Materials Science and Engineering A, 1997. **237**(2): p. 216-223.

29. Araki, T., M. Enomoto, and K. Shibata, Microstructural Aspects of Bainitic and Bainite-like Ferritic Structures of Continuously Cooled Low Carbon (<0.1%) HSLA Steels. Materials Transactions, JIM, 1991. **32**(8): p. 729-736.

30. Rees, G.I. and H.K.D.H. Bhadeshia, *Bainite Transformation Kinetics: Part 1 Modified Model.* Material Science and Technology, 1992. **8**(November): p. 985-993.

31. Hehemann, R.F., K.R. Kinsman, and H.I. Aaronson, *A Debate on the Bainite Reaction.* Metallurgical Transactions, 1972. **3**(May): p. 1077-1094.

32. Bhadeshia, H.K.D.H., ed. *Phase Transformation in Ferrous Alloys*. ed. A.R. Marder and J.I. Goldstein. 1984, TMS-AIME: Warrendale, PA.

33. Eetwisle, A.R., Metallurgical Transactions, 1971. **2**: p. 2395.

34. Christian, in *Martensite: Fundamentals and Technology*, E.R. Petty, Editor. 1970, Longmans.

35. Aaronson, H.I., et al., Tests of the Zener Theory of the Incomplete Transformation Phenomenon in Fe-C-Mo and Related Alloys. Scripta Materialia, 2001. **44**(10): p. 2425-2430.

36. W. T. Reynolds, J., et al., *The Incomplete Transformation Phenomenon in Fe-C-Mo Alloys.* Metallurgical Transactions A, 1990. **21A**(June): p. 1433-.

37. W. T. Reynolds, J., et al., *An Investigation of the Generality of Incomplete Transformation to Bainite in Fe-C-X Alloys.* Metallurgical Transactions A, 1990. **21A**(June): p. 1479-1491.

38. Bhadeshia, H.K.D.H. and D.V. Edmonds, *The Mechanism of Bainite Formation in Steels.* Acta Metalurgica, 1980. **28**: p. 1265-1273.

39. Zener, C., Journal of Applied Physics, 1949. **20**: p. 950.

40. Zener, C., Trans. AIME, 1946. **167**: p. 550.

41. Wever, F. and K. Mathieu, Mitt. Kaiser-Wilhelm-Inst. Eisenforsch., 1940. **22**: p. 9-18.

42. Bradley, J.R. and H.I. Aaronson, Metallurgical Transactions A, 1981. **12A**: p. 1729-1741.

43. Christian, J.W. and D.V. Edmonds, *Phase Transformation in Ferrous Alloys*. 1984, Warrendale, PA: TMS.

44. Bhadeshia, H.K.D.H., *Phase Transformations '87*. 1988, London: Institute of Metals.

45. Mandelbrot, B.B., *The Fractal Geometry of Nature*. 1982, New York: W.H. Freeman and Company.

46. Lu, S.-Z. and A. Hellawell, *Using Fractal Analysis to Descibe Irregular Microstuctures.* JOM, 1995(December): p. 14-17.

47. Streitenberger, P., et al., *Temperature Induced Smoothing of Initially Fractal Grain Boundaries.* Scripta Materialia, 1996. **34**(1): p. 111-119.

48. Hornbogen, E., *Fractals in microstructure of metals.* International Materials Reviews, 1989. **34**(6): p. 277-296.

49. Streitenberger, P., et al., *The Fractal Geometry of Grain Boundaries in Deformed and Recovered Zinc.* Scripta Metallurgica et Materialia, 1995. **33**(4): p. 541-546.

50. Mutschler, R.A., Effect of Solutions on Austenite Processing in Ultra-Low Carbon Steels, in Materials Science and Engineering. 2000, University of Pittsburgh: Pittsburgh, PA, USA. p. 187.

51. Kaye, B.H., A Random Walk Through Fractal Dimensions. 1989, Weinheim: VCH.

52. Russ, J.C., *Fractal Surface*. 1994, New York: Plenum Press.

53. Alam, M.N., M. Blackman, and D.W. Pashley, Proc. Roy. Soc. Lond, 1954(A): p. 221-224.

54. Humphreys, F.J., Review: Grain and Subgrain Characterisation by Electron Backscatter Diffraction. Journal of Materials Science, 2001. **36**: p. 3833~3854.

55. Humphreys, F.J., Characterisation of Fine-scale Microstructures by Electron Backscatter Diffraction (EBSD). Scripta Materialia, 2004. **to be published**.

56. Adams, B.L., Orientation Imaging Microscopy: Application to the Measurement of Grain Boundary Structure. Material Science and Engineering A, 1993. **166**: p. 59-66.

57. Bouyne, E., et al., Use of EBSD Technique to Examine Microstructure and Cracking in a Bainitic Steel. Scripta Materialia, 1998. **39**: p. 295-300.

58. Mitsche, S., et al., Quantification of the Recrystallized Fraction in a Nickel-Base-Alloy from EBSD-Data. Mscrosc. Microanal., 2003. **9**(3).

59. Black, M.P. and R.J. Higginson, An Investigation into the Use of Electron Backscattered Diffraction to Measure Recrystallied Fraction. Scripta Materialia, 1999. **41**(2): p. 125~129.

60. Gardiola, B. and C. Esling, *EBSD Study of the Austenite to Ferrite Phase Transformation in an CSP-HSLA Steel.* Advanced Engineering Materials, 2003. **5**(8): p. 583~587.

61. Okuda, K. and A.D. Rollett. Monte Carlo simulation for Recrystallization in IF Steels, Combined with OIM Microstructure. in Proceedings of IF-2003. 2003.

62. Lassen, N.C.K. Advances in Automatic Detection of KiKuchi Bands in Electron Backscattering Patterns. in CHANNEL Users Meeting. 1998. Hobro Denmark.

63. Rollett, A.D., M.L. Taheri, and B.S. El-Dasher. Texture-Dependence Measurement of Recrystallization Kinetics Using Electron Backscatter Diffraction. in Plasticity '02, the 9th

International Symposium on Plasticity and its Current Applications. 2002. Fulton MD: NEAT Press.

64. Wilson, A.W., J.D. Madison, and G. Spanos, *Determining Phase Volume Fraction in Steels by Electron Backscattered Diffraction.* Scripta Materialia, 2001. **45**: p. 1335~1340.

65. Wilson, A.W. and G. Spanos, Application of Orientation Imaging Microscopy to Study Phase Transformations in Steels. Materials Characterization, 2001. **46**: p. 407~418.

66. Tao, X. and A. Eades, *Alternatives to Image Quality (IQ) Mapping in EBSD.* Microsc. Microanal., 2002. **8**(2).

67. Binnig, G., C.F. Quate, and C. Gerber, *Atomic Force Microscope.* Phys. Rev. Lett., 1986. **56**(3): p. 930-933.

68. Baker, A., *Atomic Force Microscopy*, in *Introduction to Scanning Probe Microscopy*. 2004, University of Bristol: Bristol, UK. p. http://spm.phy.bris.ac.uk/.

69. Rempling, A., *AFM - Atomic Force Microscopy*. 2004. p. http://www.pol.chalmers.se/Pages/equipment/afm.htm.

70. Albrecht, T.R., et al., Frequency Modulation Detection Using High-Q Cantilevers for Enhanced Force Microscope Sensitivity. Journal of Applied Physics, 1991. **69**(2): p. 668-673.

71. Ros-Yanez, T., Y. Houbaert, and A. Mertens, *Characterization of TRIP-assisted Multiphase Steel Surface Topotraphy by Atomic Force Microscopy.* Materials Characterization, 2001. **47**: p. 93~104.

72. Garcia, J.E., Reducing the Variability of HSLA Sheet Steels, in Department of Materials Science and Engineering. 2002, University of Pittsburgh: Pittsburgh, PA, USA.

73. Garcia, J.E., et al. Causes of Variation in Yielding Strength in HSLA Strip Steels. in 44th Mechanical Working and Steel Processing Conference. 2002. Orlando, Florida: ISS, Warrendale, PA.

74. Palmiere, E.J., C. I. Garcia and A. J. DeArdo, *Compositinal and Microstructural Changes which Attend Reheating and Grain Coarsening in Steels Containing Niobium.* Metallurgical and Materials Transactions A, 1994. **9A**(February): p. 277-286.

75. LePara, F.S., Improved Etching Technique to Emphasize Martensite and Bainite in High-Strength Dual-Phase Steel. J. Metals, 1980. **32**(8): p. 38~39.

76. Thillou, V., Precipitation of Niobium in Ferrite, in High Strength - Low Carbon - Low Alloy Steels. 1997, BAMPRI, University of Pittsburgh: Pittsburgh, PA, USA.

77. Honeycombe, R.W.K., *Carbide Precipitation in Ferrite*, in *Phase Transformations in Ferrous Alloys*, A.R. Marder and J.I. Goldstein, Editors. 1984, TMS-AIME: Warrendale, PA. p. 259-280.

78. Honeycombe, R.W.K. Yield Points in Microalloyed Titanium Steels. in International Conference ICSMA 6 on the Strength of Metals and Alloys. 1982. Melbourne, Australia: Progamon Press.

79. Al-Hajeri, PSN Behavior of the Heavy Duty Steel. 2004.

80. Randle, V., *The Measurement of Grain Boundary Geometry*. 1993, Bristol and Philadelphia: Institute of Physics Publishing.

81. Bourell, D.L. and A. Rizk, Influence of martensite transformation strain on the ductility of dual-phase steels. Acta Metallurgica, 1983. **31**(4): p. 609-617.

82. Rizk, A. and D.L. Bourell, *Dislocation Density Contribution to Strength of Dual-Phase Steels.* Scripta Metallurgica et Materiala, 1982. **16**(12): p. 1321-1324.